


2015

## COMPUTATIONAL STUDY OF MICROSTRUCTURE- PROPERTYMECHANISM RELATIONS IN FERROIC COMPOSITES

Fengde D. Ma  
*Michigan Technological University*

Follow this and additional works at: <https://digitalcommons.mtu.edu/etds>


 Part of the [Materials Science and Engineering Commons](#), and the [Mechanics of Materials Commons](#)  
Copyright 2015 Fengde D. Ma

---

### Recommended Citation

Ma, Fengde D., "COMPUTATIONAL STUDY OF MICROSTRUCTURE-PROPERTYMECHANISM RELATIONS IN FERROIC COMPOSITES", Dissertation, Michigan Technological University, 2015.  
<https://doi.org/10.37099/mtu.dc.etds/893>

Follow this and additional works at: <https://digitalcommons.mtu.edu/etds>

 Part of the [Materials Science and Engineering Commons](#), and the [Mechanics of Materials Commons](#)

**COMPUTATIONAL STUDY OF MICROSTRUCTURE-PROPERTY-  
MECHANISM RELATIONS IN FERROIC COMPOSITES**

By

Fengde D. Ma

A DISSERTATION

Submitted in partial fulfillment of the requirements for the degree of

DOCTOR OF PHILOSOPHY

In Materials Science and Engineering

MICHIGAN TECHNOLOGICAL UNIVERSITY

2015

© 2015 Fengde D. Ma

This dissertation has been approved in partial fulfillment of the requirements for the Degree of DOCTOR OF PHILOSOPHY in Materials Science and Engineering.

Department of Materials Science and Engineering

Dissertation Advisor: *Yu U. Wang*

Committee Member: *Stephen L. Kampe*

Committee Member: *Stephen A. Hackney*

Committee Member: *Zhenlin Wang*

Department Chair: *Stephen L. Kampe*

*To my family.*

# Table of Contents

List of Figures .....	VII
Preface.....	X
Acknowledgement .....	XI
Abstract.....	XIII
Chapter 1. Introduction.....	1
1.1 Ferroic Materials .....	1
1.2 Ferroic Composites .....	6
1.2.1 Magnetoelectric Composites.....	6
1.2.2 Ferroelectric Filler - Polymer Matrix Composites.....	9
1.3 Requirement for Computational Study .....	10
1.4 Phase Field Modeling.....	13
Chapter 2. Phase Field Modeling of Ferroic Composites.....	15
2.1 Monolithic Ferroic Materials .....	15
2.1.1 Ferroelectric Materials .....	15
2.1.2 Magnetostrictive Materials .....	17
2.2 Ferroic Composites .....	18
2.2.1 Magnetoelectric Composite .....	18
2.2.2 Polymer Matrix Ferroelectric Composite .....	24
Chapter 3. Particulate Magnetoelectric Composite .....	27
3.1 Introduction .....	27
3.2 Model and Material Parameters .....	28
3.3 Simulation Procedure .....	30
3.4 Results and Discussion.....	33
3.4.1 In-Situ Poling of Ferroelectric Phase within Composite Microstructure....	33
3.4.2 Electrical Conductivity of Magnetic Phase.....	38
3.4.3 Phase Connectivity.....	39
3.4.4 Bias Magnetic Field .....	41

3.5	Conclusion.....	46
Chapter 4. Longitudinal and Transverse Responses of Particulate Magnetostrictive-Piezoelectric Composites.....		
4.1	Introduction.....	48
4.2	Model and Material Parameters.....	49
4.3	Simulation Procedure.....	50
4.4	Results and Discussion.....	52
4.4.1	Dependence of ME Coefficients on Magnetic Domain Structure.....	52
4.4.2	Magnetic Domain Engineering.....	56
4.5	Conclusion.....	57
Chapter 5. Particulate Ferroelectric Ceramic-Polymer Matrix Composites.....		
5.1	Depolarization Effect.....	59
5.1.1	Introduction.....	59
5.1.2	Material Parameters and Simulation Procedure.....	61
5.1.3	Results and Discussion.....	62
5.1.3.1	Effect of Grain Size and Particle Size.....	62
5.1.3.2	Effect of Shape of Alignment.....	65
5.1.3.3	Effect of Ferroelectric Phase Connectivity.....	66
5.1.3.4	Effect of Electrical Conductivity of Polymer Matrix.....	68
5.1.4	Conclusion.....	70
5.2	Field-Induced Ferroelectric Phase Transition and Nonlinear Dielectric Behavior.....	71
5.2.1	Introduction.....	71
5.2.2	Model and Materials Parameters.....	73
5.2.3	Laudan Theory-based Analysis of Single Crystal.....	73
5.2.4	Simulation Results and Discussion.....	76
5.2.4.1	Polycrystals and Texture Effect.....	76
5.2.4.2	Composites and Microstructure Effect.....	79
5.2.5	Conclusion.....	82

Chapter 6. Diffuse Interface Field Approach to Modeling and Simulation of Particles Packing .....	84
6.1 Introduction .....	84
6.2 Current Status and Challenge .....	85
6.3 Diffuse Interface Field Approach to Particle Packing Problem .....	87
6.3.1 Inter-Particle Contact Force .....	88
6.3.2 Friction .....	90
6.3.3 Equations of Motion .....	92
6.4 Simulation Results .....	94
6.4.1 Simulation Test of Simple Cases .....	94
6.4.1.1 Simplest Case: Free Fall of Ball in Fluid .....	95
6.4.1.2 Conveyor Problem .....	97
6.4.1.3 Problem of Sphere Rolling Downhill .....	99
6.4.2 Simulation of Particle Packing Process .....	101
6.5 Discussion and Conclusion .....	105
Chapter 7. Summary and Future Research .....	108
7.1 Insights from Computational Study .....	108
7.2 Future Research .....	110
References .....	112
Appendix A: Copyright Permission of Contents in Section 2.2.1 of Chapter 2 .....	125
Appendix B: Copyright Permission of Contents in Chapter 3 .....	127
Appendix C: Copyright Permission of Figures in Chapter 4 .....	129
Appendix D: Copyright Permission of Texts in Chapter 4 .....	131

# List of Figures

<b>Figure 1.1</b> Schematic response of polarization as a function of electric field for (a) paraelectric phase and (b) ferroelectric phase. ....	2
<b>Figure 2.1</b> (a) Grain structure and (b) phase morphology of particulate composite.....	19
<b>Figure 2.2</b> Grain structure and phase morphology of a polymer matrix composite, visualized in a simulation cell with periodic boundary condition.....	25
<b>Figure 3.1</b> Grain structure and phase morphology particulate composite, visualized in 3×3 simulation cells with periodic boundary condition.....	29
<b>Figure 3.2</b> Simulation procedure to study ME effect.....	31
<b>Figure 3.3</b> Evolution of ferroelectric domains (a-c) and magnetic domains (a'-c') during the simulation process shown in Figure 3.2. ....	32
<b>Figure 3.4</b> Simulated ME voltage coefficient ( $\alpha_{31}$ ) of 0-3 particulate composites under different conditions.....	35
<b>Figure 3.5</b> Polarization distribution in continuous ferroelectric phase of 0-3 particulate ME composite under different conditions. ....	37
<b>Figure 3.6</b> Polarization distribution in isolated ferroelectric phase of 3-0 particulate ME composite under different conditions. ....	40
<b>Figure 3.7</b> Simulated magnetic, dielectric and magnetoelectric responses of 0-3 particulate ME composite as function of externally applied magnetic field. ....	42
<b>Figure 3.8</b> Simulated magnetic domain evolution inside isolated magnetostrictive phase of 0-3 particulate ME composite in response to horizontally applied magnetic field $H$ ( $\times 10^6$ A/m) as indicated by big blue arrow.....	43
<b>Figure 3.9</b> Simulated changes of magnetization, polarization and stress in 0-3 particulate ME composite in response to increasing horizontal magnetic field from $H=1 \times 10^6$ A/m to $H=2 \times 10^6$ A/m).....	44
<b>Figure 4.1</b> Grain structure and phase morphology of 0-3 particulate composite with isotropic two-phase microstructure. ....	50
<b>Figure 4.2</b> (a) Polarization distribution in electrically poled (along $x_3$ ) ferroelectric phase of 0-3 particulate ME composite. (b) Simulation of magnetic field-induced	



polarization response in longitudinal and transverse mode, where magnetic field is applied at $t^*=180$ along $x_3$ and $x_1$ , respectively.....	51
<b>Figure 4.3</b> Simulated longitudinal and transverse ME voltage coefficients $\alpha_{E33}$ and $\alpha_{E31}$ of 0-3 particulate composites under different internal residual stress conditions.....	53
<b>Figure 4.4</b> (a) Simulated responses of magnetization and magnetic field-induced strain of 0-3 particulate composite in longitudinal and transverse sensing modes as function of applied magnetic field magnitude. Magnetic domain structure inside isolated magnetostrictive phase before application of magnetic field (b) and corresponding magnetic domain evolutions in longitudinal (c-e) and transverse (f-h) sensing modes with increasing magnetic field.....	54
<b>Figure 4.5</b> Engineered magnetic domain structures in magnetostrictive phase under different internal residual stress conditions. ....	57
<b>Figure 5.1</b> Simulated dielectric and piezoelectric properties and corresponding domain processes in monolithic ferroelectric polycrystal. ....	62
<b>Figure 5.2</b> Simulated $P$ - $E$ hysteresis loops for composites of (a) different grain size but same particle size and (b) different particle size but same grain size, where the ferroelectric phase volume fraction remains the same. ....	63
<b>Figure 5.3</b> Simulated domain microstructures in large ferroelectric particle of small grains in the composite at typical evolution stages under external electric field as highlighted on the $P$ - $E$ curve in Fig. 3(a). ....	64
<b>Figure 5.4</b> Simulated $P$ - $E$ hysteresis loops for composites of different particle shape and phase connectivity. The ferroelectric phase volume fraction remains the same. ....	65
<b>Figure 5.5</b> Comparison of simulated polarization distributions in (a) discontinuous and (b) continuous ferroelectric phase. ....	68
<b>Figure 5.6</b> $P$ - $E$ loops for 0-3 ferroelectric ceramic/polymer composites with different conductivities for polymer matrix. ....	69
<b>Figure 5.7</b> Schematic illustration of (a) linear dielectric, (b) nonlinear dielectric with early polarization saturation, and (c) nonlinear dielectric with high dielectric capacity. Shaded area indicates electric energy density stored in each dielectric material. ....	72
<b>Figure 5.8</b> Landau-Ginzburg-Devonshire free energy $f(\mathbf{P})$ as a function of polarization $\mathbf{P}=(P,0,0)$ . ....	74

<b>Figure 5.9</b> Polarization-electric field ( $P$ - $E$ ) response at different temperatures as determined from Landau-Ginzburg-Devonshire free energy $f(\mathbf{P})$ under $\mathbf{E}=(E,0,0)$ ..	75
<b>Figure 5.10</b> (a) Polarization-electric field ( $P$ - $E$ ) response at temperature 398.15 K between $T_1$ and $T_2$ along different axes of a single crystal. (b) $P$ - $E$ hysteresis associated with [100] electric field-induced transition between paraelectric and ferroelectric phases. The anhysteretic jump (dashed line) corresponds to equilibrium condition. ....	77
<b>Figure 5.11</b> (a) Polarization-electric field ( $P$ - $E$ ) response at temperature 398.15 K between $T_1$ and $T_2$ in polycrystals of different degrees of [100] uniaxial texture. (b) Energy density stored upon charging to 8 kV/cm, energy density released upon discharging, and energy density dissipated per charge-discharge cycle. ....	78
<b>Figure 5.12</b> (a) Phase morphology of 0-3 paraelectric composite; (b) Simulated $P$ - $E$ response for 0-3 paraelectric composite. ....	80
<b>Figure 5.13</b> (a) Phase morphology of a 1-3 paraelectric composite; (b) Simulated $P$ - $E$ response in the 1-3 paraelectric composite of different degrees of [100] uniaxial texture. ....	81
<b>Figure 5.14</b> Simulated polarization distributions in $0^0$ [100]-textured 1-3 continuous composites. ....	82
<b>Figure 6.1</b> Illustration for friction calculation. ....	90
<b>Figure 6.2</b> Velocity evolvment of free falling ball in viscous fluid. ....	96
<b>Figure 6.3</b> Velocity evolvment of an object dropped on a conveyor. ....	98
<b>Figure 6.4</b> Linear and angular velocity evolvment for a sphere released on an inclined plane. ....	100
<b>Figure 6.5</b> DIFA simulation of a sphere sliding/rolling downhill. ....	102
<b>Figure 6.6</b> DIFA simulation of a frictional and a frictionless packing structures. ....	103
<b>Figure 6.7</b> Formation of a typical pore in the frictional packing process. ....	104
<b>Figure 6.8</b> DIFA simulation of packing process of multi-shaped particles. ....	105
<b>Figure 6.9</b> Treatment of concave objects in the packing system. ....	107

# Preface

This dissertation is submitted for the degree of Doctor of Philosophy at Michigan Technological University. The research described herein was conducted under the supervision of Prof. Yu U. Wang in the Department of Materials Science and Engineering, Michigan Technological University, between August 2010 and January 2015.

Part of this work has been published in 2 peer-reviewed papers:

Chapter 3 and Section 2.2.1 of Chapter 2 are reprinted from the paper [Fengde D. Ma, Yongmei M. Jin, Yu U. Wang, Stephen L. Kampe, Shuxiang Dong. *Phase Field Modeling and Simulation of Particulate Magnetoelectric Composites: Effects of Connectivity, Conductivity, Poling, and Bias Field*. *Acta Materialia*, 70 (2014) 45–55].

Chapter 4 is reprinted from the paper [Fengde D. Ma, Yongmei M. Jin, Yu U. Wang, Stephen L. Kampe, Shuxiang Dong. *Effect of Magnetic Domain Structures on the Longitudinal/Transverse Magnetoelectric Response of Particulate Magnetoelectric Composite*. *Applied Physics Letters*, 104 (2014), 112903].

In these two papers, I performed the simulation data collecting, data analysis and article drafting, Dr. Jin developed the simulation model and code, Dr. Wang revised the manuscript critically and participated in data interpretation, Dr. Kampe and Dr. Dong participated in the manuscript revision and discussion.

Materials in Chapter 5 will be submitted for publication in:

Fengde D. Ma, Yu U. Wang, *Depolarization Field Effect on Dielectric and Piezoelectric Properties of Particulate Ferroelectric Ceramic-Polymer Composites: Phase Field Modeling*, and

Fengde D. Ma, Yu U. Wang, *Field-Induced Ferroelectric Phase Transition and Nonlinear Dielectric Behavior of Paraelectric Polycrystals: Phase Field Modeling*.

In these two publications, I performed the simulation data collecting, data interpretation and article drafting, Dr. Wang participated in data interpretation and revised the manuscript critically.

Fengde D. Ma  
January 2015

# Acknowledgement

First and foremost I would like to express my special appreciation and thanks to my advisor Prof. Yu U. Wang for supporting me during the past four years. He has been a tremendous mentor for me, who taught me how good research is done. The communication between Prof. Wang and me has been always clear, effective and efficient, through which he provided me with every bit of guidance, assistance, and expertise that I need for my Ph.D. thesis. The enthusiasm he has for his research was contagious for me, and will keep motivating me throughout my career.

I'd also like to give a heartfelt thanks to Prof. Yongmei M. Jin, for her great assistance in the development and debug of the phase field models for ferroic composites. I really enjoyed our collaboration and the conversations between her and me were always pleasant. She also encouraged me a lot during tough times in my Ph.D. pursuit and that really meant a lot to me.

I would like to thank my committee members, Prof. Stephen L. Kampe, Prof. Stephen A. Hackney and Prof. Zhenlin Wang for serving as my committee and for helpful discussion on my research.

I want to extend my gratitude to all faculty and staff in Materials science and Engineering department at Michigan Tech for helping me accomplish my Ph.D. study. I appreciate Prof. Paul G. Sanders and Prof. Bruce J. Pletka for their suggestions and encouragement on my work. Also I would like to thank Prof. Mark R. Plichta, Prof.

Douglas J. Swenson and Prof. Jiann-yang Hwang for their help. Thanks to Edward A Laitila, Owen P Mills, Ruth I. Kramer, Paul Fraley, Margaret Rothenberger, Beth Ruohonen and Felica Nip, for their persistent help and support in the past few years. I also would like to thank Professor Dennis Meng for his suggestions on my proposal defense.

I really enjoy my stay in Houghton in the past 4 years. Special thanks to my labmates and friends, Dr. Tianle Cheng, Jie Zhou, Liwei Geng, Dr. Hui Wang, Weilue He, Dr. Jingtuo Zhang and others for their support and encouragement. They made my life in Houghton colorful and gave me the best memories at Michigan Tech.

Finally, I would like to thank my parents (Shuzhen Ma and Dongxian Gong) and my younger sister (Xiao Ma) for their selfless, persistent support and encouragement. Special thanks to my wife, Lu Wang, for her understanding and unconditional love to me in the past several years. I feel fortunate to have such a loving family. I can never finish this long journey without their company.

# Abstract

Ferroic materials, as notable members of smart materials, have been widely used in applications that perform sensing, actuation and control. The macroscopic property change of ferroic materials may become remarkably large during ferroic phase transition, leading to the fact that the macroscopic properties can be tuned by carefully applying a suitable external field (electric, magnetic, stress). To obtain an enhancement in physical and/or mechanical properties, different kinds of ferroic composites have been fabricated. The properties of a ferroic composite are determined not only by the properties and relative amounts of the constituent phases, but also by the microstructure of individual phase such as the phase connectivity, phase size, shape and spatial arrangement.

This dissertation mainly focuses on the computational study of microstructure – property – mechanism relations in two representative ferroic composites, *i.e.*, two-phase particulate magnetoelectric (ME) composite and polymer matrix ferroelectric composite. The former is a great example of ferroic composite exhibiting a new property and functionality that neither of the constituent phases possesses individually. The latter well represents the kind of ferroic composites having property combinations that are better than the existing materials.

Phase field modeling was employed as the computing tool, and the required models for ferroic composites were developed based on existing models for monolithic materials. Extensive computational simulations were performed to investigate the microstructure-

property relations and the underlying mechanism in ferroic composites. In particulate, it is found that for ME composite 0-3 connectivity (isolated magnetostrictive phase) is necessary to exhibit ME effect, and small but finite electrical conductivity of isolated magnetic phase can beneficially enhance ME effect. It is revealed that longitudinal and transverse ME coefficients of isotropic 0-3 particulate composites can be effectively tailored by controlling magnetic domain structures without resort to anisotropic two-phase microstructures. Simulations also show that the macroscopic properties of the ferroelectric-polymer composites critically depend on the ferroelectric phase connectivity while are not sensitive to the sizes and internal grain structures of the ceramic particles. Texturing is found critical to exploit the paraelectric $\leftrightarrow$ ferroelectric phase transition and nonlinear polarization behavior in paraelectric polycrystal and its polymer matrix composite. Additionally, a Diffuse Interface Field model was developed to simulate packing and motion in liquid phase which is promising for studying the fabrication of particulate-polymer composites.

# Chapter 1. Introduction

## 1.1 Ferroic Materials

“Ferroic materials” is a general term for ferroelectric materials, ferromagnetic materials, ferroelastic materials, *etc.* The term “ferroic” was coined by Aizu, who defined a material being ferroic “when it has two or more orientation states in the absence of magnetic field, electric field, and mechanical stress, and can shift from one to another of these states by means of a magnetic field, an electric field, a mechanical stress, or a combination of these” [1]. It’s worthwhile to mention that, in spite of the name “ferroic”, it has nothing to do with the presence of iron in a ferroic material [2]. Ferroic materials have been known for a long time because of their applications in many devices. The macroscopic property change of ferroic materials may become remarkably large during the ferroic phase transition, leading to the fact that the macroscopic properties can be tuned by carefully applying a suitable external field (electric, magnetic, stress). This fact makes the ferroic materials a notable member of smart materials.

For example, ferroelectric materials, which exhibit a stable spontaneous polarization that can be switched by an external electric field, have been extensively used in ferroelectric memory, sensors, actuators, high energy density capacitors, and many other devices [3-6]. Examples of typical ferroelectrics are: barium titanate  $\text{BaTiO}_3$ , lead titanate  $\text{PbTiO}_3$  (PTO), lead zirconate titanate (PZT,) Rochelle salt, *etc* [7, 8]. The ferroelectric properties are temperature dependent. For example,  $\text{BaTiO}_3$  is in “paraelectric” phase at



high enough temperature. Application of electric field to it will induce a polarization inside the materials, and the magnitude of the induced polarization is a function of electric field, as schematically shown in Figure 1.1a. When the material is cooled down to below a certain temperature  $T_C$  called Curie temperature, ferroelectricity appears. In the ferroelectric phase the crystal is typically divided into several regions, within each the orientation of spontaneous polarization is uniform. Such regions are called domains, which are the essential feature of ferroic materials. In the absence of external electric field, the domains of different polarization orientations are arranged with equal probability thus no macroscopic polarization can be detected. Upon the application of external electric field, the polarizations are reoriented, via domain switching and domain wall motion. The macroscopic polarization depends not only on the electric field but also on the electrical loading history, resulting in a hysteresis loop, as shown in Figure 1.1b. The nonlinear response of polarization with respect to electric field may be exploited in capacitor with tunable capacitance and in ferroelectric RAM [3] for computers.

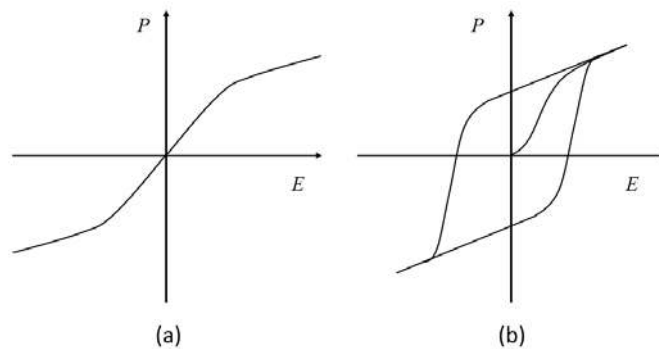


**Figure 1.1** Schematic response of polarization as a function of electric field for (a) paraelectric phase and (b) ferroelectric phase.

A lattice distortion in a ferroelectric crystal usually accompanies the polarization reorientation, which leads to the macroscopic change in the shape and dimension of the ferroelectric crystal upon the application of external electric field. This property is called piezoelectricity (a result of electrostriction effect). In the reverse effect a mechanical strain produces a measurable electrical signal. All ferroelectrics are piezoelectric, but not all piezoelectrics are ferroelectric [9]. Piezoelectricity has been used in broad applications such as power harvesting systems [10], sensors [11], actuators [12, 13], motors [14-17] and ultrasonic transducers [18, 19].

As the magnetic counterpart of ferroelectrics, ferromagnetic materials have also found extensive applications in various fields such as power conversion, signal transfer, permanent magnets, analog/digital data storage [20]. A ferromagnetic crystal could exhibit spontaneous magnetization and the concomitant domain structures. Within the domain, the magnetization is high, but a bulk material is usually unmagnetized because the domains are randomly oriented with equal probability. The domains can reorient in external magnetic field, causing the material to be magnetized. Ferromagnetics tend to stay magnetized to some extent even after the external magnetic field being removed. This property, called magnetic remanence, is the basis for many electro-mechanical devices such as electric motors, electromagnets, generators. Similar to piezoelectricity, the magnetic domain rearrangement upon an external magnetic field may also cause the ferromagnetics to change their shape or dimension. This property is called piezomagnetic effect (a result of magnetostriction). Materials exhibiting giant magnetostriction (such as Terfenol-D) [21-25] and their composites [26-36] have been attracting intensive studies.

There are very few intrinsic “multiferroic” materials in which at least two independent ferroic order parameters (ferroelectric, ferromagnetic, or ferroelastic) are coupled. A good example is a material in which ferromagnetism and ferroelectricity occur simultaneously in the same phase; the coupling between the ferromagnetic and ferroelectric order parameters produces a new effect, *i.e.*, magnetoelectric (ME) effect. The ME effect is the occurrence of induced polarization (or magnetization) by applying an external magnetic (or electric) field. Materials exhibiting ME effect have drawn extensive attentions due to their promise in applications such as magnetic field sensors, transformers, electric-write magnetic-read memory devices, and energy harvesting [[37-41](#)].

A short list of examples of ferroic materials are presented in Table 1.1 along with their properties of relevance. Note that the information provided in the table should only be used as a qualitative comparison as the data were recorded for different materials under different conditions.

**Table 1.1** Examples of ferroic materials. Adapted from [42-46]

Type	Maximum strain	Maximum pressure	Specific elastic energy density	Elastic energy density	Coupling efficiency $k^2$	Maximum efficiency	Specific density
	%	MPa	J g <sup>-1</sup>	J cm <sup>-3</sup>	%	%	
Piezoelectric (ferroelectric) ceramic (PZT)	0.2	110	0.013	0.1	52	>90	7.7
Piezoelectric (ferroelectric) single crystal (PZT-PT)	1.7	131	0.13	1	81	>90	7.7
Piezoelectric polymer (PVDF)	0.1	4.8	0.0013	0.0024	7	-	1.8
Electrostrictive polymer [P(VDF-TrFE)]	4.3	43	0.49	0.92	-	~80 (est.)	1.8
Magnetostrictive (Terfenol-D)	0.2	70	0.0027	0.025	-	60	9

## 1.2 Ferroic Composites

Composite materials, as the name indicates, are materials made up of two or more individual materials (called constituent materials) with different physical or chemical properties. Composites have been used for quite a long time in human history. For example, one of the oldest man-made composite *wattle and daub* has a history of over 6000 years and is still used as a construction materials in many parts of the world [47]. Nowadays, various modern composites have been extensively used in almost every aspect of our everyday life and industry.[48] Composites are highly designable; the combination of different constituent materials usually produce a new material with characteristics different from the constituent components. The properties of a composite are determined not only by the properties and relative amounts of the constituent phases, but also, to a great extent, by the microstructure of individual phase such as the phase connectivity, phase size, shape, spatial arrangement, *etc.* This indicates the possibility to tailor composites with property combinations that are better than the existing materials, which is the most attracting feature of composites.

In the realm of ferroic materials, different kinds of composites have been made to obtain an enhancement in physical and/or mechanical properties. The followings are two representative ferroic composites which have recently attracted lots of research activities.

### 1.2.1 Magnetoelectric Composites

As mentioned before, the magnetoelectric (ME) effect is a useful material property that has been attracting intensive study recently [41, 49-52]. However, it is a very rare

effect in single-phase materials [53]. Even in the very limited number of single-phase materials that do exhibit a ME effect, it is too weak to find practical applications [37]. Composites consisting of magnetostrictive and piezoelectric phases can offer an important means to establish a ME effect exploiting strain-mediated coupling between magnetization and polarization through magnetostriction and electrostriction effects [37]. In such composites, the ME effect is obtained when an external magnetic field induces a magnetization response in the magnetostrictive phase and simultaneously produces a strain response through a magnetostriction effect. This strain causes the magnetostrictive phase to elastically interact with the ferroelectric phase in the composite by internally applying stress to the latter. The resultant stress and strain in ferroelectric phase induces a polarization response through the piezoelectric effect and produces an electric signal (measured as charge or voltage) which results in the apparent magnetic field-induced electric response (*i.e.*, the ME effect). In this way, ME composites exhibit a property or functionality that neither of the constituent phases possesses individually, *i.e.*, it is an example of the so-called product property (in contrast to an additive or sum property) [39, 54-56]:

$$ME_H \text{ effect} = \frac{\text{Magnetic}}{\text{Mechanical}} \times \frac{\text{Mechanical}}{\text{Electric}} \quad (1.1)$$

ME composites have been fabricated in various forms, such as 0-3 particulate [57-71], 2-2 laminate ceramic composites [72-86] and thin film nanostructured composites [87-96]. The composite can be made up of various constituent material systems. Commonly used piezoelectric phases include (BaTiO<sub>3</sub>) BTO, Pb(Zr<sub>1-x</sub>Ti<sub>x</sub>)O<sub>3</sub> (PZT), PbTiO<sub>3</sub> (PTO),

$\text{Sr}_{0.5}\text{Ba}_{0.5}\text{Nb}_2\text{O}_6$  [97, 98]; and ferrites (*e.g.*, Ni ferrites, Co ferrites, Mn ferrites, Cu ferrites) [57] are often used as the magnetic phase. The 0-3 particulate ME composites have its popularity due to the easy fabrication procedure. Conventionally, sintering processing is usually employed as a simple approach to fabricate particulate ME ceramic composites [58-65]. ME coefficient as high as 10-100 mV/cm Oe have been reported by carefully controlling the sintering processing [59]. However, the experimentally obtained value of ME coefficient is still far lower than theoretical prediction. It's due partially to the high sintering temperature which causes interphase chemical reaction deteriorating the functions of active phases. In order to avoid the unwanted reactions, several new fabrication techniques, such as hot pressing [66], wet chemical processing [67-69] and spark plasma sintering [70, 71], have been employed to make 0-3 particulate ME ceramic composites.

In the early 2000s, the appearance of ME composites consisting of giant magnetostrictive alloy Terfenol-D brought the development of ME composite into a new era. Both theoretical prediction by Green's function [66, 68] and experimental observations [27, 68, 72-74, 83] showed that the Terfenol-D based ME composite (both particulate and laminate) could exhibit a giant magnetoelectric effect. The obtained composites have exhibited ME coefficients (as high as 1.3 V/cm Oe, see [79]) much higher than that found in single-phase materials, suggesting promising technological potential [39].

## 1.2.2 Ferroelectric Filler - Polymer Matrix Composites

Polymer matrix composites are made by the combination of polymers and inorganic additives having different geometries. The additives can be continuous (*e.g.*, long fiber) or discontinuous (*e.g.*, short fiber, particulates, and flakes), forming a very wide range of materials. The term “filler” used here is defined, similar to Ref. [99], as a variety of solid particulate materials with various shapes — regular, irregular, acicular, fibrous, plate-like and so on. We can conveniently classify fillers according to their primary functions including modifications of: a) mechanical properties, b) fire retardants, c) electrical and magnetic properties, d) surface properties and e) processability [99, 100]. While the fillers traditionally serve to modify polymer structural materials to help them gain better mechanical properties, sometimes polymer-matrix composites with functional fillers are themselves important alternative to the monolithic functional materials and open up possibilities for new technological applications [101-103].

In particular, ferroelectric ceramic particle-filled polymer-matrix composites have been under intensive study [6, 104-109] as an alternative to conventional single-component ferroelectric and piezoelectric materials and to the more recently developed ferroelectric polymers. [6] They offer unique properties that are not attainable with monolithic ferroelectric and piezoelectric materials. [110-112] Polymers as matrix materials offer several advantages, such as good electric insulation, high dielectric breakdown strength, low mechanical brittleness, and flexible manufacturability into complex shapes. The enhanced dielectric breakdown strength of polymer-matrix composites combined with



improved dielectric constant is desired for high-energy-density capacitor applications; [111, 112] the high electrical resistivity and increased tensile strength enable high frequency and resonant applications; [26, 110] and the low density and high elastic compliance allow good acoustic impedance matching in aquatic and biological environments. [110] Polymer-matrix composites can be fabricated economically with properties tailored through microstructure control. [26, 110-112] The properties of the composites not only depend on the properties of polymer matrix and functional ferroelectric fillers, but also sensitively depend on the filler microstructures (filler particle shape, size, arrangement, textures, *etc.*) embedded in the matrix [105, 107-109].

### **1.3 Requirement for Computational Study**

The performance of ferroic composites depends on both the properties of respective constituent phases and the architecture of the two-phase microstructures. One of the central issues in ferroic composite design and optimization is to understand the effects of microstructures on composite properties and clarify the underlying mechanisms. However, due to the microstructural complexity, some fundamental issues relevant to ferroic composites have not received adequate investigation.

In particular, theoretical analyses have been performed to estimate the ME coefficient in terms of constitutive magnetostrictive and piezoelectric properties in ME composites of simplified microstructures [54, 113-126]. For example, Green's function [54, 115] and micromechanics models [117-125] was employed to obtain the effective properties of ME composite in terms of averaged fields. They all solved a set of constitutive

equations [39] for describing coupling mechanical-electric-magnetic response in ME composites, and were able to consider the details such as volume fraction, phase connectivity, particle aspect ratio, *etc.*. Equivalent circuit [127] was also developed as an analytical approach to analyze the magnetoelectric response in 2-2 laminate ME composites. But the theoretical approaches are limited when it comes to the realistic and complex composite microstructures. The complexities ultimately lie in the ferroic nature of the constituent phases in that the properties of both the magnetostrictive and ferroelectric phases are determined by their domain-level processes [128, 129]. Domain behaviors are sensitive to the nature of the inter-phase interfaces and grain boundaries present within the ME composites. Furthermore, the ferroelectric phase will not exhibit piezoelectricity without pre-treatment; the ferroelectric phase must be electrically poled in-situ within composite microstructures. Poling serves to reorient the polarizations of electric domains in the grains towards one preferential direction (poling direction), thus rendering a macroscopic polar axis and piezoelectricity to the ferroelectric phase [130]; this is necessary for the composites to exhibit the ME effect. Similarly, the magnetic phase will exhibit either a piezomagnetic or magnetostrictive response depending on whether or not a bias magnetic field is applied. Because of the serious challenges associated with a meaningful experimental and/or theoretical approaches to a detailed study of such fundamental issues at mesoscale domain levels, a computer modeling and simulation thus offers a useful, appropriate, and ultimately, complementary approach.

Computational methods are also required to take into account the realistic polymer matrix ferroelectric composite microstructures. Although several analytical approaches

have been derived for simple case of dielectric/ferroelectric inclusion in a matrix — for example, models based on Maxwell-Garnett theory [131] and Polder-Van Santen formalism [132, 133] have been used to estimate the effective permittivity for the case of spherical or ellipsoids filler — but the required knowledge of highly non-uniform distribution of polarization and local electric field inside heterogeneous composite systems can hardly be obtained by analytical approaches.

Several computational approaches, such as finite element method [134-142], boundary integral technique [143-145] and phase field method, have been employed to study different ferroic composites in a more comprehensive and accurate way. For example, finite element method have been used to investigate the layer thickness [136] and interfacial bonding [136] dependence of ME response based on the strain/stress transfer analysis in 2-2 laminate composite [135, 136]. Prediction of characteristic properties such as effective permittivity [139-141] was also studied using FEM modelling for polymer matrix ferroelectric composites. Boundary integral technique [143-145] was also proved to be useful in the calculation of the polarization, electric field distribution and interfacial boundary charge. However, both of the computing tools employ microstructure-specific space discretization, *i.e.*, discrete meshes coinciding with interphases of multiphase microstructures in composites. One of the drawbacks of these approaches is that the need for meshing becomes tedious as the complexity of the microstructures increases. For these reasons, there is still lack of studies considering the real particulate microstructures and their effects on composites properties.

## 1.4 Phase Field Modeling

The phase field method, without having to track the evolution of individual interfaces, has proved to be extremely powerful for visualizing the development of microstructure such as solid phase transformation, solidification, and grain growth [146, 147]. Modeling the complex microstructure is the strength of phase field method, because the complexity of the interfaces won't increase the requirement for computing resource, thanks to the diffuse-interface technique.

In particular, the phase field models of ferroelectric [129] and magnetostrictive material [148] have been developed in previous research, which employed fast Fourier transform technique and parallel computing algorithm to solve electric/magnetic equations in terms of polarization and magnetization vector field in reciprocal space. The models calculate heterogeneous distributions of polarization/magnetization, charge density, local electric, magnetic and/or strain field of the composites with periodic boundary conditions. These models not only can study monolithic ferroic materials, but also, are proved to be able to seamlessly incorporate in the composites of arbitrarily complex microstructures [149].

This thesis will fully develop the required phase field model for different kinds of ferroic composites by incorporating the models for monolithic materials mentioned above. The details of composite models will be presented in Chapter 2. Computational study will focus on the microstructure-property relationship and the underlying mechanism in two representative ferroic composites, *i.e.*, magnetoelectric particulate composites and

polymer-matrix ferroelectric composites, the results of which will be shown in Chapters 3-4 and Chapter 5, respectively. In Chapter 6, additional study was conducted in which a diffuse interface computational model is proposed to simulate the particle packing and motion in liquid phase (uncured polymer melt). The model is expected to find its application in the study of fabrication of particulate polymer composites.

# Chapter 2. Phase Field Modeling of Ferroic Composites\*

In this thesis, phase field modeling and computer simulation will be employed to study the relationships between microstructures and macroscopic properties of two representative ferroic composites, *i.e.*, two-phase particulate magnetostrictive-ferroelectric composite and polymer matrix ferroelectric composite. The models will be fully developed based on stand-alone phase field models of magnetostrictive materials [128] and ferroelectric materials [129] developed in our group's previous works, which will be also described in the following.

## 2.1 Monolithic Ferroic Materials

### 2.1.1 Ferroelectric Materials

Phase field method describes the ferroelectric materials in a phenomenological way. Based on Ginzburg–Landau theory, the phase field approach considers evolution of the microstructures thermodynamically and kinetically. Thus the results obtained from phase field method are independent of any specific atomic structures. The total system free energy under externally applied electric field  $E^{\text{ex}}$  is [129]:

---

\* The material contained in Section 2.2.1 of this chapter was previously published in *Acta Materialia*, 70 (2014) 45–55, by Fengde D. Ma, Yongmei M. Jin, Yu U. Wang, Stephen L. Kampe, Shuxiang Dong. See Appendix A for documentation of permission to republish this material.

$$F = \int \left[ f(\mathbf{P}) + \beta |\nabla \mathbf{P}|^2 - \mathbf{E}^{\text{ex}} \cdot \mathbf{P} \right] d^3 r + \int \frac{d^3 k}{(2\pi)^3} \left[ \frac{1}{2\varepsilon_0} |\mathbf{n} \cdot \tilde{\mathbf{P}}|^2 + \frac{1}{2} K_{ijkl} \tilde{\varepsilon}_{ij} \tilde{\varepsilon}_{kl}^* \right], \quad (2.1)$$

where the function  $f(\mathbf{P})$  is Landau-Ginzburg-Devonshire energy of ferroelectric phase [150]:

$$\begin{aligned} f(\mathbf{P}) &= \alpha_1 (P_1^2 + P_2^2 + P_3^2) + \alpha_{11} (P_1^4 + P_2^4 + P_3^4) + \alpha_{12} (P_1^2 P_2^2 + P_2^2 P_3^2 + P_3^2 P_1^2) \\ &+ \alpha_{111} (P_1^6 + P_2^6 + P_3^6) + \alpha_{112} \left[ P_1^4 (P_2^2 + P_3^2) + P_2^4 (P_3^2 + P_1^2) + P_3^4 (P_1^2 + P_2^2) \right] \\ &+ \alpha_{123} P_1^2 P_2^2 P_3^2 \end{aligned} \quad (2.2)$$

The gradient terms of  $\mathbf{P}$  in Eq. (2.1) characterize energy contributions from polarization gradient in domain wall regions. The  $\mathbf{k}$ -space integral terms characterize the domain configuration-dependent energies of long-range electrostatic and elastostatic interactions, where  $\varepsilon_0$  are permittivity of free space,  $\tilde{\mathbf{P}}(\mathbf{k})$  and  $\tilde{\boldsymbol{\varepsilon}}(\mathbf{k})$  are the Fourier transforms of the respective field variables  $\mathbf{P}(\mathbf{r})$  and  $\boldsymbol{\varepsilon}(\mathbf{k})$ . The spontaneous strain  $\boldsymbol{\varepsilon}$  is a function of polarization  $\mathbf{P}$  resulting from electrostriction,  $\varepsilon_{ij} = Q_{ijkl} P_k P_l$ , where  $Q_{ijkl}$  is electrostrictive coefficient tensors.  $K_{ijkl} = C_{ijkl} - n_m C_{ijmn} \Omega_{np} C_{klpq} n_q$ ,  $\Omega_{ik} = (C_{ijkl} n_j n_l) - 1$ ,  $C_{ijkl}$  is elastic modulus tensor, and  $\mathbf{n} = \mathbf{k}/k$ . It's worth pointing out that the superscript asterisk \* indicates complex conjugate.

The domain evolution of polarization  $\mathbf{P}(\mathbf{r}, t)$  is governed by time-dependent Ginzburg-Landau equation [151],

$$\frac{\partial \mathbf{P}(\mathbf{r}, t)}{\partial t} = -L \frac{\delta F}{\delta \mathbf{P}(\mathbf{r}, t)} \quad (2.3)$$

where  $L$  is kinetic coefficient.

## 2.1.2 Magnetostrictive Materials

The phase field model of a magnetostrictive single crystal is formulated in terms of magnetization vector field  $\mathbf{M}(\mathbf{r})$ , which is the primary order parameter. The total system free energy  $F$  of a magnetostrictive material under externally applied magnetic field  $\mathbf{H}^{\text{ex}}$  is [128]:

$$\begin{aligned} F = & \int \left[ K_1 (m_1^2 m_2^2 + m_2^2 m_3^2 + m_3^2 m_1^2) + K_2 m_1^2 m_2^2 m_3^2 \right] d^3 r + \int \beta_M |\nabla \mathbf{M}|^2 d^3 r \\ & - \int \mu_0 \mathbf{H}^{\text{ex}} \cdot \mathbf{M}(\mathbf{r}) d^3 r + \frac{\mu_0}{2} \int \frac{d^3 k}{(2\pi)^3} |\mathbf{n} \cdot \tilde{\mathbf{M}}(\mathbf{k})|^2 + \frac{1}{2} \int \frac{d^3 k}{(2\pi)^3} K_{ijkl} \tilde{\varepsilon}_{ij} \tilde{\varepsilon}_{kl}^* \end{aligned} \quad (2.4)$$

where  $\mathbf{m} = \mathbf{M}/M$  is the magnetization direction.  $\mathbf{n} = \mathbf{k}/k$  is a unit vector in  $\mathbf{k}$ -space,  $\tilde{\mathbf{M}}(\mathbf{k})$  and  $\tilde{\varepsilon}(\mathbf{k})$  are the Fourier transform of the fields  $\mathbf{M}(\mathbf{r})$  and  $\varepsilon(\mathbf{r})$ , respectively, and the superscript asterisk  $*$  indicates complex conjugate. Resulting from magnetostriction, the spontaneous strain  $\varepsilon$  in magnetostrictive materials is a secondary order parameter and is coupled to the primary order parameter  $\mathbf{M}$  through magnetostriction coefficient tensor  $\lambda_{ijkl}$ :

$$\varepsilon_{ij} = \lambda_{ijkl} M_k M_l. \quad (2.5)$$



The integrand of the first energy term in Eq. (2.4), *i.e.*,  $K_1(m_1^2 m_2^2 + m_2^2 m_3^2 + m_3^2 m_1^2) + K_2 m_1^2 m_2^2 m_3^2$ , is the magnetocrystalline anisotropy energy where  $K_1$  and  $K_2$  are materials constants characterizing magnetocrystalline anisotropy. The gradient term,  $\beta_M |\nabla \mathbf{M}|^2$ , characterizes the energy contributions from the magnetization gradient (exchange energy) of the domain walls, where  $\beta_M$  is the exchange stiff constant. The two  $\mathbf{k}$ -space integrals in Eq. (2.4) give the magnetostatic energy of magnetic polarization distribution  $\mathbf{M}(\mathbf{r})$  and the elastostatic energy of magnetostrictive strain distribution  $\boldsymbol{\epsilon}(\mathbf{r})$ , respectively. The evolution of magnetization  $\mathbf{M}(\mathbf{r}, t)$  and its domains are respectively governed by the Landau-Lifshitz-Gilbert equation [152]:

$$\frac{\partial \mathbf{M}(\mathbf{r}, t)}{\partial t} = \gamma \mathbf{M} \times \frac{\delta F}{\delta \mathbf{M}(\mathbf{r}, t)} + \alpha \mathbf{M} \times \left[ \mathbf{M} \times \frac{\delta F}{\delta \mathbf{M}(\mathbf{r}, t)} \right], \quad (2.6)$$

where  $\gamma$  and  $\alpha$  are gyromagnetic ratio and damping parameter, respectively, of magnetization evolution.

## 2.2 Ferroic Composites

### 2.2.1 Magnetoelectric Composite

Both constituent phases in ME composites, namely, the magnetostrictive and ferroelectric phases, are ferroic materials whose macroscopic properties are determined by the underlying mesoscale evolution of magnetic and electric domains coupled with their respective secondary elastic domains due to magnetostriction and electrostriction. Such

domain processes sensitively depend on the composite microstructures (shape, size, distribution and orientation of the grains of the respective phases). In such situations, theoretical treatment merely based on constitutive equations of the constituent phases [54, 58, 113, 114, 116] is insufficient, and a computational approach is required that explicitly simulates the domain-level processes and mechanisms within realistic composite microstructures.

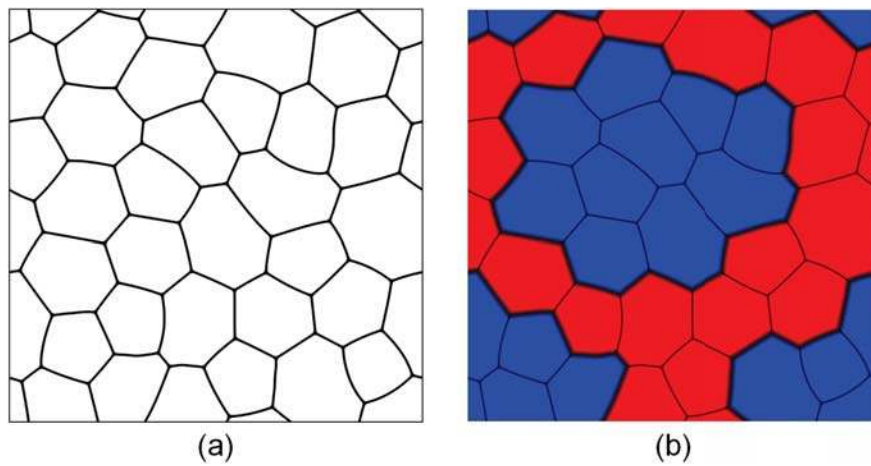


**Figure 2.1** (a) Grain structure and (b) phase morphology of particulate composite.

Computer modeling is developed by integrating our previously developed stand-alone phase field models of magnetostrictive materials [128] and ferroelectric materials [129]. In order to study the effects of electrical conductivity in ME composites, recently developed phase field modeling of current density distributions in complex microstructures [153] is also incorporated which solves the microscopic Ohm's law in the same phase field formalism as for magnetic, electric and elastic domain evolutions. The ME composite model describes the grain structure of two-phase particulate composites (as illustrated in

Figure 2.1) and the coupled evolutions of magnetic, electric and elastic domains, calculates heterogeneous distributions of local magnetic, electric and elastic stress/strain fields as well as current density distributions, from which detailed domain-level mechanisms are studied and effective ME coefficient of the composites is determined.

The grain structure of particulate composite is characterized by a grain rotation matrix field  $R_{ij}(\mathbf{r})$  that describes the geometry (size, shape, location) and crystallographic orientation of individual grains, as illustrated in Figure 2.1(a). The two-phase morphology of the composite is characterized by a phase field variable  $\eta(\mathbf{r})$  that distinguishes magnetostrictive grains ( $\eta=0$ ) and ferroelectric grains ( $\eta=1$ ), as illustrated in Figure 2.1(b), where blue and red coloring represent magnetostrictive and ferroelectric phases, respectively. The multiferroic state of such a ME composite is described by two vector fields and one scalar field, namely, magnetization  $\mathbf{M}(\mathbf{r})$ , polarization  $\mathbf{P}(\mathbf{r})$  and free charge density  $\rho(\mathbf{r})$ . The total system free energy under externally applied magnetic field  $\mathbf{H}^{\text{ex}}$  and electric field  $\mathbf{E}^{\text{ex}}$  is [128, 129]:

$$F = \int \left[ (1-\eta) f_M(R_{ij}M_j) + \eta f_E(R_{ij}P_j) + \beta_M |\nabla \mathbf{M}|^2 + \beta_E |\nabla \mathbf{P}|^2 - \mu_0 \mathbf{H}^{\text{ex}} \cdot \mathbf{M} - \mathbf{E}^{\text{ex}} \cdot \mathbf{P} \right] d^3r + \int \frac{d^3k}{(2\pi)^3} \left[ \frac{\mu_0}{2} |\mathbf{n} \cdot \tilde{\mathbf{M}}|^2 + \frac{1}{2\varepsilon_0} \left| \frac{\tilde{\rho}}{k} - i\mathbf{n} \cdot \tilde{\mathbf{P}} \right|^2 + \frac{1}{2} K_{ijkl} \tilde{\varepsilon}_{ij} \tilde{\varepsilon}_{kl}^* \right], \quad (2.7)$$

where  $f_M(R_{ij}M_j)$  and  $f_E(R_{ij}P_j)$  are the local free energy density functions that respectively define the thermodynamic properties of magnetostrictive and ferroelectric phases in individual grains. Both  $\mathbf{M}(\mathbf{r})$  and  $\mathbf{P}(\mathbf{r})$  are defined in a global coordinate system attached to the particulate polycrystalline sample instead of in a local coordinate system aligned

with  $\langle 100 \rangle$  lattice axes of the local crystal lattice. The operations  $R_{ij}M_j$  and  $R_{ij}P_j$  in the functions  $f_M(R_{ij}M_j)$  and  $f_E(R_{ij}P_j)$  transform  $\mathbf{M}(\mathbf{r})$  and  $\mathbf{P}(\mathbf{r})$  from the global sample system to the local crystallographic system in each grain. In a local crystallographic system,  $f_M(\mathbf{M})$  is formulated as the magnetocrystalline anisotropy energy [154]:

$$f_M(\mathbf{M}) = K_1(m_1^2m_2^2 + m_2^2m_3^2 + m_3^2m_1^2) + K_2m_1^2m_2^2m_3^2, \quad (2.8)$$

where  $\mathbf{m}=\mathbf{M}/M$  is the magnetization direction, and  $f_E(\mathbf{P})$  is formulated by the Landau-Ginzburg-Devonshire (LGD) polynomial energy:

$$\begin{aligned} f_E(\mathbf{P}) = & \alpha_1(P_1^2 + P_2^2 + P_3^2) + \alpha_{11}(P_1^4 + P_2^4 + P_3^4) + \alpha_{12}(P_1^2P_2^2 + P_2^2P_3^2 + P_3^2P_1^2) \\ & + \alpha_{111}(P_1^6 + P_2^6 + P_3^6) + \alpha_{112} \left[ P_1^4(P_2^2 + P_3^2) + P_2^4(P_3^2 + P_1^2) + P_3^4(P_1^2 + P_2^2) \right] \\ & + \alpha_{123}P_1^2P_2^2P_3^2 \end{aligned} \quad (2.9)$$

The gradient terms characterize the energy contributions from the magnetization gradient (exchange energy) and polarization gradient, respectively, of the domain walls. The  $\mathbf{k}$ -space integral terms characterize the domain configuration-dependent energies of the long-range magnetostatic, electrostatic and elastostatic interactions (within an elastic homogeneity assumption), where  $\mu_0$  and  $\varepsilon_0$  are permeability and permittivity of free space,  $\tilde{\mathbf{M}}(\mathbf{k})$ ,  $\tilde{\mathbf{P}}(\mathbf{k})$ ,  $\tilde{\rho}(\mathbf{k})$  and  $\tilde{\boldsymbol{\varepsilon}}(\mathbf{k})$  are the Fourier transforms of the respective field variables  $\mathbf{M}(\mathbf{r})$ ,  $\mathbf{P}(\mathbf{r})$ ,  $\rho(\mathbf{r})$  and  $\boldsymbol{\varepsilon}(\mathbf{r})$ . The spontaneous strain  $\boldsymbol{\varepsilon}$  is a function of magnetization  $\mathbf{M}$  and polarization  $\mathbf{P}$  resulting from magnetostriction and electrostriction,  $\varepsilon_{ij} = \lambda_{ijkl}m_k m_l + Q_{ijkl}P_k P_l$ , where  $\lambda_{ijkl}$  and  $Q_{ijkl}$  are magnetostrictive and electrostrictive

coefficient tensors, respectively. The evolution of magnetization  $\mathbf{M}(\mathbf{r}, t)$  and polarization  $\mathbf{P}(\mathbf{r}, t)$  and thus their domains are respectively governed by the Landau-Lifshitz-Gilbert equation [152] and the time-dependent Ginzburg-Landau equation :

$$\frac{\partial \mathbf{M}(\mathbf{r}, t)}{\partial t} = \gamma \mathbf{M} \times \frac{\delta F}{\delta \mathbf{M}(\mathbf{r}, t)} + \alpha \mathbf{M} \times \left[ \mathbf{M} \times \frac{\delta F}{\delta \mathbf{M}(\mathbf{r}, t)} \right], \quad (2.10)$$

$$\frac{\partial \mathbf{P}(\mathbf{r}, t)}{\partial t} = -L \frac{\delta F}{\delta \mathbf{P}(\mathbf{r}, t)}, \quad (2.11)$$

where  $\gamma$  and  $\alpha$  are gyromagnetic ratio and damping parameter, respectively, of magnetization evolution, and  $L$  is kinetic coefficient of polarization evolution. It is worth noting that, while the field variables  $\mathbf{M}(\mathbf{r}, t)$  and  $\mathbf{P}(\mathbf{r}, t)$  evolve according to separate equations, they are coupled within a ME composite by long-range elastic interaction through the spontaneous strain  $\varepsilon_{ij} = \lambda_{ijkl} m_k m_l + Q_{ijkl} P_k P_l$ , which produces coupled secondary elastic domains. The free charge density field  $\rho(\mathbf{r}, t)$  evolves while satisfying the law of charge conservation:

$$\frac{\partial \rho(\mathbf{r}, t)}{\partial t} = -\nabla \cdot \mathbf{j}(\mathbf{r}, t), \quad (2.12)$$

where the current density field  $\mathbf{j}(\mathbf{r}, t)$  follows the microscopic Ohm's law:

$$j_i = \sigma_{ik} E_k, \quad (2.13)$$

where the field variable  $\sigma_{ik}(\mathbf{r})$  describes the electrical conductivity distribution in the particulate ME composite and can be conveniently expressed in terms of the conductivities of respective constituent phases and the phase field variables  $R_{ij}(\mathbf{r})$  and  $\eta(\mathbf{r})$  [153]. The local electric field  $\mathbf{E}(\mathbf{r})$  is generated by both free charge density distribution  $\rho(\mathbf{r})$  and polarization distribution  $\mathbf{P}(\mathbf{r})$  as well as externally applied electric field  $\mathbf{E}^{\text{ex}}$  [153]:

$$\mathbf{E}(\mathbf{r}) = \mathbf{E}^{\text{ex}} - \frac{1}{\varepsilon_0} \int \frac{d^3k}{(2\pi)^3} \left[ \mathbf{n} \cdot \tilde{\mathbf{P}}(\mathbf{k}) + i \frac{\tilde{\rho}(\mathbf{k})}{k} \right] \mathbf{n} e^{i\mathbf{k} \cdot \mathbf{r}} . \quad (2.14)$$

The above-formulated model explicitly treats domain processes and grain structures in two-phase polycrystals and automatically takes into account the boundary conditions at inter-phase interfaces and grain boundaries of the ME composites. The phase field model is generally applicable to various forms of ME composites, such as particulate, laminar, layered and thin film nanostructured composites, where the microstructures of different forms are described by differing spatial features of the field variables  $R_{ij}(\mathbf{r})$  and  $\eta(\mathbf{r})$ .

It is worth noting that a similar phase field model of ME composites was reported recently, in which an order parameter field is used to describe the spatial distributions of the two constituent phases in the composite and the temporal evolutions of the magnetization and polarization fields in individual phases follow Landau-Lifshitz-Gilbert and time-dependent Ginzburg-Landau equations [155, 156]. However, the model does not address arbitrary grain orientations in particulate composite structures nor electrical

conductivity of magnetic phase, and was used to simulate film-substrate system [156] and 1-3 type bulk composite with ferroelectric rods of various cross-section shapes embedded in magnetic matrix [155]. It is also noteworthy that a different phase field approach to ME composites was also developed recently, which formulates a closed-form ME coefficient as a functional of the shape function that describes a spatial distribution of the phases, and the long-range dipole-dipole magnetostatic, electrostatic and elastostatic interactions are solved analytically within linear theory [157]. This approach uses a double-well potential, gradient term and ME coefficient to define a “virtual” free energy as a functional of the shape function, and employs a conserved Ginzburg-Landau-Khalatnikov equation to evolve the shape function and maximize ME coefficient, automatically reaching the optimal composite architecture [157]; however, domain-level processes are not addressed in this approach.

### **2.2.2 Polymer Matrix Ferroelectric Composite**

To describe the ferroelectric filler polymer matrix composite microstructure, a grain rotation matrix field  $R_{ij}(\mathbf{r})$  is used to characterize the geometry (size, shape, location) and crystallographic orientation of ferroelectric grains, and a phase field variable  $\eta(\mathbf{r})$  is used to characterize the ferroelectric particles ( $\eta=1$ ) embedded in polymer matrix ( $\eta=0$ ) [149, 158], as illustrated in Figure 2.2. The state of the composite is described by polarization vector field  $\mathbf{P}(\mathbf{r})$ .

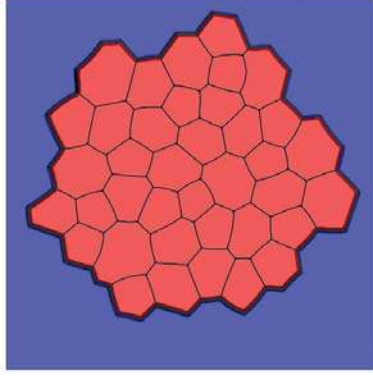


**Figure 2.2** Grain structure and phase morphology of a polymer matrix composite, visualized in a simulation cell with periodic boundary condition. Red and blue colors represent ferroelectric and matrix phases, respectively.

The total system free energy under externally applied electric field  $\mathbf{E}^{\text{ex}}$  is [159]:

$$F = \int \left[ \eta f(R_{ij}P_j) + \beta |\nabla \mathbf{P}|^2 - \mathbf{E}^{\text{ex}} \cdot \mathbf{P} \right] d^3r + \int \frac{d^3k}{(2\pi)^3} \left[ \frac{1}{2\epsilon_0} |\mathbf{n} \cdot \tilde{\mathbf{P}}|^2 + \frac{1}{2} K_{ijkl} \tilde{\epsilon}_{ij} \tilde{\epsilon}_{kl}^* \right], \quad (2.15)$$

where  $f(\mathbf{P})$  is Landau-Ginzburg-Devonshire energy function of ferroelectric phase. In Eq. (2.15),  $\mathbf{P}(\mathbf{r})$  is defined in a global coordinate system attached to the particulate composite instead of a local coordinate system aligned with  $\langle 100 \rangle$  lattice axes of a ferroelectric single crystal; the operation  $R_{ij}P_j$  in the free energy function  $f$  transforms  $\mathbf{P}(\mathbf{r})$  from global sample system to local lattice system in each grain. The gradient term characterizes energy contribution from polarization gradient in domain wall regions. The  $\mathbf{k}$ -space integral terms characterize the domain configuration-dependent energies of long-range electrostatic and elastostatic interactions, where  $\epsilon_0$  is permittivity of free space,  $\tilde{\mathbf{P}}(\mathbf{k})$  and  $\tilde{\epsilon}(\mathbf{k})$  are the Fourier transforms of the respective field variables  $\mathbf{P}(\mathbf{r})$  and  $\epsilon(\mathbf{r})$ . The spontaneous strain



$\boldsymbol{\varepsilon}$  is coupled to polarization  $\mathbf{P}$  through electrostriction coefficient tensor  $Q_{ijkl}$   
 $\varepsilon_{ij} = Q_{ijkl} P_k P_l$ . The evolution of polarization  $\mathbf{P}(\mathbf{r}, t)$  is governed by time-dependent  
Ginzburg-Landau equation, as shown in section 2.1.

# Chapter 3. Particulate Magnetoelectric Composite<sup>†</sup>

## 3.1 Introduction

Since the ME response of monophasic materials is either too weak or occurs at temperatures far below room temperature, such single phase materials have difficulty finding any practical engineering applications. An alternative is to use magnetostrictive - piezoelectric composites [160, 161] which are expected to give rise to an enhancement of ME effects. The extrinsic ME effect in composites is known as a product property that results from the elastic interaction between the magnetostrictive phase and the piezoelectric phase [162]. Thus the ME effect is a coupled electrical and magnetic phenomenon via elastic interaction. Due to the great design flexibility of composites, various ME composite connectivities (0-3, 1-3 and 2-2) have been experimentally studied in recent years.

In this chapter, we will focus on certain issues that are important for both rational design and practical application of 0-3 particulate ME composites, including the connectivity of constituent phases, the electrical conductivity of magnetostrictive phase, in-situ electric poling of ferroelectric phase within composite, and bias magnetic field during sensing. These issues are especially prominent in particulate composites [59, 65, 163].

---

<sup>†</sup> The material contained in this chapter was previously published in *Acta Materialia*, 70 (2014) 45–55, by Fengde D. Ma, Yongmei M. Jin, Yu U. Wang, Stephen L. Kampe, Shuxiang Dong. See Appendix B for documentation of permission to republish this material.

The ME composites will have realistic complex microstructures characterizing individual grain and phase morphologies. In addition to complicated grain structures, the particulates of different phases can develop different phase connectivities that can have important implications on composite properties [55]. Moreover, particulate composites are often synthesized by high-temperature sintering processes (above the Curie temperatures of both constituent phases); thus, the ferroelectric phase in the as-fabricated ME composites is usually unpoled and does not possess the necessary piezoelectric characteristics. In-situ electric poling of the ferroelectric grains within the particulate microstructure is thus necessary. It is worth noting that, unlike glued multilayer structures where the separate ferroelectric layers can be independently poled prior to their incorporation into a ME composite [39] (albeit such gluing procedure imposes limitations to the geometry and miniaturization of ME microstructures and devices), in-situ poling is necessary for all other forms of ME composites including particulate, co-sintered laminates, and self-assembled thin film nanostructures [39]. Therefore, in-situ poling is an important and critical issue worthy of detailed study. In this chapter, evolution of magnetic and electric domains and their associated magnetostriction and electrostriction under electric and/or magnetic fields in poling and sensing conditions will be simulated to study the strain-mediated domain-level coupling mechanisms between magnetization and polarization.

## 3.2 Model and Material Parameters

While various combinations of constituent phases have been used to synthesize ME composites,  $Tb_xDy_{1-x}Fe_2$  (Terfenol-D) [154] and  $Pb(Zr_{1-x}Ti_x)O_3$  (PZT) [164] are

considered as model magnetostrictive and ferroelectric materials in this study, whose material parameters have been determined by experiments and are used as input parameters to perform simulation study in this work. The material-specific input parameters are magnetocrystalline anisotropy constants  $K_1=-6\times 10^4$  J/m<sup>3</sup>,  $K_2=-2\times 10^5$  J/m<sup>3</sup>, saturation magnetization  $M_s=8\times 10^5$  A/m, magnetostrictive constants  $\lambda_{111}=1.64\times 10^{-3}$ ,  $\lambda_{100}=1\times 10^{-4}$  for Terfenol-D [154], and LGD coefficients  $\alpha_1=-2.67\times 10^7$  m/F,  $\alpha_{11}=-1.43\times 10^7$  m<sup>5</sup>/C<sup>2</sup>F,  $\alpha_{12}=1.57\times 10^7$  m<sup>5</sup>/C<sup>2</sup>F,  $\alpha_{111}=1.34\times 10^8$  m<sup>9</sup>/C<sup>4</sup>F,  $\alpha_{112}=1.17\times 10^9$  m<sup>9</sup>/C<sup>4</sup>F,  $\alpha_{123}=-4.77\times 10^9$  m<sup>9</sup>/C<sup>4</sup>F, electrostrictive constants  $Q_{11}=0.0966$  m<sup>4</sup>/C<sup>2</sup>,  $Q_{12}=-0.046$  m<sup>4</sup>/C<sup>2</sup>,  $Q_{44}=0.0819$  m<sup>4</sup>/C<sup>2</sup> for Pb(Zr<sub>0.5</sub>Ti<sub>0.5</sub>)O<sub>3</sub> [164, 165]. While it is straightforward to carry out simulations with other material-specific input parameters, the obtained results reflect general behavior of ME composites and the conclusions hold for all particulate ME composites.

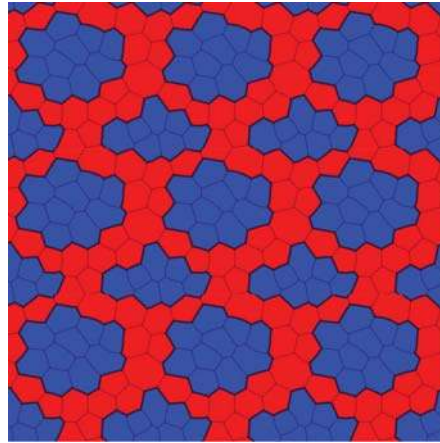


**Figure 3.1** Grain structure and phase morphology particulate composite, visualized in 3×3 simulation cells with periodic boundary condition. Red and blue colors represent matrix and filler phases, respectively.

Figure 3.1 shows the grain structure and phase morphology for a typical 0-3 particulate composite that will be used in the simulations, where blue and red colors represent filler and matrix phases, respectively. The computational results are presented and discussed in the following subsections. We will first describe (3.3) simulation procedure to study ME effect, and subsequently present the simulation results (3.4) and conclusion (3.5).

### 3.3 Simulation Procedure

The simulation procedure to study the composite-based ME effect is shown in Figures 3.2 and 3.3. In the first step, the composite is cooled through the Curie points (both magnetic and ferroelectric) to room temperature to attain an equilibrium domain structure, where both magnetic phase and ferroelectric phase are unpoled (the average magnetization and polarization are zero).

In the second step, an electric field of magnitude 100 kV/cm is applied to pole the ferroelectric grains within the particulate microstructure, and is maintained until new equilibrium domain structures are established. The average polarization ( $P_3$ ) and magnetization ( $M_1$ ) of the ME composite are shown in Figure 3.2(a,a'), where polarization reaches saturation under the poling field while magnetization remains close to zero; the corresponding ferroelectric and magnetic domain structures are shown in Figure 3.3(a,a'), where local polarization vectors are reoriented to follow continuous streamlines through the ferroelectric phase along the poling field direction as indicated by red arrow (except for

a few vortices formed at grain corners near inter-phase interfaces), while local magnetization vectors form closure domains within the polycrystalline magnetic phase.

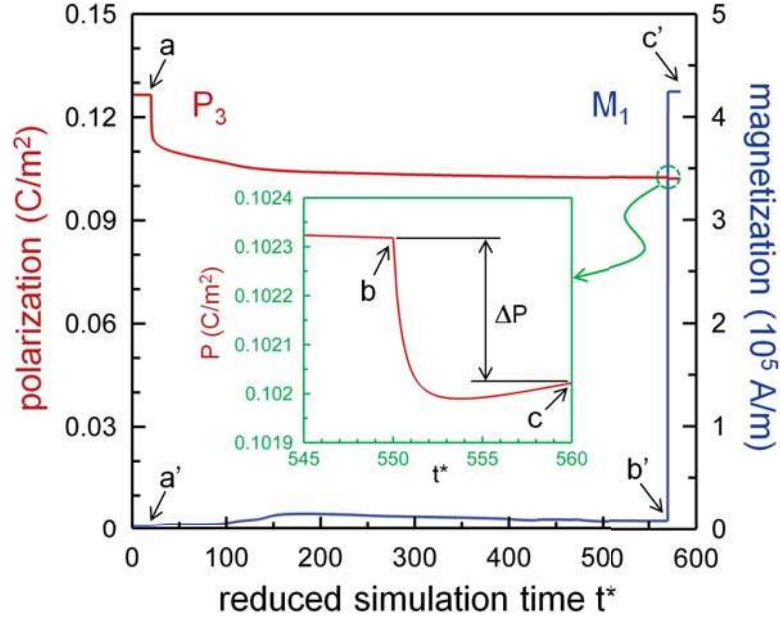


**Figure 3.2** Simulation procedure to study ME effect. Composite is poled under electric field (a), which is subsequently relaxed and remains poled upon removal of electric field (b). Magnetic field-induced polarization response is then simulated (c).

In the third step, the electric field is removed, and the domain structures are allowed to relax into a new equilibrium with the ferroelectric phase remaining poled, as shown in Figure 3.2(b,b'); the corresponding relaxed ferroelectric and magnetic domain structures are shown in Figure 3.3(b,b'), where the ferroelectric phase remains poled (except for a few more vortices formed upon removal of the electric field), and magnetic domains adjust into a better closure configuration (as illustrated by the magnetization streamlines).

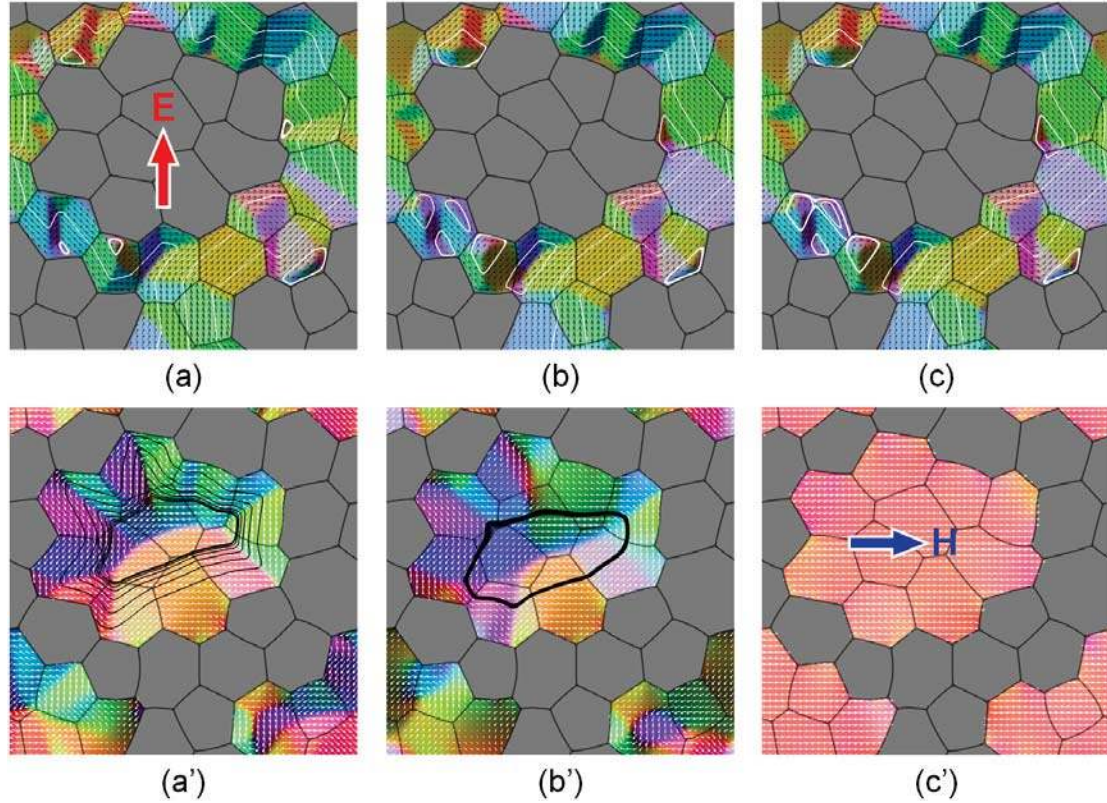


**Figure 3.3** Evolution of ferroelectric domains (a-c) and magnetic domains (a'-c') during the simulation process shown in Figure 3.2. Big red and blue arrows respectively indicate application of electric field (a,a') and magnetic field (c,c') and their directions. Small black and white arrows respectively represent polarization and magnetization distributions. Domain patterns are visualized by color maps with red, green, blue (RGB) components proportional to  $x$  (horizontal, right positive),  $y$  (vertical, up positive),  $z$  (normal, out of plane positive) components of polarization/magnetization vector.

In the fourth step, a magnetic field of magnitude  $10^6$  A/m is applied to magnetize the magnetostrictive phase and induce a polarization change, as shown in Figure 3.2(c,c'); the corresponding ferroelectric and magnetic domain structures are shown in Figure 3.3(c,c'), where local magnetization vectors are aligned along the magnetic field direction

as indicated by blue arrow, which generates magnetostrictive strain to elastically interact with the poled ferroelectric (now piezoelectric) phase, leading to a change in ferroelectric domain structure and polarization. Finally, the ME voltage coefficient  $\alpha$  is determined from this simulation procedure as  $\alpha = (\varepsilon_0 \varepsilon_r)^{-1} \Delta P / \Delta H$ , where  $\varepsilon_r$  is the relative permittivity of the composite. The domain evolution during above described simulation process and as shown in Figure 3 provides detailed insights into the underlying mechanisms responsible for the observed ME behavior that results.

The above-discussed simulation procedure will be employed to study the ME effect produced by particulate composites of varying constituencies and under various conditions. We will firstly investigate the effects of (3.4.1) in-situ poling of ferroelectric phase within composite microstructure, followed by (3.4.2) electrical conductivity of magnetic phase, (3.4.3) phase connectivity, and (3.4.4) bias magnetic field on the ME properties of the particulate composites.

## **3.4 Results and Discussion**

### **3.4.1 In-Situ Poling of Ferroelectric Phase within Composite Microstructure**

We will consider ME composites composed of ~50% volume fraction of each phase with randomly oriented equiaxed grains. The two-phase morphology with an isolated magnetic phase embedded in a continuous ferroelectric matrix (0-3 connectivity [55]) is firstly considered, as shown in Figure 3.1 (where the red represents ferroelectric in current



study). Three different constituent conditions are simulated, namely, (A) unpoled, (B) poled, and (C) poled with finite (nonzero) electrical conductivity of the magnetic phase. Under condition (A), the as-fabricated ME composites are simulated where the ferroelectric phase is unpoled thus does not exhibit piezoelectricity. Under condition (B), the ferroelectric grains are electrically poled in-situ within particulate two-phase microstructures. Under both (A) and (B) conditions, the magnetic phase is assumed to be nonconductive (zero electrical conductivity). To investigate the effect of electrical conductivity of magnetostrictive phase on the ME property, a finite (small but nonzero) conductivity is assumed for the magnetic phase under condition (C). It is worth noting that the magnetostrictive phases used in particulate ME composites generally possess lower electrical resistivity than the ferroelectric phases [39]. Such a small but nonzero electrical conductivity of magnetic phase will have a negligible effect over short time periods such as when sensing AC signals, assuming that free charge will not have sufficient time to redistribute due to the low conductivity. However, over long time periods such as during DC electrical poling of the ME composites, the finite electrical conductivity of the magnetostrictive phase is expected to allow free charge sufficient time to redistribute through magnetic phase. Such an effect is studied under condition (C) and can be directly compared with condition (B).

Depending on the directions of electric poling and magnetic field, ME coefficient is usually measured in longitudinal ( $\alpha_{33}$ ) or transverse ( $\alpha_{31}$ ) mode. Optimization of ME responses for longitudinal or transverse mode usually requires fabrication of ME composites with anisotropic two-phase microstructures and different phase connectivity,

such as 2-2 laminate and 1-3 fiber/rod composites [39]. The difference between  $\alpha_{33}$  and  $\alpha_{31}$  is not very significant in 0-3 particulate composites due to their more isotropic two-phase microstructures (our simulation study reveals that  $\alpha_{33}$  and  $\alpha_{31}$  of 0-3 particulate composites with isotropic two-phase microstructures can be effectively tailored via magnetic domain engineering to optimize ME responses without fabricating anisotropic two-phase microstructures, which will be presented in Chapter 4). In this chapter, we consider the transverse ME coefficient  $\alpha_{31}$  and use it to evaluate the effects of various factors addressed.

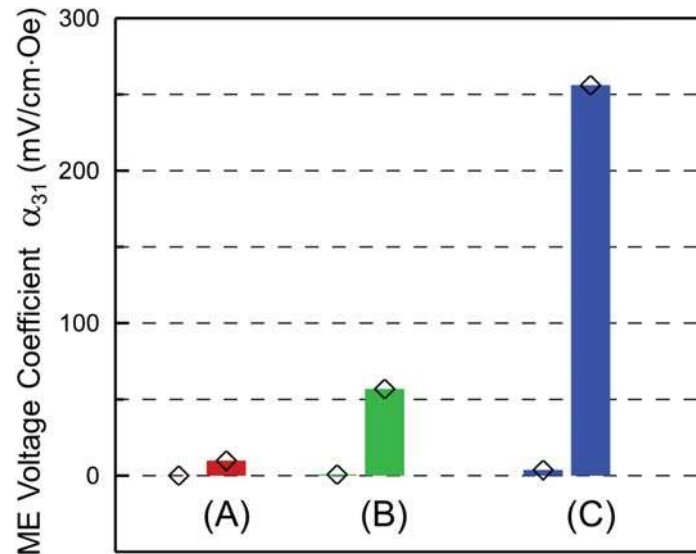


**Figure 3.4** Simulated ME voltage coefficient ( $\alpha_{31}$ ) of 0-3 particulate composites under different conditions: (A) unpoled, (B) poled, and (C) poled with finite (small but nonzero) electrical conductivity of isolated magnetic phase. For comparison,  $\alpha_{31}$  of 3-0 particulate composite under each condition is also shown to the left of each corresponding 0-3 composite.

The simulated ME voltage coefficient  $\alpha_{31}$  of 0-3 particulate composites under different conditions are compared in Figure 3.4. To simulate  $\alpha_{31}$ , the composite is poled vertically along axis 3 and the magnetic-field-induced polarization change  $\Delta P_3$  is measured in the same direction, where the magnetic field is applied horizontally along axis 1. The ME voltage coefficient is evaluated as  $\alpha_{31} = (\varepsilon_0 \varepsilon_r)^{-1} \Delta P_3 / \Delta H_1$ , where  $\varepsilon_r$  is the relative permittivity of the poled composite in axis-3 direction (after removal of the poling electric field). For the particulate ME composite with ~50% volume fraction of each phase considered here,  $\varepsilon_r \approx 140$  is obtained by simulating the polarization change in response to electric field applied along axis 3 (vertically) in the poled state ( $\varepsilon_r \approx 400$  in unpoled state, where the ferroelectric phase does not exhibit piezoelectricity, thus there is no ME effect in the composite). It is worth noting that the particulate ME composites illustrated in Figure 3.1 exhibit isotropic dielectric property in poled state, as shown by computer simulations ( $\varepsilon_r$  varies slightly within about 5% in different directions; in contrast, piezoelectric property is highly anisotropic) and also expected from random orientations of equiaxed grains.

It is also worth noting that 10 simulation cases are carried out for each condition, each with different random grain orientations to produce an averaged value. The average ME coefficients are plotted and shown in Figure 3.4 for comparison; the averaging procedure is necessary to obtain statistically meaningful results since a real ME particulate composite specimen consists of a large number of randomly oriented grains. However, due to limited computational power, only 32 grains are used to model the particulate

microstructure of composite; thus the averaging procedure improves the statistics of the simulation results and allows closer comparison between simulations and with experiments.

As shown in Figure 3.4, the unpoled composites under condition (A) exhibit a very weak ME effect (the nonzero  $\alpha_{31}$  value is due to the incomplete randomness of grain orientations sampled by the particulate structure models used in simulations), which is expected from the lack of piezoelectricity in unpoled ferroelectric phase. The domain structure in the unpoled ferroelectric phase within the ME composite is shown in Figure 3.5(A), where the polarization vectors form numerous vortices, and thus the ferroelectric phase does not possess macroscopic polarization, leading to lack of the piezoelectric effect.

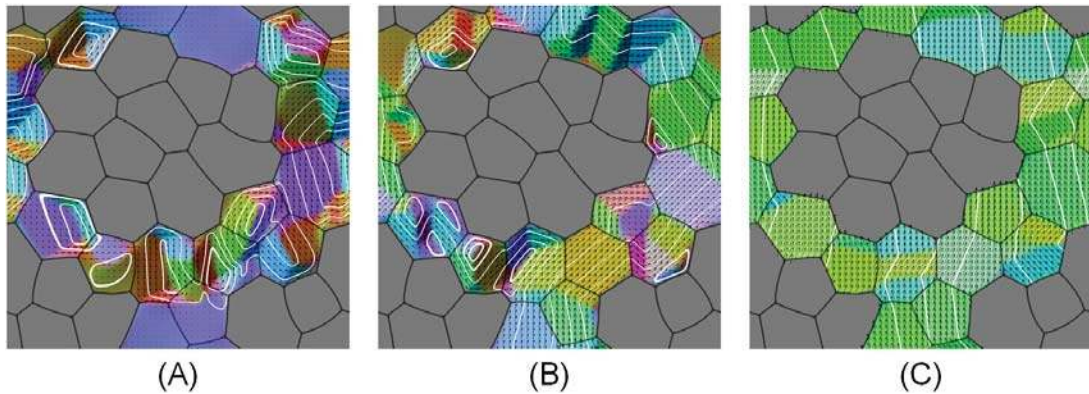


**Figure 3.5** Polarization distribution in continuous ferroelectric phase of 0-3 particulate ME composite under different conditions: (A) unpoled, (B) poled, and (C) poled with finite (small but nonzero) electrical conductivity of isolated magnetic phase. Small black arrows represent polarization distributions. Domain patterns are visualized by RGB color maps.

In contrast to unpoled ME composites, the poled composites under condition (B) exhibit the ME effect, as shown in Figure 3.4. The domain structure in poled ferroelectric

phase within the ME composite is shown in Figure 3.5(B), where polarization vectors orient to follow continuous streamlines through the ferroelectric phase along poling direction. Thus, the ferroelectric phase possesses macroscopic polarization and exhibits piezoelectricity; nevertheless, many vortices still form at grain corners near inter-phase interfaces. Therefore, the ferroelectric phase is not fully poled. Formation of polarization vortices helps eliminate spatial charges that would accumulate at the inter-phase interfaces, thus reducing electrostatic energy. A prominent feature of the domain structure in Figure 3.5(B) is that polarization streamlines are parallel to the inter-phase interfaces and never terminate at the interfaces and avoid interfacial charge accumulation.

### **3.4.2 Electrical Conductivity of Magnetic Phase**

As compared with poled ME composites with nonconductive magnetic phase, the poled composites under condition (C), i.e., with small but nonzero electrical conductivity of magnetic phase, exhibit significantly stronger ME effect, as shown in Figure 3.4. The mechanism responsible for such a drastic enhancement in ME coefficient is revealed by domain simulations.

The domain structure in the poled ferroelectric phase within the ME composite is shown in Figure 3.5(C), where polarization vectors are aligned in the poling direction, where the streamlines start and end at the inter-phase interfaces (without continuously running through the ferroelectric phase), and no polarization vortexes are formed; thus, the ferroelectric phase is fully poled and exhibits strong piezoelectricity. The fully polarized state of ferroelectric phase is achieved with the help of the nonzero conductivity of

magnetic phase which serves to redistribute the free charge to eliminate the bound charges accumulated at the interfaces caused by polarization terminations, thus removing the depolarization field to the ferroelectric phase. Such electrical conduction will be significant over the long time periods associated with the poling process, in spite of small (but finite) conductivity of magnetic phase. Therefore, the finite conductivity of magnetic phase enhances the piezoelectricity of the ferroelectric phase and the ME effect of the composites by both assisting effective poling and helping stabilize poled state of the ferroelectric phase. The simulations show that the ME voltage coefficient  $\alpha_{31}$  exhibits ~450% enhancement under condition (C) as compared to condition (B).

This result is contrary to conventional wisdom that regards conductivity in a magnetostrictive phase as detrimental to magnetoelectric composites. The simulations show that in-situ electric poling of ME composites is critically important for improving ME effect, and the small conductivity of the isolated magnetic phase of 0-3 particulate composites, if appropriately exploited, can produce a significant beneficial effect.

### **3.4.3 Phase Connectivity**

To further investigate the in-situ electrical poling and the effect of electrical conductivity in the magnetic phase, a two-phase morphology with an isolated ferroelectric phase embedded in continuous magnetic phase (3-0 connectivity) is also considered (as shown in Figure 1 but with the two phases exchanged, *i.e.*, red and blue colors now represent magnetostrictive and ferroelectric phases, respectively). The above three conditions (A)-(C) are again simulated, and the respective ME voltage coefficient  $\alpha_{31}$  of

3-0 composites is plotted in Figure 3.4 to the left of each corresponding 0-3 composite for comparison. It is clearly shown that 3-0 composites exhibit a vanishingly weak ME effect even under poled conditions (B) and (C).

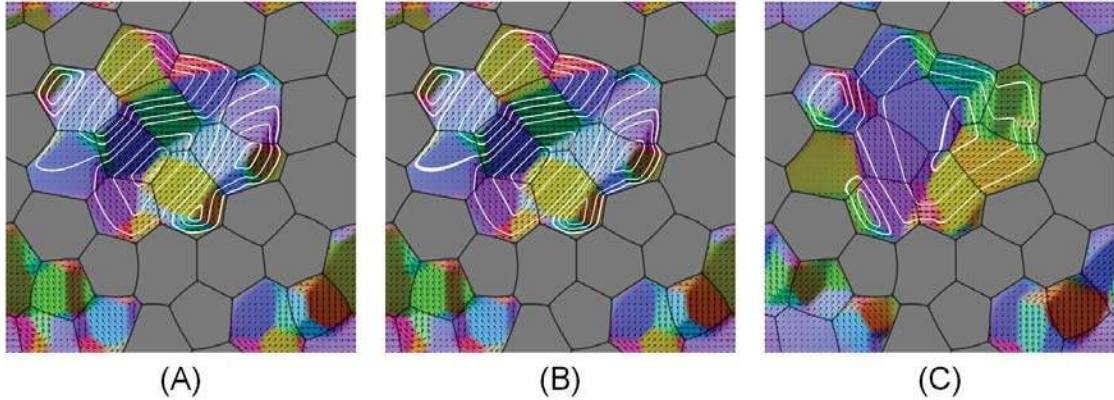


**Figure 3.6** Polarization distribution in isolated ferroelectric phase of 3-0 particulate ME composite under different conditions: (A) unpoled, (B) poled, and (C) poled with finite (small but nonzero) electrical conductivity of continuous magnetic phase. Small black arrows represent polarization distributions. Domain patterns are visualized by RGB color maps.

The simulated domain structures shown in Figure 3.6 reveal that the lack of ME response in 3-0 composites is due to the inability to in-situ pole the isolated ferroelectric phase embedded in continuous magnetic phase matrix, where polarization vectors always form vortices, thus the ferroelectric phase neither possesses macroscopic polarization nor exhibits piezoelectricity. Such unpoled state with vortex domains is a low-energy state determined by the electrical boundary condition at the inter-phase interfaces: under condition (B), *i.e.*, nonconductive magnetic phase, the accumulated bound charges at interfaces caused by polarization termination cannot be eliminated by free charges, which

generate internal electric field to depolarize the isolated ferroelectric phase, thus the polarization distribution returns to vortex domains upon removal of poling field.

On the other hand, under condition (C), the continuous magnetic phase of finite electrical conductivity prevents effective application of the electric poling field to the isolated ferroelectric phase; as a result, polarization vectors still form vortex domains, and the ferroelectric phase remains essentially unpoled. Therefore, 0-3 connectivity is required for particulate composites to produce ME effect, where the isolated magnetostrictive phase (0-connectivity) is embedded in continuous ferroelectric phase (3-connectivity), and where the ferroelectric phase is able to be poled in-situ within the composites no matter the magnetic phase possesses finite conductivity or not. The simulations show that the essential requirement for particulate ME composites is effective poling of the ferroelectric phase to exhibit strong piezoelectricity, and that the finite conductivity of isolated magnetic phase in 0-3 composites can help improve the poling and enhance the ME effect.

#### **3.4.4 Bias Magnetic Field**

Finally, the effect of bias magnetic field on the ME response of 0-3 composites under poled condition (B) is studied. The changes of magnetization ( $\Delta M_1$ ) and polarization ( $\Delta P_3$ ) are simulated as function of the externally applied magnetic field ( $H_1$ ), as plotted in Figure 3.7(a). A prominent observation is that under external magnetic field the polarization response markedly lags behind the magnetization response.



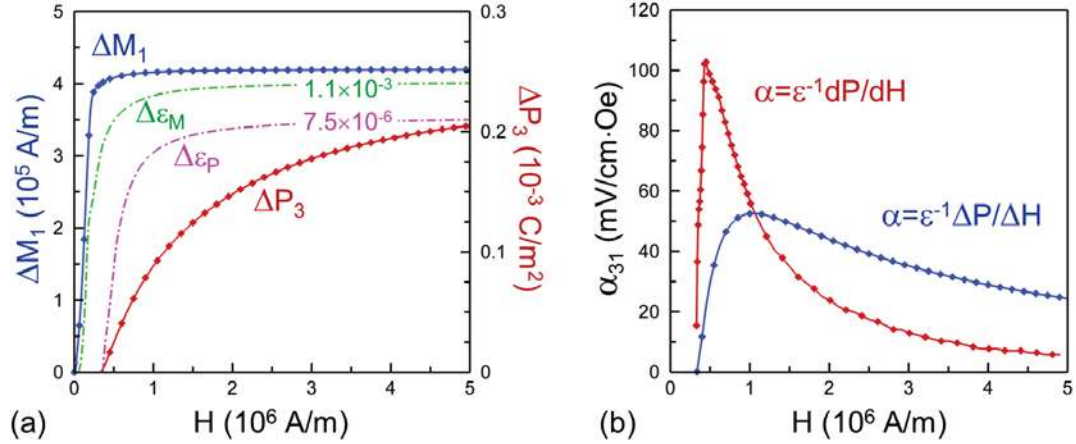


**Figure 3.7** Simulated magnetic, dielectric and magnetolectric responses of 0-3 particulate ME composite as function of externally applied magnetic field. (a) Changes of magnetization, polarization, magnetostrictive and electrostrictive strains (both  $\epsilon_{33}$  component) as induced by magnetic field. (b) Effect of bias magnetic field on magnetolectric coefficient.

The simulated magnetic domain process is shown in Figure 3.8. As seen from Figure 3.7(a) and Figure 3.8, the macroscopic magnetization approaches saturation and the internal magnetization vectors mostly switch to the external magnetic field direction after  $H=0.5 \times 10^6$  A/m). Nevertheless, the magnetization switching and saturation are not complete: the magnetization vectors near the inter-phase interfaces remain nonparallel to the external magnetic field direction, which gradually rotate towards magnetic field direction with increasing field even after  $H=1 \times 10^6$  A/m. While the contribution to the macroscopic magnetization is small during the gradual rotation of magnetization vectors near the interfaces, the associated magnetostrictive strain most efficiently interacts with the poled ferroelectric phase to induce a polarization response, producing a ME response. The

delayed polarization response markedly lagging behind magnetization response is a direct result of domain-level indirect coupling mechanism mediated through heterogeneous strain field, where the ME coupling depends on the efficacy of transferring magnetostrictive strain into electrostrictive strain via elastic interaction between the two constituent phases.

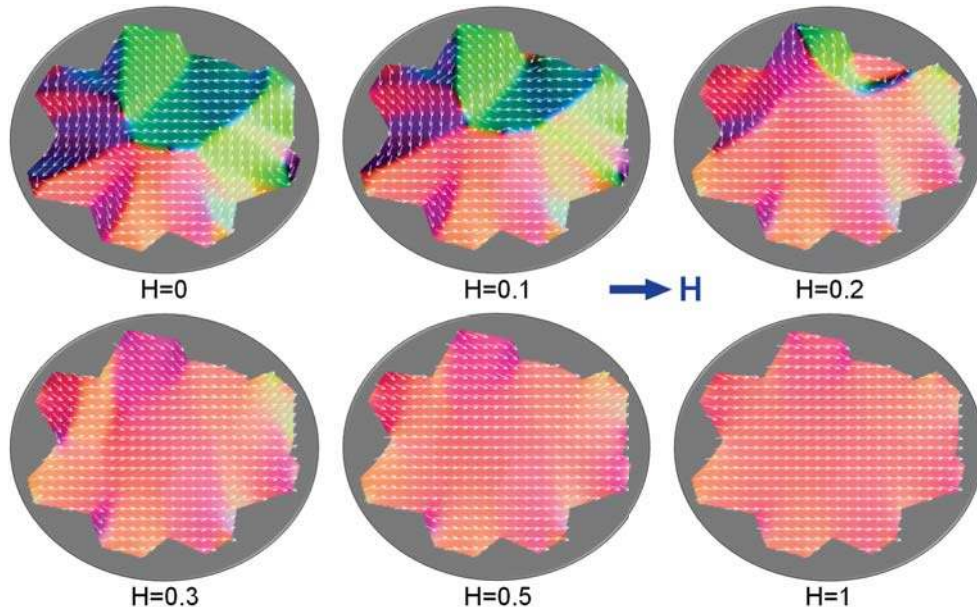


**Figure 3.8** Simulated magnetic domain evolution inside isolated magnetostrictive phase of 0-3 particulate ME composite in response to horizontally applied magnetic field  $H$  ( $\times 10^6$  A/m) as indicated by big blue arrow. Small white arrows represent magnetization distributions. Domain patterns are visualized by RGB color maps.

To illustrate the strain transfer behavior, the changes of the average magnetostrictive strain and electrostrictive strain versus the applied magnetic field are also plotted in Figure 3.7(a). Clearly, these strain changes are directly associated with the changes in magnetization and polarization; however, most of the magnetostrictive strain does not transfer into electrostrictive strain in the 0-3 particulate composites, resulting in

the electrostrictive strain (thus polarization) response lagging behind the magnetostrictive strain (thus magnetization) response. In particular, the magnetostrictive strain generated inside the polycrystalline magnetic particulate during  $H < 0.5 \times 10^6$  A/m does not interact strongly with the surrounding ferroelectric matrix, thus the composite lacks ME response under small magnetic field. It is the magnetostrictive strain generated near the inter-phase interfaces that is most efficient for the ME coupling.

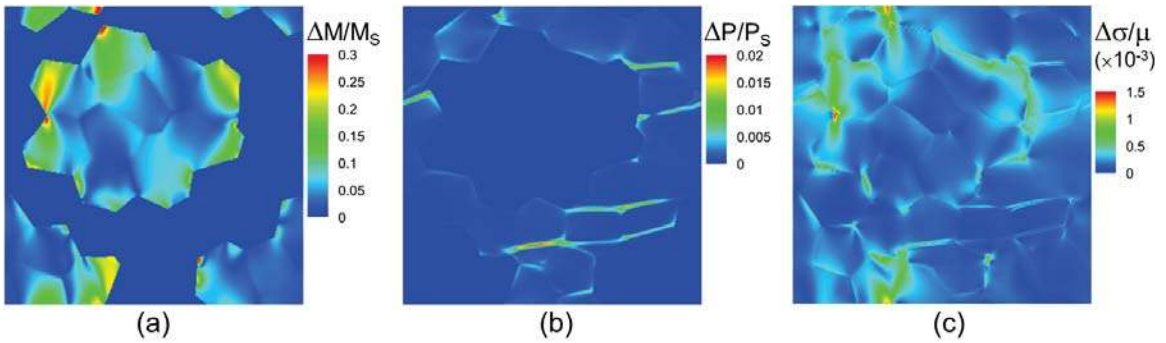


**Figure 3.9** Simulated changes of magnetization, polarization and stress in 0-3 particulate ME composite in response to increasing horizontal magnetic field from  $H=1 \times 10^6$  A/m to  $H=2 \times 10^6$  A/m). (a)  $\Delta M = \sqrt{\Delta M_k \Delta M_k}$  normalized by saturation magnetization  $M_s$ . (b)  $\Delta P = \sqrt{\Delta P_k \Delta P_k}$  normalized by spontaneous polarization  $P_s$ . (c)  $\Delta \sigma = \sqrt{\Delta \sigma_{ij} \Delta \sigma_{ij}}$  normalized by shear modulus  $\mu$ .

To demonstrate this effect, we plot the local changes in magnetization, polarization, and stress in the composite in Figure 3.9, corresponding to a change of magnetic field in horizontal direction from  $H=1 \times 10^6$  A/m to  $H=2 \times 10^6$  A/m (after macroscopic magnetization approaches apparent saturation). It clearly shows that, even the macroscopic magnetization does not increase appreciably after  $H=0.5 \times 10^6$  A/m, local magnetization vectors near the

inter-phase interfaces gradually rotate under increasing magnetic field, as shown in Figure 3.9(a) in agreement with the observation in Figure 3.8. Such magnetization change is accompanied by magnetostrictive strain change, which elastically interacts with the poled ferroelectric phase across the interface, causing polarization change near the interface (as well as along some grain boundaries and ferroelectric domain walls), as shown in Figure 3.9(b). Such elastic interaction is the strongest near the interface, as revealed in the stress change shown in Figure 3.9(c). It is expected that platelet two-phase morphology and multilayer architecture provide the most efficient strain-mediated ME coupling, in agreement with the theoretical prediction [157].

The apparently delayed polarization response lagging behind magnetization response implies that ME effect is highly nonlinear and sensitively depends on the external magnetic field, thus bias magnetic field can be used to effectively enhance the ME voltage coefficient, as shown in Figure 3.7(b), where the values of  $\alpha_{31}$  are calculated in two different ways from the simulated  $P$ - $H$  curve shown in Figure 3.7(a). In the first way, a differential scheme is used to obtain the “tangent” coefficient, as plotted in red curve in Figure 3.7(b), which reflects the effect of bias magnetic field on  $\alpha_{31}$ . It shows that a peak value can be achieved by applying an appropriate bias magnetic field ( $H \approx 0.5 \times 10^6$  A/m), which renders piezomagnetic response to the magnetostrictive phase. In the second way, a difference scheme is used to obtain the “secant” coefficient, as plotted in blue curve in Figure 7(b), which reaches a peak value at higher bias magnetic field ( $H \approx 1 \times 10^6$  A/m). Comparison of the ME coefficients as defined in the two ways shows that, while the

“tangent” coefficient reaches a higher peak value, it is also sensitive to the value of the bias field as reflected in the sharpness of the peak, thus best “tangent” coefficient would be difficult to exploit in practical applications. On the other hand, while the peak value of the “secant” coefficient is lower, it is also insensitive to the bias magnetic field, as reflected by the peak flatness of the blue curve in Figure 3.7(b). Thus, the “secant” coefficient would be more stable and more reliable in practice. For this reason, “secant” ME coefficients are compared in Figure 3.4 to study the ME composites under different conditions. It is worth noting that “tangent” and “secant” coefficients are measures of ME response respectively suitable for small and big signal sensing.

### **3.5 Conclusion**

Phase field modeling of ME composites is employed to perform a simulation study of some fundamental issues important for both rational design and practical application of ME composites.

It is found that in-situ electric poling of the ferroelectric phase within composite microstructures is crucial to obtaining the ME effect, 0-3 connectivity of isolated magnetostrictive phase embedded in continuous ferroelectric phase matrix is necessary for particulate ME composites, and small but finite electrical conductivity of isolated magnetic phase can beneficially enhance ME effect by both assisting effective poling and helping stabilize poled state of the ferroelectric phase. Optimum ME coefficient values can be achieved with appropriate bias magnetic field. The simulated evolution of magnetic and electric domains reveals complex domain-level strain-mediated coupling mechanisms

between magnetization and polarization. While these findings are obtained on particulate ME composites, they also shed useful light on other forms of ME composites.

# Chapter 4. Longitudinal and Transverse Responses of Particulate Magnetostrictive-Piezoelectric Composites<sup>‡</sup>

## 4.1 Introduction

As was discussed in previous chapters, magnetoelectric composites come in various forms, such as particulate, laminate, fiber/rod, and thin film nanostructure, which exhibit ME coefficients much higher than single-phase materials, thus promising significant technological potential. [39] Depending on the directions of electric poling and magnetic field, the ME coefficient is usually measured in longitudinal or transverse mode, each of which is convenient for a specific device design and a particular application. When poled along  $x_3$  axis, the longitudinal ( $\alpha_{E33}$ ) and transverse ( $\alpha_{E31}$ ) ME voltage coefficients are determined by applying the magnetic field respectively along  $x_3$  and  $x_1$ :  $\alpha_{E33} = (\varepsilon_0 \varepsilon_r)^{-1} \Delta P_3 / \Delta H_3$  and  $\alpha_{E31} = -(\varepsilon_0 \varepsilon_r)^{-1} \Delta P_3 / \Delta H_1$ , where  $\varepsilon_r$  is the relative permittivity of the composite measured along  $x_3$  (note that  $\Delta P_3 > 0$  in longitudinal mode while  $\Delta P_3 < 0$  in transverse mode). Optimization of ME responses for longitudinal or transverse mode usually requires fabrication of ME composites with anisotropic two-phase microstructures and different phase connectivity, such as 2-2 laminate and 1-3 fiber/rod composites.[55] In particular, 2-2 laminate composites exhibit a significantly higher

---

<sup>‡</sup> The material contained in this chapter was previously published in *Applied Physics Letters*, 104 (2014), 112903, by Fengde D. Ma, Yongmei M. Jin, Yu U. Wang, Stephen L. Kampe, Shuxiang Dong. See Appendix C and D for documentation of permission to republish this material.

transverse ME coefficient ( $\alpha_{31} > \alpha_{33}$ ) [75], while 1-3 fiber/rod composites exhibit a higher longitudinal ME coefficient ( $\alpha_{33} > \alpha_{31}$ ) [166]. In contrast, the difference between  $\alpha_{33}$  and  $\alpha_{31}$  is not so significant in 0-3 particulate composites due to their more isotropic two-phase microstructures.

It is desirable if the longitudinal and transverse ME responses of particulate composites could be effectively tailored without specially fabricating anisotropic two-phase microstructures, which would improve cost-performance ratio of ME composites. In this work we present a computational study of the effects of magnetic domain structures on the ME responses of 0-3 particulate composites, which reveals that the longitudinal and transverse ME coefficients of particulate composites with isotropic two-phase microstructures can be effectively tailored by engineering magnetic domains of magnetostrictive phase via controlling internal residual stress through appropriate processing, such as co-sintering under external stress (rather than isostatic pressing) in analogy to stress annealing of magnetostrictive materials.

## 4.2 Model and Material Parameters

As detailed in previous chapter, the same phase field model, simulation procedure and material parameters for magnetostrictive  $Tb_xDy_{1-x}Fe_2$  (Terfenol-D) [154] and ferroelectric  $Pb(Zr_{1-x}Ti_x)O_3$  (PZT) [164] model materials are used in this chapter.

Particulate ME composite of 0-3 phase connectivity and isotropic two-phase microstructure is considered. Figure 4.1 shows the grain structure and phase morphology,



where blue and red colors represent magnetostrictive and ferroelectric phases, respectively. To obtain isotropic composite microstructure, the two phases are such distributed in simulation cell that under periodic boundary condition the dispersed magnetostrictive particles form quasi-hexagonal arrangement embedded in ferroelectric matrix, as shown in Figure 4.1(b).

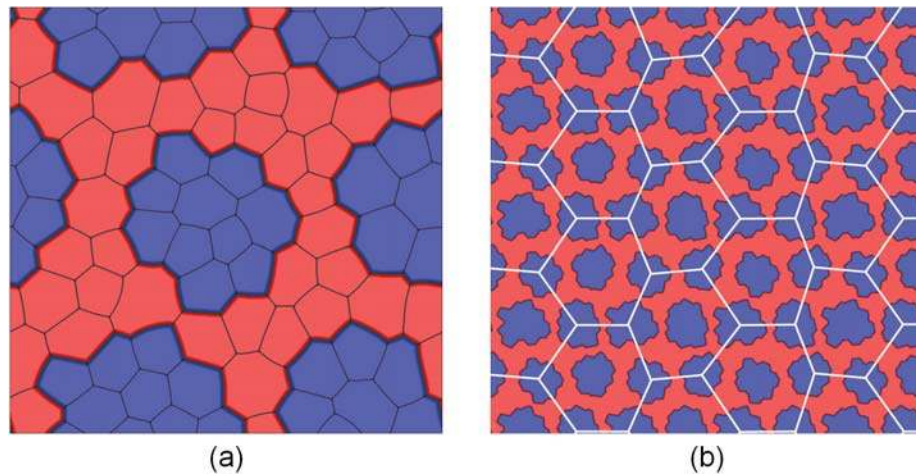


**Figure 4.1** Grain structure and phase morphology of 0-3 particulate composite with isotropic two-phase microstructure. (a) Simulation cell of particulate structure with periodic boundary condition. (b) Array of 4×4 cells illustrating quasi-hexagonal arrangement and nearly isotropic two-phase microstructure.

### 4.3 Simulation Procedure

Since particulate ME composites are synthesized via high-temperature sintering process (above the Curie temperatures of both constituent phases), the ferroelectric phase in the as-fabricated composites is unpoled thus does not possess the necessary piezoelectric property. In order to exhibit ME effect, in-situ electric poling of the ferroelectric grains within the composite microstructures is necessary, which requires 0-3 phase connectivity

with isolated magnetostrictive particles embedded in continuous ferroelectric matrix. The composite is poled along  $x_3$ -axis and remains poled after removal of electric field, as shown in Figure 4.2(a), where the polarization vectors of ferroelectric grains are reoriented towards the poling direction, rendering a macroscopic polar axis and piezoelectricity to the ferroelectric phase. As found in previous chapter, finite (small but nonzero) electrical conductivity of isolated magnetostrictive phase can produce beneficial effects during poling of 0-3 particulate composites by both assisting effective poling and helping stabilize poled state of ferroelectric phase. The poled ME composite is then subjected to a magnetic field that induces a polarization change, producing ME effect, as shown in Figure 4.2(b).

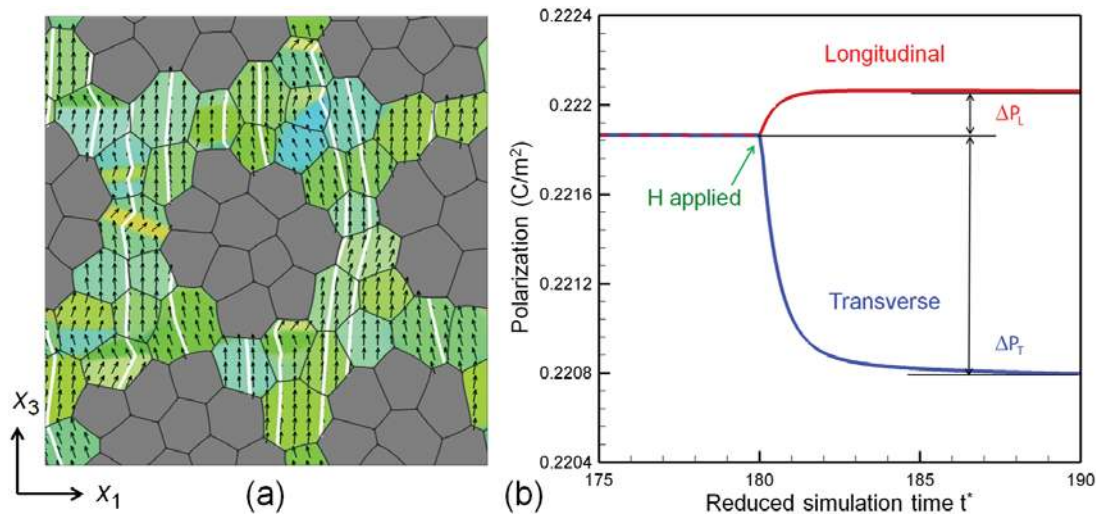


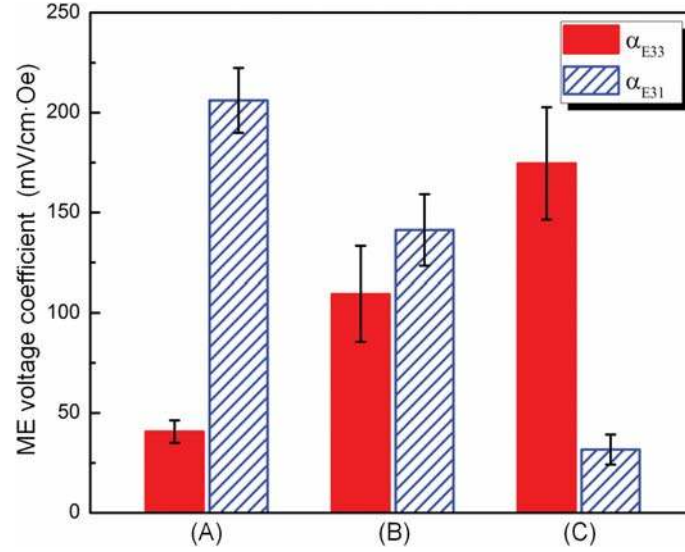
**Figure 4.2** (a) Polarization distribution in electrically poled (along  $x_3$ ) ferroelectric phase of 0-3 particulate ME composite. Domain patterns are visualized by color maps with red, green, blue (RGB) components proportional to  $P_x$ ,  $P_y$ ,  $P_z$ . (b) Simulation of magnetic field-induced polarization response in longitudinal and transverse mode, where magnetic field is applied at  $t^* = 180$  along  $x_3$  and  $x_1$ , respectively.

Applying the magnetic field respectively along  $x_3$  and  $x_1$ , longitudinal ( $\alpha_{E33}$ ) and transverse ( $\alpha_{E31}$ ) ME voltage coefficients are determined:  $\alpha_{E33} = (\varepsilon_0 \varepsilon_r)^{-1} \Delta P_3 / \Delta H_3$  and  $\alpha_{E31} = -(\varepsilon_0 \varepsilon_r)^{-1} \Delta P_3 / \Delta H_1$ , where  $\varepsilon_r$  is the relative permittivity of the composite measured along  $x_3$  (note that  $\Delta P_3 = \Delta P_L > 0$  in longitudinal mode while  $\Delta P_3 = \Delta P_T < 0$  in transverse mode). For the composite with ~50% volume fraction of each phase considered here (Figure 4.1),  $\varepsilon_r \approx 480$  is obtained by simulating polarization change in response to applied electric field in the poled state. The simulation procedure to study ME effect is the same as detailed in previous chapter.

## 4.4 Results and Discussion

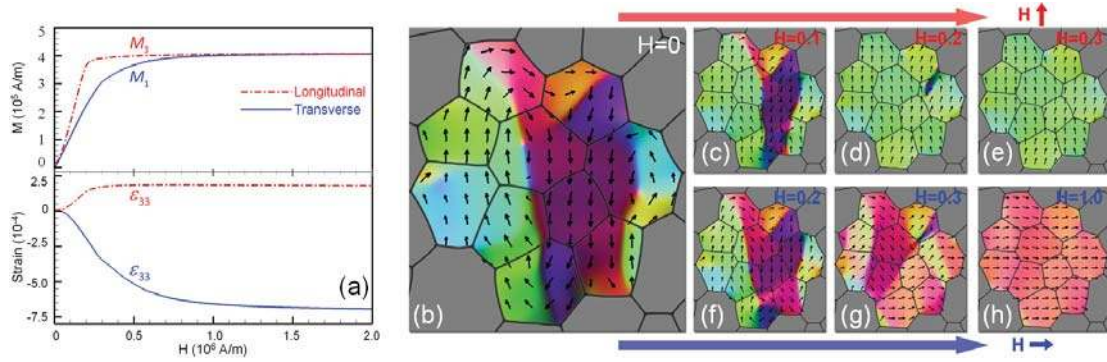
### 4.4.1 Dependence of ME Coefficients on Magnetic Domain Structure

Figure 4.3(A) compares the longitudinal and transverse ME voltage coefficients of the 0-3 particulate composites as determined by such simulations. It is worth noting that 5 simulations with different random grain orientations are carried out for each sensing mode, and both the average values and the variation ranges of the simulated ME voltage coefficients are plotted in Figure 4.3(A); such averaging procedure is necessary to obtain statistically meaningful results because a real ME particulate composite specimen consists of a large number of randomly oriented grains while, due to limited computational power, only 78 grains are used to model the particulate microstructure of the composite; thus averaging procedure improves the statistics of the simulation results.



**Figure 4.3** Simulated longitudinal and transverse ME voltage coefficients  $\alpha_{E33}$  and  $\alpha_{E31}$  of 0-3 particulate composites under different internal residual stress conditions: (A) non-engineered, (B) stress-relieved, and (C) residual stress-engineered.

As shown in Figure 4.3(A), the longitudinal coefficient  $\alpha_{E33}$  is much smaller than the transverse coefficient  $\alpha_{E31}$  in the 0-3 particulate ME composites. Their values are  $\alpha_{E33} = 40.6 \pm 5.6$  mV/cm·Oe and  $\alpha_{E31} = 206.1 \pm 16.2$  mV/cm·Oe. In order to clarify the underlying mechanisms responsible for such difference, the domain evolutions during above simulation procedure together with the corresponding responses of magnetization and magnetic field-induced strain are shown in Figure 4.4.



**Figure 4.4** (a) Simulated responses of magnetization and magnetic field-induced strain of 0-3 particulate composite in longitudinal and transverse sensing modes as function of applied magnetic field magnitude. Magnetic domain structure inside isolated magnetostrictive phase before application of magnetic field (b) and corresponding magnetic domain evolutions in longitudinal (c-e) and transverse (f-h) sensing modes with increasing magnetic field. Domain patterns are visualized by color maps with red, green, blue (RGB) components proportional to  $M_x, M_y, M_z$ .

As shown in Figure 4.4(a), the magnetic field-induced strain is much smaller in longitudinal mode than in transverse mode. Since ME effect in composite materials results from strain-mediated domain-level coupling between magnetization and polarization, smaller strain in longitudinal mode leads to weaker coupling thus smaller longitudinal ME voltage coefficient. The simulated magnetic domain structures and evolutions as function of applied magnetic field are shown in Figures 4.4(b-h). Figure 4.4(b) shows the magnetic domain structure before application of magnetic field, where a marked feature is the alignment of magnetization along  $\pm x_3$ -axis with predominant  $180^\circ$  domain walls oriented along  $x_3$ -axis. Such initial magnetic domain structure results from the strain-mediated elastic interaction between magnetostrictive phase and electrically poled ferroelectric

phase shown in Figure 4.2(a). Because the ferroelectric phase is poled along  $x_3$ -axis, it elongates in this poling direction due to electrostriction; as a result, the magnetostrictive particulates are stretched by the ferroelectric matrix along poling direction, resulting in magnetization alignment and  $180^\circ$  domain wall formation. In longitudinal mode, applied magnetic field mostly drives  $180^\circ$  domain wall motion, as shown in Figure 4.4(c-e), which does not contribute much to the change in magnetostriction strain, as shown in Figure 4.4(a), thus resulting in a small polarization change shown in Figure 4.2(b). In contrast, application of magnetic field in transverse mode rotates magnetization and drives domain switching via non- $180^\circ$  domain wall motion, as shown in Figure 4.4(f-h), leading to significant changes in magnetostriction strain and polarization, as shown in Figure 4.4(a) and Figure 4.2(b), respectively.

Above simulation results show that ME responses depend on the magnetic domain structures of magnetostrictive phase. It suggests that longitudinal and transverse ME coefficients of 0-3 particulate composites with isotropic two-phase microstructures can be tailored if magnetic domain structures can be engineered. One way to engineer the magnetic domain structures is through control of internal residual stress in the composites by appropriate processing, such as co-sintering under uniaxial or biaxial stress (rather than isostatic pressing), which produces similar effects as stress annealing of magnetostrictive materials for domain engineering and property optimization. [167] Co-sintered composites without special stress control is labeled as non-engineered condition (A) in Figure 4.3.

## 4.4.2 Magnetic Domain Engineering

To support our idea of tailoring ME properties via magnetic domain engineering by controlling internal stress in the particulate composites, we carry out more simulations under stress-relieved (B) and residual stress-engineered (C) conditions. As compared to condition (A), the internal residual stress in the magnetic phase is relieved under condition (B) while a compressive residual stress in  $x_3$  direction is engineered into the magnetic phase under condition (C). Control of internal residual stress is achieved in phase field modeling and simulation by introducing additional misfit strain between the two phases as in previous report [168].

The longitudinal and transverse ME voltage coefficients under three internal residual stress conditions (A-C) are plotted in Figure 4.3 for comparison. Under stress-relieved condition (B),  $\alpha_{E33}$  and  $\alpha_{E31}$  are nearly the same, while under residual stress-engineered condition (C) the longitudinal  $\alpha_{E33}$  becomes much larger than the transverse  $\alpha_{E31}$ , which is in sharp contrast to the condition (A). Figure 4.5 shows the magnetic domain structures under conditions (B) and (C) before application of magnetic field. In contrast to the domain structure under condition (A) shown in Figure 4.4(b), vortex domains without preferred magnetization direction are formed under stress-relieved condition (B) as shown in Figure 4.5(a), which is similar to the domain structure in stress-free particles; [169] since domain switching involves motions of both  $180^\circ$  and non- $180^\circ$  domain walls in both longitudinal and transverse modes, the magnetic field-induced strain thus strain-mediated ME coupling are similar, leading to similar values of  $\alpha_{E33}$  and  $\alpha_{E31}$ . On the other hand, the

engineered residual stress in condition (C) produces magnetization alignment and predominant  $180^\circ$  domain walls along  $x_1$ -axis, as shown in Figure 4.5(b), just opposite to condition (A), leading to longitudinal  $\alpha_{E33}$  much larger than transverse  $\alpha_{E31}$ , while the domain-level coupling mechanisms are the same as discussed for condition (A).

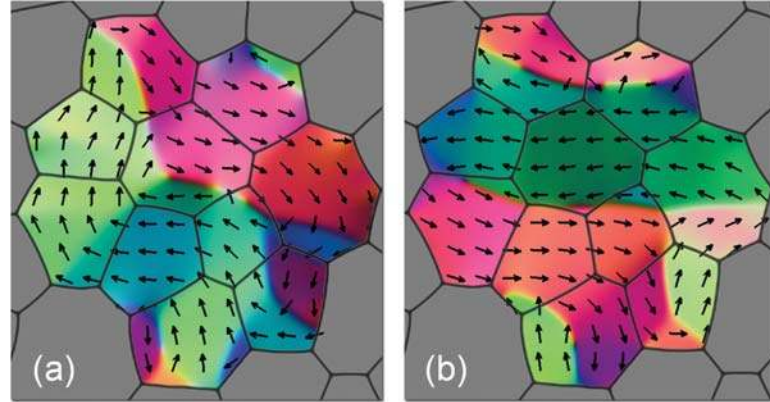


**Figure 4.5** Engineered magnetic domain structures in magnetostrictive phase under different internal residual stress conditions: (a) stress-relieved; (b) residual stress-engineered. Domain patterns are visualized by RGB color maps.

## 4.5 Conclusion

In summary, computer modeling and simulation reveals significant effects of magnetic domain structures on the ME responses of particulate composites. It is shown that longitudinal and transverse ME coefficients of 0-3 particulate composites with isotropic two-phase microstructures can be effectively tailored by controlling magnetic domain structures via internal residual stress engineering without resort to anisotropic two-phase microstructures (*e.g.*, 2-2 laminate, 1-3 fiber/rod). It suggests that co-sintering under uniaxial or biaxial stress rather than isostatic pressing is an effective route to engineer



internal residual stress and magnetic domain structures of particulate ME composites, which may also offer a means to help eliminate cumbersome external bias magnetic field that is usually required to achieve optimal material response.

# Chapter 5. Particulate Ferroelectric Ceramic-Polymer Matrix Composites<sup>§</sup>

## 5.1 Depolarization Effect

### 5.1.1 Introduction

The spontaneous polarization in ferroelectrics implies a hysteresis effect, which is a primary characteristic and the key property of ferroelectric materials. From the hysteresis loop, which describes the switching behavior of spontaneous polarization, a number of primary ferroelectric properties of a material can be determined such as the remanent polarizations (the polarization  $\mathbf{P}$  after the applied field  $\mathbf{E}^{\text{ex}}$  is removed) and the coercive fields (the amount of reverse electric field which must be applied to make the polarization return to zero). The understanding and control of ferroelectric hysteresis have always been an important and difficult undertaking from both theoretical and practical point of view.

[170]

Ferroelectric ceramic-polymer composites represent one of the most important technologies developed to broaden the application of conventional ferroelectrics. They offer several distinct advantages, such as the ease of manufacture and flexibility, broad bandwidth, low electrical losses, *etc.* The polymer-matrix composites can be manufactured

---

<sup>§</sup> The material contained in Section 5.1 of this chapter will be published in *Depolarization Field Effect on Dielectric and Piezoelectric Properties of Particulate Ferroelectric Ceramic-Polymer Composites: Phase Field Modeling*, by Fengde D. Ma, Yu U. Wang; The material contained in Section 5.2 of this chapter will be published in *Field-Induced Ferroelectric Phase Transition and Nonlinear Dielectric Behavior of Paraelectric Polycrystals: Phase Field Modeling*, by Fengde D. Ma, Yu U. Wang.

economically with properties tailored through microstructure control. In particulate, the mechanical and electrical properties of composites are highly dependent on the degree and type of connectivity of ferroelectric phase. There are 16 possible connectivity patterns [171], of which 0-3 connectivity is the most fundamental and practical type [106]. Plenty of experimental reports [172-174] have been found employing the 0-3 ferroelectric composite, due to different reasons.

Domains are essential feature of ferroelectrics. The hysteresis is believed to originate from the underlying domain switching processes and domain wall motion.[170] Our previous work discovered that the domain behaviors are sensitive to the internal boundary conditions at inter-phase interfaces and grain boundaries in the ferroelectrics [159, 175]. As to the 0-3 ferroelectric composite, the dynamic domain processes can be different due to the charges trapped in the ceramic/polymer interfaces. However, there are not many reports found concerning such fundamental issues as grain size or particle size at mesoscale domain levels.

This chapter will present a computational study of the dielectric and piezoelectric properties of ferroelectric ceramic particle-filled polymer-matrix composites. We focus on the effects of size, shape, internal grain structure, and spatial arrangement of the ferroelectric ceramic particulates on the composite properties. It's also suggesting that the ferroelectric behavior can be effectively tailored by changing the electric conductivity of polymer matrix.

### 5.1.2 Material Parameters and Simulation Procedure

To perform the computational study, a phase field model of ferroelectric ceramic particle-filled polymer-matrix composites is developed, as stated in Chapter 2. As shown in Chapter 3, the connectivity of the ferroelectric phase in a composite microstructure plays a critical role. This study reveals that the macroscopic dielectric and piezoelectric properties of the composites are dominated by depolarization field effect, which depends on the arrangement, alignment and connectivity rather than the size or internal grain structure of the ferroelectric ceramic particles. In this work we consider ferroelectric particles of  $\text{Pb}(\text{Zr}_{1-x}\text{Ti}_x)\text{O}_3$  (PZT) phase with composition  $x=0.6$ , whose materials parameters have been experimentally determined.

To simulate the dielectric and piezoelectric properties of ferroelectric composites, the material is first cooled across Curie point down to room temperature to form an equilibrium domain structure. Then a varying electric field  $E$  is applied to the material, and polarization  $P$  and strain  $\varepsilon$  are measured as functions of electric field  $E$ . A loading rate of 10 V/cm per simulation step is used that allows the domain structure to fully evolve in response to the varying electric field. For comparison, the hysteresis loops of  $P$ - $E$  and  $\varepsilon$ - $E$  curves are first simulated for a monolithic ferroelectric polycrystal, as plotted in Figure 5.1, where the domain microstructures at typical evolution stages as highlighted by numbers on the hysteresis loops are also shown. The state 1 corresponds to initially unpoled domain structure without macroscopic polarization, the state 3 corresponds to the poled domain structure with remanent polarization, and the states 2 and 4 show the fully poled domain

structures with aligned polarizations under saturation electric field along opposite directions. The hysteresis loops and domain structures shown in Figure 5.1 will serve as comparison basis for the following study of depolarization field effects on the dielectric and piezoelectric properties of ferroelectric ceramic particle-filled polymer-matrix composites.

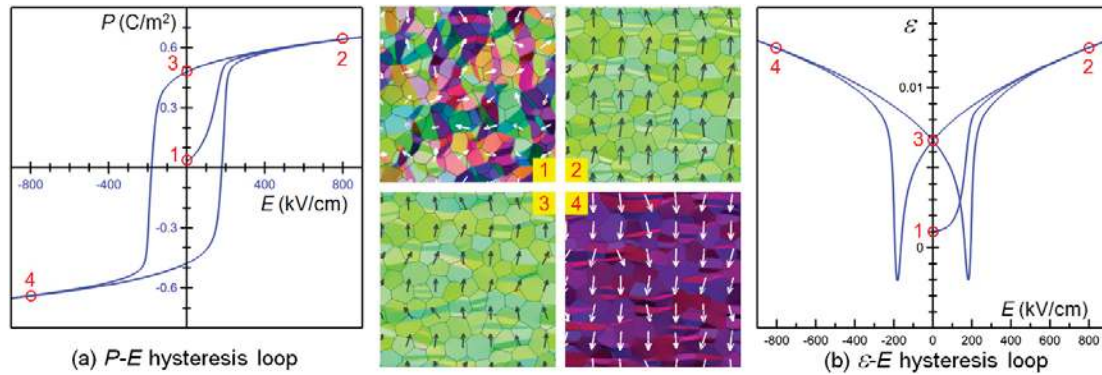


**Figure 5.1** Simulated dielectric and piezoelectric properties and corresponding domain processes in monolithic ferroelectric polycrystal. (a) Polarization-electric field ( $P$ - $E$ ) hysteresis loop. (b) Strain-electric field ( $\epsilon$ - $E$ ) hysteresis loop. (1-4) Domain microstructures at typical evolution stages as highlighted on the hysteresis loops. Small arrows represent polarization distribution. Domain patterns are visualized by color maps with red, green, blue (RGB) components proportional to  $P_x, P_y, P_z$ .

## 5.1.3 Results and Discussion

### 5.1.3.1 Effect of Grain Size and Particle Size

Figure 5.2 shows the simulated  $P$ - $E$  hysteresis loops for the ferroelectric ceramic particle-filled polymer-matrix composites of different grain sizes or particle sizes while the ferroelectric phase volume fraction remains the same in each case. To investigate the individual roles of grain size and particle size in particulate composites Figure 5.2 (a)

shows the results for different grain sizes while the particle size remains the same, while Figure 5.2 (b) shows the results for different particle sizes while the grain size remains the same. It is found that the grain size does not produce any effect, and the particle size plays a very minor effect (such minor effect has been shown to be attributed to variation in particle dispersion in the matrix). More importantly, linear dielectric behavior is observed, which does not exhibit any typical hysteresis features of monolithic ferroelectric polycrystal as shown in Figure 5.1.

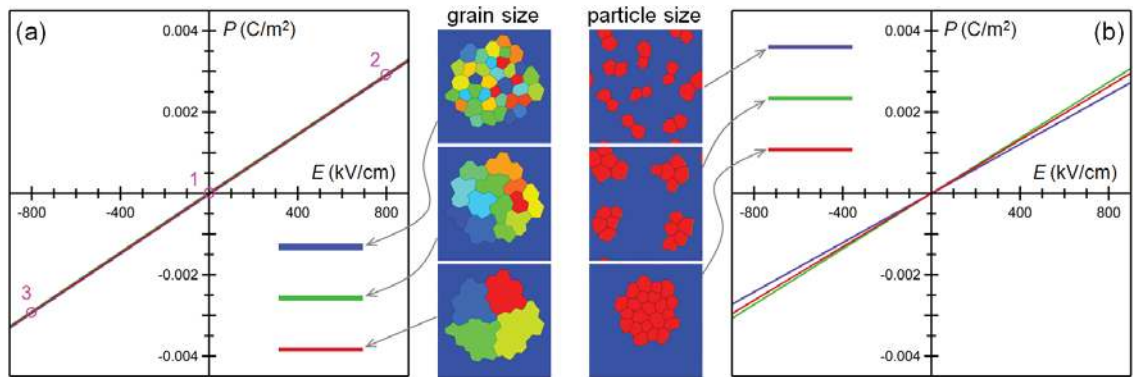


**Figure 5.2** Simulated  $P$ - $E$  hysteresis loops for composites of (a) different grain size but same particle size and (b) different particle size but same grain size, where the ferroelectric phase volume fraction remains the same.

To understand the lack of effects from grain size and particle size as well as linear anhysteretic dielectric response, the domain microstructures in the large ferroelectric particle of small grains at typical evolution stages as highlighted by numbers in Figure 5.2 (a) are shown in Figure 5.3. It is found that the equilibrium domain structure in the state 1 hardly evolves under external electric field as shown in the states 2 and 3. The lack of internal domain response to external electric field is due to the strong depolarization effect

that prevents change in local polarization. In an isolated ferroelectric particle embedded in polymer matrix, the equilibrium domain structure is formed to minimize the electrostatic and elastostatic energies. In particular, the electrostatic energy is minimized by eliminating the charge accumulation at particle interface that would produce large internal electric field in the particle (i.e., depolarization field). The local polarization vectors in the equilibrium domain structure would respond to an external electric field; however, the polarization change will generate interfacial charges thus increases the depolarization field and electrostatic energy. As a result of such a depolarization field effect, the local polarization response to external electric field is very weak. The same observation holds for isolated ferroelectric particles of different sizes and grain structures shown in Figure 5.2. Consequently, the particulate composites behave like linear dielectric materials in spite of ferroelectric particles. The field-induced macroscopic polarization (averaged in the ferroelectric particle) is very weak ( $<0.004 \text{ C/m}^2$ ) as compared with that in monolithic ferroelectric polycrystal ( $\sim 0.6 \text{ C/m}^2$ ) under the same applied electric field  $800 \text{ kV/cm}$ .

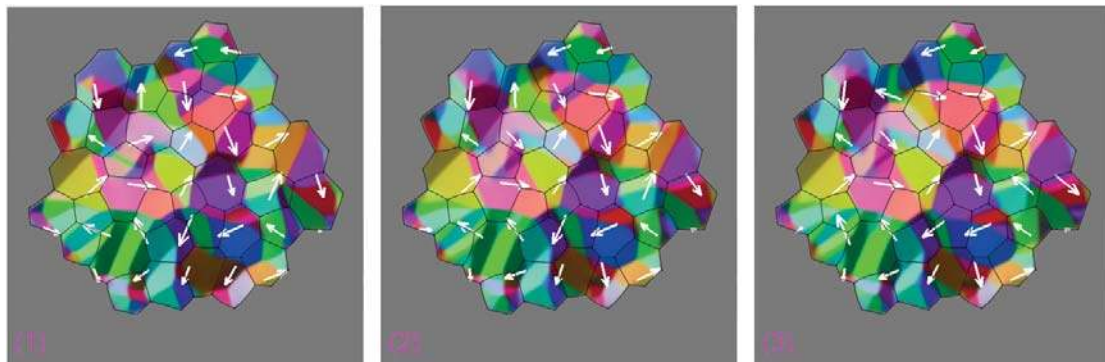


**Figure 5.3** Simulated domain microstructures in large ferroelectric particle of small grains in the composite at typical evolution stages under external electric field as highlighted on

the  $P$ - $E$  curve in Fig. 3(a). Small arrows represent polarization distribution. Domain patterns are visualized by color maps with RGB components proportional to  $P_x, P_y, P_z$ .

### 5.1.3.2 Effect of Shape of Alignment

Above results show that the depolarization field effect plays a decisive role in determining the macroscopic response of particulate composites. In order to fully exploit the properties of the ferroelectric particles embedded in the polymer matrix, depolarization field effect needs to be controlled. Our previous work has demonstrated that particle shape, arrangement and alignment have significant effects on the composite properties.[158] In particular, the connectivity of ferroelectric phase is of critical importance. To investigate these structural factors, we simulate the composites of same ferroelectric phase volume fraction but with different particle microstructures and compare their  $P$ - $E$  responses in Figure 5.4.

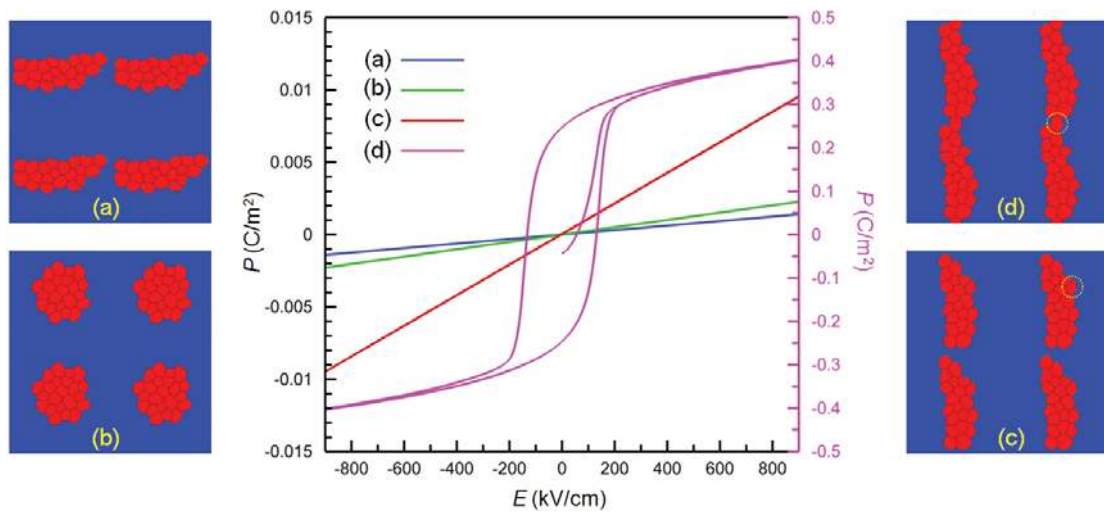


**Figure 5.4** Simulated  $P$ - $E$  hysteresis loops for composites of different particle shape and phase connectivity. The ferroelectric phase volume fraction remains the same.



It is found that the composites with isolated particles always exhibit linear anhysteretic dielectric response, irrespective of particle shapes. Nevertheless, the composite with particles of larger aspect ratio aligned along the applied electric field direction exhibits stronger dielectric response than those with smaller particle aspect ratios, as shown in Figure 5.4(c) versus in Figure 5.4(a, b). This difference is attributed to the depolarization field effect, where the depolarization factor depends on the shape (aspect ratio) of the isolated particles: particles with larger aspect ratio aligned along the applied electric field direction have lower depolarization factor and experience weaker depolarization field effect, which enable the particles to develop stronger local polarization response to the external electric field, as visualized by the domain structure in Figure 5(a). Thus, the shape and alignment of the ferroelectric particles play more important roles than the particle size and grain structures. In particular, the composite with aligned particles of large aspect ratio shown in Figure 5.4(c) exhibits 3-fold increase in dielectric constant than that with equiaxed particles shown in Figure 5.4(b). Nevertheless, the composite still behaves like a linear dielectric and the polarization response in the ferroelectric particles is still very small ( $<0.01 \text{ C/m}^2$  at  $800 \text{ kV/cm}$ ). That is, the ferroelectric properties of the isolated particles do not transfer into the macroscopic properties of the composites.

### **5.1.3.3 Effect of Ferroelectric Phase Connectivity**

In order to effectively transfer the desired properties of the ferroelectric particles into the macroscopic properties of the composites, depolarization field effect must be further reduced. In order to do so, continuous ferroelectric phase distribution is required. To investigate the effect of phase connectivity without changing the ferroelectric phase

volume fraction, we relocate one small grain to fill the gap between the elongated particles, as highlighted in Figure 5.4(c, d). The simulated  $P$ - $E$  curve for such a composite microstructure shown in Figure 5.4(d) is also plotted in Figure 5.4. It is interesting that such a small change in the particulate microstructure brings about drastic change in the composite properties: the  $P$ - $E$  curve exhibits hysteresis loop characteristic of ferroelectric behavior, and the ferroelectric phase shows strong polarization response ( $\sim 0.4 \text{ C/m}^2$  at 800 kV/cm) comparable to monolithic ferroelectric polycrystal.

To reveal the origin of such a drastic change, Figure 5.5 compares the domain microstructures in the discontinuous and continuous ferroelectric phases of the two composites both under 800 kV/cm electric field applied along the phase alignment direction. It is clearly seen that the single relocated grain creates a bridge between the ferroelectric particles to provide a continuous polarization path in the ferroelectric phase, thus enabling local polarization to reorient along the external electric field direction without generating interfacial charge accumulation or depolarization field. It is worth noting that such small microstructural change of single relocated grain causes a qualitative change in the phase connectivity from 0-3 to 1-3. Therefore, in order to effectively transfer the ferroelectric properties of the particles into the macroscopic properties of the composites, continuous ferroelectric phase connectivity is required. Without such continuous phase connectivity, the composites would behave just like linear dielectric materials with very small dielectric constant, even though ferroelectric particles of large dielectric constant are used.

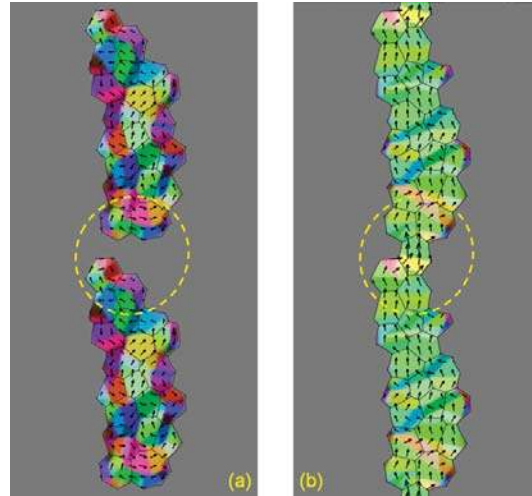


**Figure 5.5** Comparison of simulated polarization distributions in (a) discontinuous and (b) continuous ferroelectric phase.

#### 5.1.3.4 Effect of Electrical Conductivity of Polymer Matrix

Tuning the depolarization field is another approach to change the electric response of the 0-3 ferroelectric composite. An easy way to do that is to control the conductivity of the polymer matrix, for example, by filling polymer matrix with metal powders[176]. The nonzero conductivity of matrix phase serves to redistribute the free charge to reduce/eliminate the bound charges accumulated at the interfaces caused by polarization terminations, thus decreasing/removing the depolarization field to the ferroelectric phase. In order to exploit the possibility of tailoring the  $P$ - $E$  loops of ferroelectric composite, we studied the effects of different electric conductivities of polymer matrix. Our recently developed phase field modeling of current density distributions in complex microstructures is incorporated, which solves the microscopic Ohm's law in the same phase field formalism as for electric and elastic domain evolutions[153]. Here we employed the composite model

for small grain size (illustrated in Figure 5.6) and simulated 3 conductivities settings for polymer matrix.

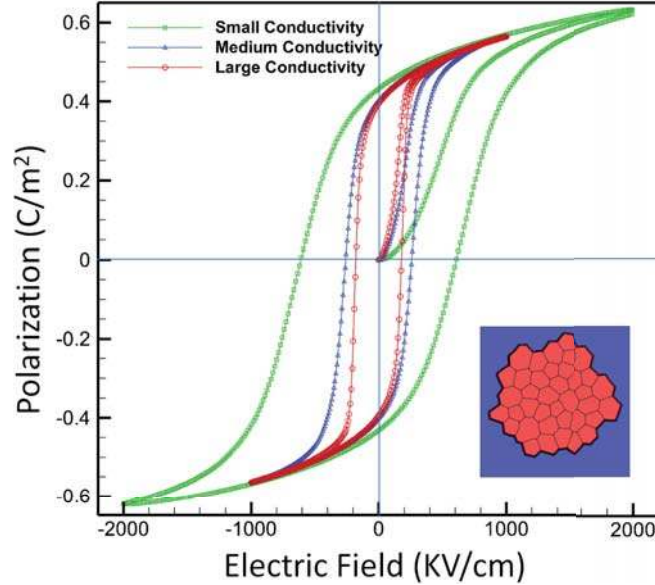


**Figure 5.6**  $P$ - $E$  loops for 0-3 ferroelectric ceramic/polymer composites with different conductivities for polymer matrix.

The obtained polarization-electric field hysteresis loops for three different conductivities are presented in Figure 5.6. It clearly demonstrates that the presence of different conductivities of polymer matrix affects the hysteresis loops, including the coercive electric field  $E_c$  and remanent polarization  $P_R$ . The increase in the conductivity of polymer benefits the ease of domain switching and domain wall motion, resulting to smaller  $E_c$  and  $P_R$ , and a more rectangular shape for  $P$ - $E$  loop. The simulation suggests that the  $P$ - $E$  loops of 0-3 ferroelectric composite can be effectively tailored by carefully controlling the conductivities of polymer matrix.

#### **5.1.4 Conclusion**

In summary, computer modeling and simulation of ferroelectric ceramic particle-filled polymer-matrix composites show that the macroscopic properties of the composites critically depend on the ferroelectric phase connectivity while are not sensitive to the sizes and internal grain structures of the ceramic particles. In order to fully exploit the ferroelectric properties of the particles embedded in the composite matrix, continuous ferroelectric phase connectivity is required. Without such continuous phase connectivity, the composites just behave like linear dielectric materials with very small dielectric constant, even though ferroelectric particles of large dielectric constant are used. Such composite behaviors are found to be dominated by depolarization field effect, which depends on the arrangement, alignment and, most importantly, connectivity of the ferroelectric particles.

## 5.2 Field-Induced Ferroelectric Phase Transition and Nonlinear Dielectric Behavior

### 5.2.1 Introduction

High energy density capacitors require dielectric materials of both large dielectric constant and high breakdown strength. [177] Dielectrics usually exhibit either large dielectric constant or high breakdown strength, but unfortunately not both simultaneously.[112] Nonlinear dielectric materials exhibit nonlinear dependence of polarization on electric field and could offer dielectric capacity higher than linear dielectrics. Figure 5.7 shows three typical dielectric behaviors to illustrate the desired nonlinear polarization versus electric field response for high energy density. The electric energy density stored in each dielectric material is  $U = \int_0^E EdP$ , as indicated by the shaded area in Figure 5.7. For the same maximum values of electric field and polarization, as compared to linear dielectric in Figure 5.7(a), the nonlinear dielectric in Figure 5.7(b) undergoes unwanted early polarization saturation at low electric field, which leads to low dielectric capacity. Multi-domain ferroelectrics with low coercivity field and easy domain switching typically exhibit such early polarization saturation.[178] In contrast, the nonlinear dielectric in Figure 5.7(c) exhibits small dielectric constant at low electric field and undergoes a polarization jump at higher electric field, which yields high dielectric capacity. Such desired nonlinear polarization jump is usually associated with electric field-induced phase transformation, such as antiferroelectric→ferroelectric transition.[179, 180]

Antiferroelectric phase has been exploited as nonlinear dielectric for high density energy storage applications.[181]

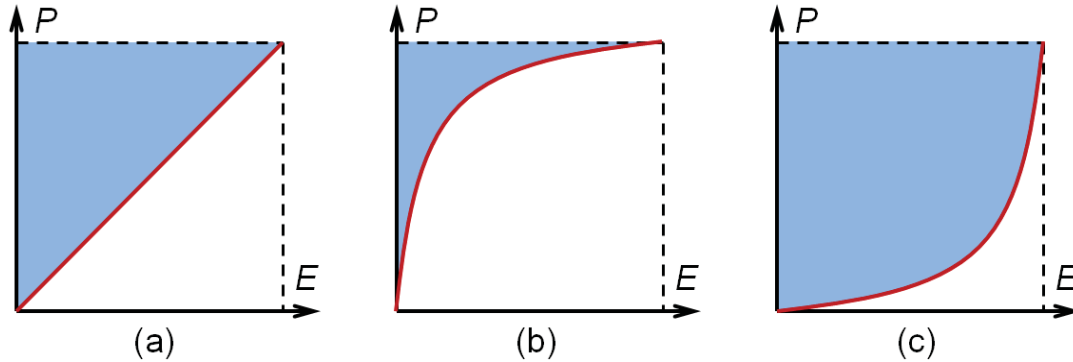


**Figure 5.7** Schematic illustration of (a) linear dielectric, (b) nonlinear dielectric with early polarization saturation, and (c) nonlinear dielectric with high dielectric capacity. Shaded area indicates electric energy density stored in each dielectric material.

In this chapter, we employ phase field modeling and computer simulation to study the nonlinear polarization behavior associated with electric field-induced transition between paraelectric and ferroelectric phases. Single crystals along different crystallographic axes and polycrystals with different degrees of grain textures are investigated for field-induced paraelectric→ferroelectric phase transition behavior to achieve increased dielectric capacities. The modeling and simulation solves the local charge density and internal electric field caused by heterogeneous polarization distribution, and takes into account the local field-dependent phase transition and nonlinear polarization behaviors.

## 5.2.2 Model and Materials Parameters

Phase field model of ferroelectric and paraelectric polycrystals is employed, as used in Section 5.1 but at temperature above Curie point. Here, we consider BaTiO<sub>3</sub> as a model system, whose thermodynamic property is characterized by the same Landau-Ginzburg-Devonshire free energy function as mentioned before, where the polynomial coefficients are:[182]  $\alpha_1=3.34\times 10^5(T-381) \text{ VmC}^{-1}$ ,  $\alpha_{11}=4.69\times 10^6(T-393)-2.02\times 10^8 \text{ Vm}^5\text{C}^{-3}$ ,  $\alpha_{12}=3.23\times 10^8 \text{ Vm}^5\text{C}^{-3}$ ,  $\alpha_{111}=-5.52\times 10^7(T-393)+2.76\times 10^9 \text{ Vm}^9\text{C}^{-5}$ ,  $\alpha_{112}=4.47\times 10^9 \text{ Vm}^9\text{C}^{-5}$ ,  $\alpha_{123}=4.91\times 10^9 \text{ Vm}^9\text{C}^{-5}$ . The electrostrictive constants are:  $Q_{11}=0.11 \text{ m}^4\text{C}^{-2}$ ,  $Q_{12}=-0.045 \text{ m}^4\text{C}^{-2}$ ,  $Q_{44}=0.029 \text{ m}^4\text{C}^{-2}$ .

## 5.2.3 Landau Theory-based Analysis of Single Crystal

To illustrate the intrinsic dielectric behavior of BaTiO<sub>3</sub> single crystal, Figure 5.8(a) plots the Landau-Ginzburg-Devonshire free energy  $f(\mathbf{P})$  as a function of polarization  $\mathbf{P}=(P,0,0)$  at different temperatures. According to the geometrical features (stationary/inflection points) of the free energy profiles, four characteristic temperatures are defined as shown in Figure 5.8(b):  $T_0$  is the Curie-Weiss temperature below which paraelectric phase is instable;  $T_C$  is the Curie temperature at which paraelectric and ferroelectric phases have equal free energy;  $T_1$  is the temperature above which ferroelectric phase is instable; and  $T_2$  is the temperature above which a paraelectric→ferroelectric phase transition can no longer be induced by electric field.



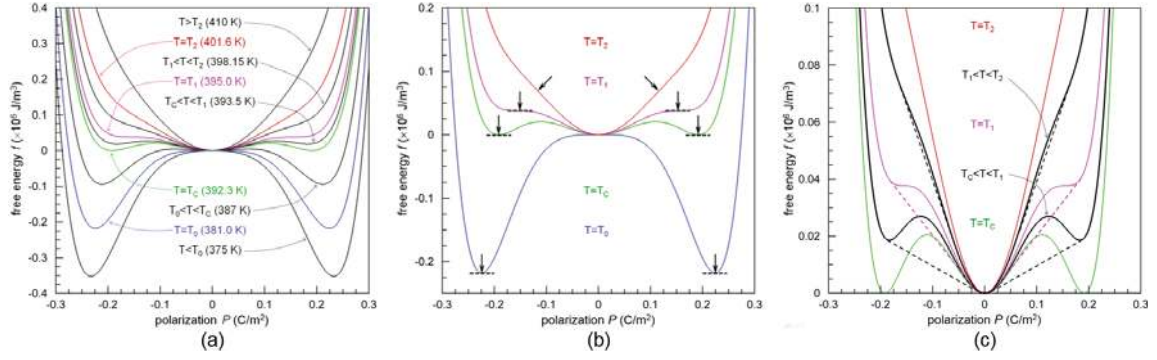


**Figure 5.8** Landau-Ginzburg-Devonshire free energy  $f(\mathbf{P})$  as a function of polarization  $\mathbf{P}=(P,0,0)$ : (a) temperature dependence; (b) characteristic temperature and corresponding polarization magnitude  $T_0$  ( $P_s=0.226$  C/m<sup>2</sup>),  $T_C$  ( $P_s=0.191$  C/m<sup>2</sup>),  $T_1$  ( $P_s=0.156$  C/m<sup>2</sup>) and  $T_2$  ( $P_s=0.119$  C/m<sup>2</sup>) defined according to stationary and/or inflection points as highlighted by dashed line segments and/or arrows; (c) convexification of nonconvex free energy profile between temperature  $T_C$  and  $T_2$  by common tangent as highlighted by dashed line segments.

The four characteristic temperatures define five temperature ranges of different polarization-electric field ( $P$ - $E$ ) responses under  $\mathbf{E}=(E,0,0)$  as shown in Figure 5.9: ( $T < T_0$ ) Ferroelectric phase is stable, paraelectric phase is instable, and  $P$ - $E$  response shows large hysteresis loop as determined by domain switching; ( $T_0 < T < T_C$ ) Ferroelectric phase is stable, paraelectric phase is metastable, and  $P$ - $E$  response shows intermediate hysteresis loop as determined by domain switching; ( $T_C < T < T_1$ ) Paraelectric phase is stable, ferroelectric phase is metastable, and  $P$ - $E$  response shows small hysteresis loop with kinks associated with the electric field-induced paraelectric $\leftrightarrow$ ferroelectric phase transition; ( $T_1 < T < T_2$ ) Paraelectric phase is stable, ferroelectric phase is instable but can be induced by electric field, and  $P$ - $E$  response shows very small hysteresis associated with the electric field-induced paraelectric $\leftrightarrow$ ferroelectric phase transition; ( $T > T_2$ ) Paraelectric phase is stable,

ferroelectric phase is unstable and cannot be induced by electric field, and  $P$ - $E$  response is free of hysteresis. As shown in Figure 5.9(b), as long as  $T < T_1$ , the  $P$ - $E$  response is always irreversible, that is, polarization does not return to zero upon removal of electric field. Such dielectric irreversibility prevents energy storage application because the energy cannot be released. On the other hand, as shown in Figure 5.9(a), at  $T > T_1$ , polarization spontaneously return to zero upon removal of electric field, thus capable of releasing the stored energy.

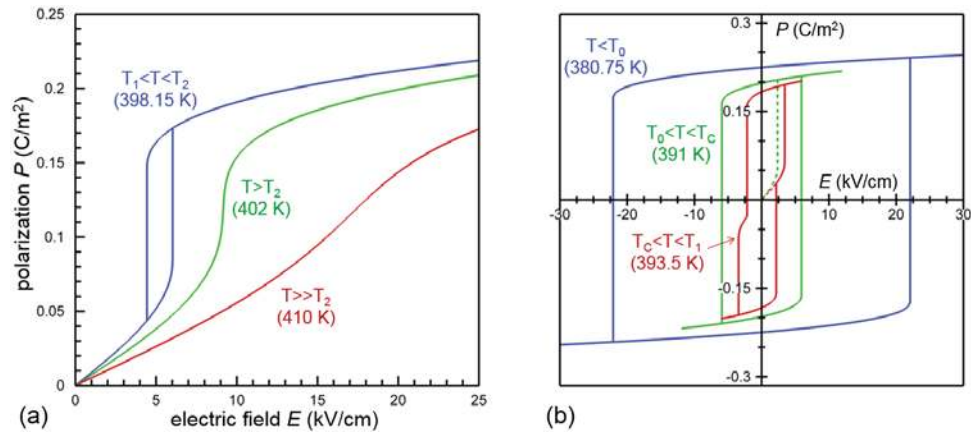


**Figure 5.9** Polarization-electric field ( $P$ - $E$ ) response at different temperatures as determined from Landau-Ginzburg-Devonshire free energy  $f(\mathbf{P})$  under  $\mathbf{E}=(E,0,0)$ .

High dielectric capacity desires a nonlinear  $P$ - $E$  response that undergoes a polarization jump, as illustrated in Figure 5.7(c). Such a behavior is obtained at temperature between  $T_1$  and  $T_2$ , where the polarization jump is associated with the electric field-induced paraelectric  $\rightarrow$  ferroelectric phase transition. In this work, we consider temperature in this range. It is worth noting that at  $T > T_2$ , the  $P$ - $E$  nonlinearity diminishes with increasing temperature, and higher dielectric breakdown strength is required to achieve high energy capacity, which imposes additional challenge to technological application.

## 5.2.4 Simulation Results and Discussion

### 5.2.4.1 Polycrystals and Texture Effect

Dielectric  $P$ - $E$  responses at temperature 398.15 K (between  $T_1$  and  $T_2$ ) along different axes of BaTiO<sub>3</sub> single crystal is shown in Figure 5.10(a). It is found that paraelectric→ferroelectric phase transition can be induced along [100] but not [110] or [111] axis. This is because tetragonal ferroelectric phase has lower free energy than orthorhombic and rhombohedral ferroelectric phases at this temperature. For comparison, the  $P$ - $E$  response of an untextured polycrystal with random grain orientations is also shown in Figure 5.10(a), which is close to the  $P$ - $E$  response of [110]-oriented single crystal and does not exhibit electric field-induced paraelectric→ferroelectric phase transition. This observation suggests that in order to exploit the nonlinear dielectric behavior in a polycrystal, [100] texture is required. It is worth noting that in [100]-oriented single crystal, the electric field-induced paraelectric↔ferroelectric phase transition is accompanied by hysteresis as detailed in Figure 5.10(b), which is similar to that observed in antiferroelectric materials.[\[180\]](#) The field-induced phase transition and accompanied hysteresis originate from the nonconvex free energy profile (characterized by existence of inflection points) as shown in Figure 5.8(c). Under equilibrium condition, it is the convexified free energy profile (as indicated by dashed common tangent line) that determines the  $P$ - $E$  response, which exhibits anhysteretic jump as shown by dashed line in Figure 5.10(b). However, with finite charging/discharging rate, an equilibrium phase transition is not achieved, and paraelectric↔ferroelectric phase transition occurs with “over/under-voltage” leading to hysteresis. The hysteresis shown in Figure 5.10 represents the maximum hysteresis where

one phase completely loses metastability under electric field. In reality, the  $P$ - $E$  curve exhibits smaller hysteresis due to thermal nucleation of electric field-dependent stable phase.

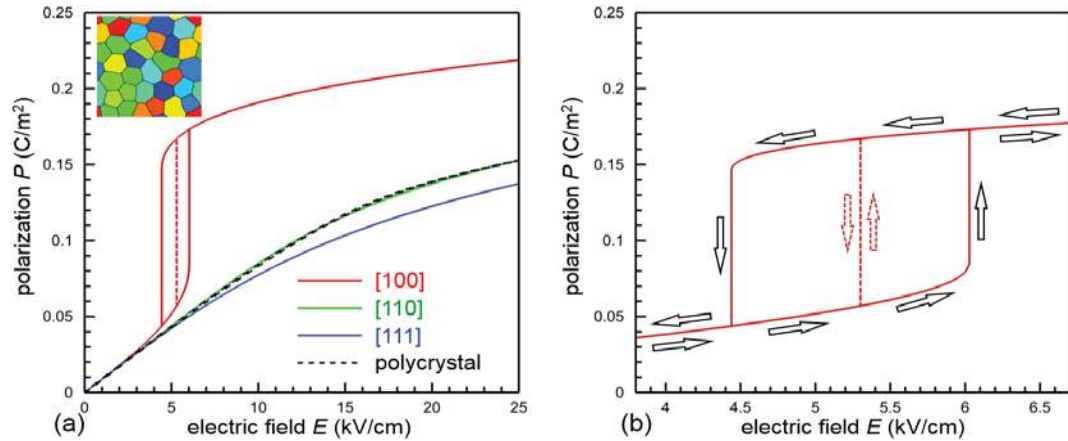


**Figure 5.10** (a) Polarization-electric field ( $P$ - $E$ ) response at temperature 398.15 K between  $T_1$  and  $T_2$  along different axes of a single crystal. For comparison,  $P$ - $E$  response of an untextured polycrystal with random grain orientations (shown as inset) is also plotted. (b)  $P$ - $E$  hysteresis associated with [100] electric field-induced transition between paraelectric and ferroelectric phases. The anhyseretic jump (dashed line) corresponds to equilibrium condition.

To study the effect of [100] texture on polarization behavior polycrystals, phase field modeling and simulation is employed, which solves the local charge density and internal electric field caused by heterogeneous polarization distribution in a polycrystal, and takes into account the local field-dependent phase transition and nonlinear polarization behavior. A polycrystal containing 32 grains shown in inset of Figure 5.10(a) is used in the simulation. Different degrees of [100] grain texture are considered, ranging from untextured random grain orientations to perfectly oriented grains (variation in [100] axis

orientation is  $0^\circ$ ), which is implemented by the grain rotation matrix field  $\mathbf{R}(\mathbf{r})$ . The  $P$ - $E$  responses and dielectric capacities of the polycrystals with different textures are compared in Figure 5.11.

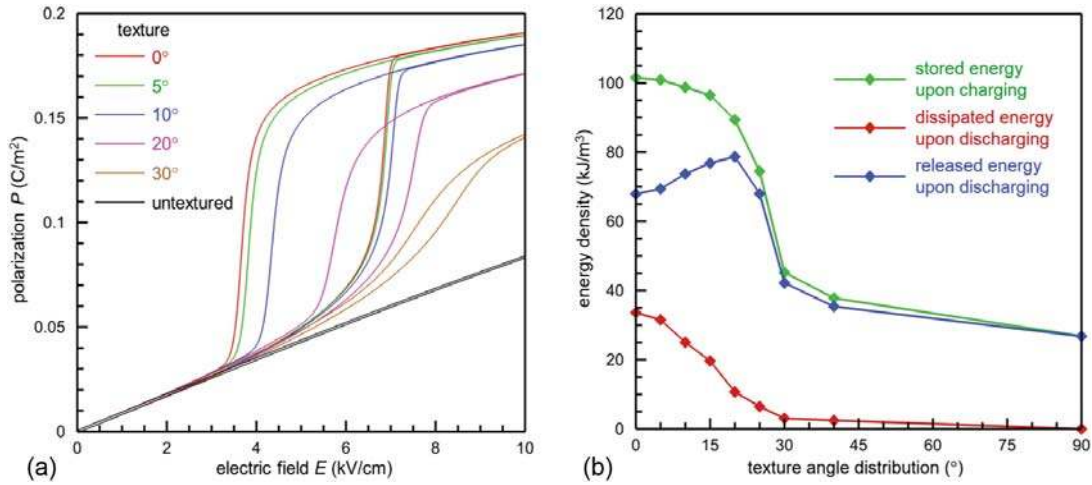


**Figure 5.11** (a) Polarization-electric field ( $P$ - $E$ ) response at temperature 398.15 K between  $T_1$  and  $T_2$  in polycrystals of different degrees of [100] uniaxial texture. (b) Energy density stored upon charging to 8 kV/cm, energy density released upon discharging, and energy density dissipated per charge-discharge cycle.

It is found that polycrystals with high degree of [100] texture are able to undergo field-induced phase transition and exhibit nonlinear polarization response with significantly increased dielectric capacity. According to Figure 5.11(b), a critical degree ( $\sim 20^\circ$ ) of [100] uniaxial texturing is required for high dielectric capacity; that is, the variation in [100] axis orientation of the grains should be confined within a cone of  $20^\circ$  half apex angle. Beyond this uniaxial texturing limit, the dielectric capacity of polycrystals rapidly drops. The hysteresis accompanying the field-induced phase transition also leads to energy density lost upon discharging, as shown in Figure 5.11(b). It is the released

energy density upon discharging that specifies the useful energy density, which reaches maximum at  $\sim 20^\circ$  texturing and remains high at higher degree of texturing due to electric field-induced paraelectric $\leftrightarrow$ ferroelectric phase transition while drops rapidly with decreasing texturing beyond  $20^\circ$ , as shown in Figure 5.11(b).

#### 5.2.4.2 Composites and Microstructure Effect

From Chapter 5.1 we learnt that the macroscopic properties of 0-3 ferroelectric-polymer composites depend on the ferroelectric phase connectivity while are not sensitive to the sizes and internal grain structures of the ceramic particles. The composites with isolated particles (0-3 connectivity) lose the hysteresis feature and always exhibit linear dielectric response, irrespective of particle shapes/sizes/alignments. The strong depolarization field generated within the isolated particle was found to be responsible for this observation. This inspired us to study the effect of depolarization field in 0-3 paraelectric-polymer composite: are we able to observe the nonlinear polarization jump as we saw in the [100]-textured paraelectric polycrystal?

Figure 5.12(b) presents the polarization-electric field response for a polymer composite with isolated paraelectric particles, which is also shown in Figure 5.12(a). It's clearly demonstrated that 0-3 paraelectric-polymer composites exhibit linear  $P$ - $E$  response without any polarization jump. It's worth mentioning that the paraelectric particle used in the composite showing in Figure 5.12(a) is ideally ( $0^\circ$ ) [100]-textured. Although the nonlinear polarization jump could be expected in textured polycrystals, the nonlinear behavior is compromised when the polycrystals are embedded in polymer matrix. The

reason is that – similar with the case of ferroelectric-polymer composite – upon the application of electric field, the induced local polarization vectors in paraelectric particle will generate interfacial charges thus increases the depolarization field and electrostatic energy. As a result, the local polarization response to external electric field is too weak to trigger the paraelectric→ferroelectric phase transition. The composites behave like linear dielectric materials with very small dielectric constant, even though textured paraelectric particles are used.

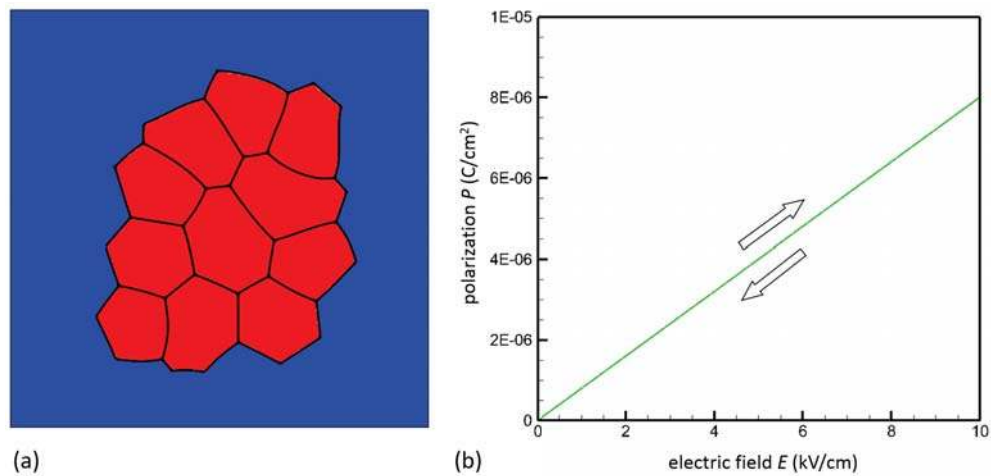


**Figure 5.12** (a) Phase morphology of 0-3 paraelectric composite; (b) Simulated  $P$ - $E$  response for 0-3 paraelectric composite.

In order to fully exploit the paraelectric↔ferroelectric phase transition in a polymer matrix composite, continuous paraelectric phase connectivity is required to reduce the strong depolarization field effect. We came up with this inference based on the discussion for ferroelectric-polymer composite in Chapter 5.1.3. Thus, the pathway to fabricate a

paraelectric-polymer composite exhibiting paraelectric $\leftrightarrow$ ferroelectric phase transition is clear: to make the [100]-textured paraelectric phase continuous in polymer matrix.

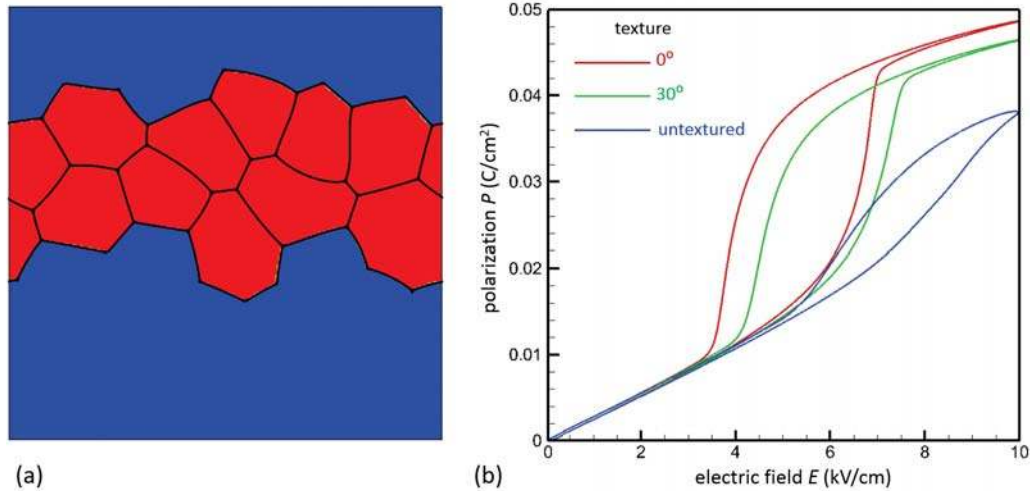


**Figure 5.13** (a) Phase morphology of a 1-3 paraelectric composite; (b) Simulated  $P$ - $E$  response in the 1-3 paraelectric composite of different degrees of [100] uniaxial texture.

To validate the inference, we created a 1-3 paraelectric polymer matrix composite as shown in Figure 5.13(a), and compared its  $P$ - $E$  responses with different textures in Figure 5.13(b). It is found that composites with high degree of [100] texture (*e.g.*,  $0^\circ$ ) are able to undergo field-induced phase transition and exhibit nonlinear polarization response with significantly increased dielectric capacity. This is because the 1-3 connectivity of paraelectric phase provides a continuous polarization path in the ferroelectric phase, thus enabling local polarization to fully evolve along the external electric field direction without generating interfacial charge accumulation, as illustrated in Figure 5.14. It's also found from Figure 5.13(b) that, the nonlinear polarization response of the composite becomes weaker with less [100] texturing, and almost disappears in untextured composite. This



texture effect in paraelectric composite observed in Figure 5.13(b), is consistent with that in polycrystal, which was previously presented in Figure 5.11(a).

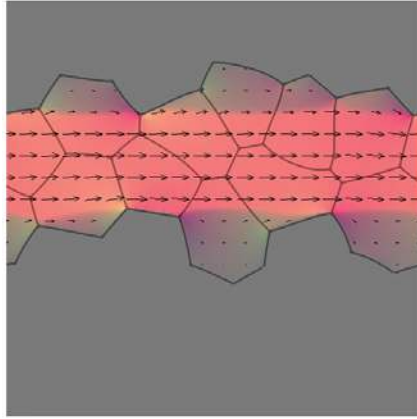


**Figure 5.14** Simulated polarization distributions in  $0^\circ$  [100]-textured 1-3 continuous composites.

### 5.2.5 Conclusion

In summary, theoretical analysis reveals that paraelectric→ferroelectric phase transition can be induced by electric field along [100] but not [110] or [111] axis of a BaTiO<sub>3</sub> single crystal, and computer simulation further shows that [100]-textured polycrystalline BaTiO<sub>3</sub> is able to undergo field-induced phase transition and exhibit nonlinear polarization behavior. A critical degree ( $\sim 20^\circ$ ) of [100] uniaxial texturing is determined by simulations that is required in order to achieve significantly increased dielectric capacity desired for high energy density storage application. In order to fully exploit the paraelectric↔ferroelectric phase transition and nonlinear polarization behavior

in a polymer matrix composite, continuous paraelectric phase connectivity and [100] uniaxial texturing are required.

# Chapter 6. Diffuse Interface Field Approach to Modeling and Simulation of Particles Packing

## 6.1 Introduction

Ferroic particulate-polymer composites are a promising group of materials that provide demanding packages that combine the ferroic materials' functional properties and the polymer's mechanical flexibility and processing flexibility. The performance of the filler-polymer composites depends on the properties of constituent phases, and the way in which the phases are connected. Composites with different connectivities have been manufactured, including 0-3 particulate, 1-3 chain-like composites, 2-2 laminated, *etc.*

Particle packing and motion in liquid phase plays in a significant role in the fabrication of particulate-polymer composites. For example, composites of 0-3 connectivity can be fabricated through very inexpensive method including simple mixing and molding: the functional filler particles or powders are packed into the solution to form liquid formulations of various filler concentration, and the formulations were then cured to become a ferroic polymer composite. [[183](#), [184](#)] In this process, the particle packing determines the degree of dispersion, agglomeration and percolation, as well as the highest volume fraction of fillers in composites. Recently, external electric/magnetic field controlled self-assembling processing has been widely employed as a route to fabricate various 1-3 chain-like composites, including dielectric, electrostrictive, magnetostrictive

and magnetoelectric. A nonuniform electric/magnetic field is applied to a suspension of ferroic particles (polarized or magnetized). Due to the dipole interaction among particles and their interaction with external field, the random dispersed particle will move, rearrange, and gradually align themselves into chains along external fields [177, 183, 185]. The particle motion has a crucial effect on the self-assembled particulate microstructures and the resultant composite properties. It would be beneficial if we can gain more understanding and controlling of the particle packing phenomena which influences the fabrication processes of 0-3 and 1-3 chain-like polymeric composites.

## 6.2 Current Status and Challenge

Over the recent decades, much progress has been made in the simulation study of packing and two complementary conceptual approaches, *i.e.*, the *dynamic models* and the *packing algorithms*, have emerged to generate random packing of particles. Being more concerned with the quantitative characterization of final packing structure or maximum packing density, the packing algorithms [186-188] usually neglect the physical packing process to achieve a high computational efficiency. On the other hand, the dynamic models, also known as sequential procedures, are designed to capture the physical packing process and generate the packing configuration.

Based on the sequential technique, plenty of analytical models [189, 190] and simulation models have already been developed employing various methods such as Monte Carlo [191, 192], distinct element method [193, 194] and molecular dynamics [195, 196]. Most of the simulation attempts assume a spherical shape for the packing particles.

However, the filler particles usually have non-uniform sizes and irregular shapes. It is important to study the effects of particle shape and size distribution on the particle packing and mixing process in melt polymer, and how the particle packing impacts the properties of resultant 0-3 composites. In the perspective of numerical simulation, allowing the nonspherical shapes will cause considerable complexity in representing and tracking the geometries of asymmetric particles and unpredictable contacts between particles. To date, dynamic packing process of arbitrarily shaped particles hasn't been truly considered.

Friction exists in real materials processing, and usually makes the system's behavior profoundly differ from the one with ideal assumption. For instance in the self-assembling process of particulates in polymer composites, the particle/particle friction, along with the particle shape irregularity, will affect the paths of particles and the resultant alignment. In this way, a good dynamic packing model is required to account for the friction in order to display the physical packing process. However, due to the high nonlinearity of friction at zero velocity, handling the friction force is a cumbersome task in numerical simulation. When the relative velocity is zero (sticking), the static friction between two surfaces is what it must be to maintain zero velocity [197], so it may take any value from zero up to the maximum static friction. Existing models of particle packing either neglected the friction by dealing with ideal hard particles [188, 193, 198, 199], or dealt with sphere shape [194-196] to obtain an acceptable computing efficiency.

## 6.3 Diffuse Interface Field Approach to Particle Packing Problem

The purpose of this chapter is to develop an effective model of dynamic random packing of arbitrarily shaped particles based on the diffuse interface field approach (DIFA) method. The DIFA method is similar to, although more general than, the commonly known phase-field method [146] in that they both describe the evolution of arbitrary microstructures without explicitly tracking the interface positions (in contrast to this feature, the conventional sharp interface-based approach to microstructure evolutions tracks the locations of a priori unknown interfaces, making its numerical implementation difficult for complex microstructure evolutions). The DIFA model of particle packing in this chapter makes full use of this advantageous feature, *i.e.*, automatic field description of arbitrarily shaped particles, to gain insight into the effect of shape on the dynamic process of particles.

Another novelty for the proposed model is the consideration of friction between particles. Similar to the concept of some *continuous models* for friction [197, 200], in the DIFA model proposed here we attempted to predict the response of packing systems without identifying the transition between stick and slip or calculating the exact value of static friction. Instead, the frictional characteristics in the packing process were reproduced by modifying the equations of motion based on our previous research [201]. Due to the “*by-pass*” technique for the static friction, the current DIFA model is numerically efficient.

### 6.3.1 Inter-Particle Contact Force

A set of continuum field functions,  $\eta(\mathbf{r}, t; \alpha = 1, 2, \dots, p)$ , will be used to describe the “dropping and rolling” particles of arbitrary shapes and sizes [202], where  $p$  represents the number of total particles. The field variable  $\eta(\mathbf{r}, t; \alpha)$ , which records the shape, size, location and orientation of the  $\alpha$ th particle at time  $t$ , is prescribed to be 1 inside the particle and 0 outside with smooth but rapid transition across the particle surface, *i.e.*, the surface of particles is diffuse instead of sharp. This technique brings about two appealing features that can’t be obtained with sharp interface field [202]: (i) the geometry of the particles can be described by a diffuse interface field with a resolution higher than the discrete computational grid, which is required for a dynamic treatment of particle rigid-body translation and rotation; (ii) the short-range inter-particle force is automatically treated in terms of the field gradient  $\nabla \eta(\mathbf{r}, t; \alpha)$  by virtue of the diffuse interface, which offers a convenient treatment of arbitrarily-shaped particles.

As a dynamic simulation, our model approaches the random packing problem by reproducing the physical process of packing: particles will drop into a container and position themselves under the influence of a unidirectional gravity field  $\mathbf{g}=(0, g)$ . It’s worth mentioning that, the container is dealt with as a special particle in the simulation; its shape and position will also be described by a field function  $\eta(\mathbf{r}; \alpha)$  but it won’t be updated to let the container keep its position. At time  $t$ , the short-range inter-particle repulsive force is formulated through an effective local force density acting on the surface of the  $\alpha$ th particle by its neighbors [202]:

$$d\mathbf{F}^{\text{sr}}(\mathbf{r}, t; \alpha) = \kappa \sum_{\alpha' \neq \alpha} \eta(\mathbf{r}, t; \alpha) \eta(\mathbf{r}, t; \alpha') [\nabla \eta(\mathbf{r}, t; \alpha) - \nabla \eta(\mathbf{r}, t; \alpha')] d^3 r \quad (6.1)$$

where the constant  $\kappa$  characterizes the short-range interaction strength. The description of the short-range interaction force through the property of diffuse interface fields,  $\eta(\mathbf{r}, t; \alpha)$ , has the advantage that it automatically takes into account the arbitrary shapes and sizes of individual particles without explicitly tracking the particle surfaces. The resultant force and torque of short-range interaction acting on the  $\alpha$ th particle about its center of mass are:

$$\mathbf{F}^{\text{sr}}(t; \alpha) = \int_V d\mathbf{F}^{\text{sr}}(\mathbf{r}, t; \alpha) \quad (6.2)$$

$$\mathbf{T}^{\text{sr}}(t; \alpha) = \int_V [\mathbf{r} - \mathbf{r}^c(t, \alpha)] \times d\mathbf{F}^{\text{sr}}(\mathbf{r}, t; \alpha) \quad (6.3)$$

where  $\mathbf{r}^c(t; \alpha)$  is the position of the center of mass of  $\alpha$ th particle at time  $t$ . Note that the gradient factor,  $\nabla \eta(\alpha) - \nabla \eta(\alpha')$ , in the local force density  $d\mathbf{F}^{\text{sr}}(\alpha)$  ensures an action-reaction law of the short-range force between any pair of neighboring particles. And as the  $\nabla \eta(\alpha)$  is always along the normal direction of particle surface, we assumed that the  $\mathbf{F}^{\text{sr}}(t, \alpha)$  is a normal force repulsing the two particles away; this is also to say, the normal direction of the contact between two particles can be obtained by  $\mathbf{n}(t; \alpha, \alpha') = \mathbf{F}^{\text{sr}}(t, \alpha) / F^{\text{sr}}(t, \alpha)$ .



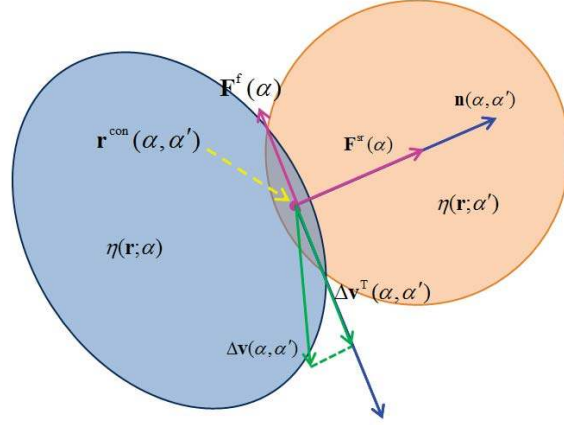


**Figure 6.1** Illustration for friction calculation.

### 6.3.2 Friction

We proceeded by dealing with the friction force. As shown in Eq. (1), the short-range repulsive force is treated in the manner of soft-sphere potential; therefore there is a slight overlap occurring between contacting particles as shown in Figure 6.1. However, to obtain a high computing efficiency, here we exerted the friction force on an *effective* contact point, instead of the above mentioned overlapping zone. This treatment is reasonable because, after all, most of the particles are interacting with their neighbors by point contacts. The position of the effective point of contact  $\mathbf{r}^{\text{con}}$  is calculated via

$$\mathbf{r}^{\text{con}}(t; \alpha, \alpha') = \frac{\int_V \eta(\mathbf{r}, t; \alpha) \eta(\mathbf{r}, t; \alpha') \mathbf{r} d^3 r}{\int_V \eta(\mathbf{r}, t; \alpha) \eta(\mathbf{r}, t; \alpha') d^3 r}, \quad (6.4)$$

where the notation “con” is short for “contact”. Now the linear velocity of the effective contact point  $\mathbf{v}^{\text{con}}(t)$  can be given based on the state of movement of the  $\alpha$ th particle:

$$\mathbf{v}^{\text{con}}(t; \alpha) = \mathbf{v}(t; \alpha) + \boldsymbol{\Omega}(t; \alpha) \times [\mathbf{r}^{\text{con}}(t; \alpha, \alpha') - \mathbf{r}^c(t; \alpha)]. \quad (6.5)$$

As the contact point belongs to both the contacting particles, most likely one can get a velocity difference when doing the above calculation based on different particle, *i.e.*,

$$\Delta \mathbf{v}(t; \alpha, \alpha') = \mathbf{v}^{\text{con}}(t; \alpha) - \mathbf{v}^{\text{con}}(t; \alpha'). \quad (6.6)$$

Actually,  $\Delta \mathbf{v}(t; \alpha, \alpha')$  represents the relative sliding velocity of the  $\alpha$ th and  $\alpha'$ th particle at contact point. As we know, the force of friction is always exerted in a direction that opposes the relative sliding, therefore, the direction of friction should be opposite to the projection of the  $\Delta \mathbf{v}(t; \alpha, \alpha')$  on the tangential direction of contact, *i.e.*,  $\Delta \mathbf{v}^T(t; \alpha, \alpha')$ ; see Figure 6.1. Finally, the friction force and its resultant torque exerted on the  $\alpha$ th particle, are

$$\mathbf{F}^f(t; \alpha) = \mu \mathbf{F}^{\text{sr}}(t; \alpha) \cdot \frac{-\Delta \mathbf{v}^T(t; \alpha, \alpha')}{\Delta \mathbf{v}^T(t; \alpha, \alpha')} \quad (6.7)$$

$$\mathbf{T}^f(t; \alpha) = [\mathbf{r}^{\text{con}}(t; \alpha, \alpha') - \mathbf{r}^c(t; \alpha)] \times \mathbf{F}^f(t; \alpha), \quad (6.8)$$

where  $\mu$  is the coefficient of friction and  $\Delta \mathbf{v}^T(t; \alpha, \alpha')$  can be obtained by

$$\Delta \mathbf{v}^T(t; \alpha, \alpha') = \Delta \mathbf{v}(t; \alpha, \alpha') - [\Delta \mathbf{v}(t; \alpha, \alpha') \cdot \mathbf{n}(t; \alpha, \alpha')] \mathbf{n}(t; \alpha, \alpha'). \quad (6.9)$$

Now the total force and torque acting on the  $\alpha$ th particle will be:

$$\mathbf{F}(t; \alpha) = \mathbf{F}^{\text{sr}}(t; \alpha) + \mathbf{F}^f(t; \alpha) + m(\alpha) \cdot \mathbf{g} \quad (6.10)$$

$$\mathbf{T}(t; \alpha) = \mathbf{T}^{\text{sf}}(t; \alpha) + \mathbf{T}^{\text{f}}(t; \alpha) \quad (6.11)$$

where  $m(\alpha)$  is the mass of the  $\alpha$ th particle. The force  $\mathbf{F}(\alpha)$  and torque  $\mathbf{T}(\alpha)$  drive the falling and rearranging process of the particles.

### 6.3.3 Equations of Motion

Our purpose of this model is to simulate the motion of filler particles in liquid viscous un-cured polymer, where the inertia term is negligible and the Reynolds number is small, *i.e.*,  $\text{Re} \ll 1$ . The *Navier-Stokes* equations became considerably simpler with the small Reynolds numbers [203], also see Eq. (10) & (11) in *ref.* [202]. However, in the presented DIFA model, we modified the simplified Navier-Stokes equations by introducing a *damping term* and, accordingly, changing the algorithm by which the linear and angular velocity are obtained. The improved equations of motion are:

$$F_i(t; \alpha) = M_{ij}(\alpha)V_j(t; \alpha) + M'_{ij}(\alpha)\Delta V_j(t; \alpha) \quad (6.12)$$

$$T_i(t; \alpha) = N_{ij}(\alpha)\Omega_j(t; \alpha) + N'_{ij}(\alpha)\Delta\Omega_j(t; \alpha) \quad (6.13)$$

$$\mathbf{V}(t + \Delta t; \alpha) = \mathbf{V}(t; \alpha) + \Delta\mathbf{V}(t; \alpha) \quad (6.14)$$

$$\mathbf{\Omega}(t + \Delta t; \alpha) = \mathbf{\Omega}(t; \alpha) + \Delta\mathbf{\Omega}(t; \alpha) \quad (6.15)$$

where the summation convention over a repeated index is implied,  $M_{ij}$  and  $N_{ij}$  are tensors coefficients characterizing the particle translation and rotation mobilities, respectively, which are independent of velocity and determined by the fluid mechanics of

moving/rotating particle in a viscous liquid [203]. For example, in the case of spherical particles of radius  $a$ ,  $M_{ij} = 6\pi\sigma a\delta_{ij}$  and  $N_{ij} = 8\pi\sigma a^3\delta_{ij}$ , where  $\sigma$  is the viscosity of the carrier fluid.  $M'_{ij}$  and  $N'_{ij}$  are the damping coefficients we introduced here which actually establish a relation between the velocity change and the total force/torque change in the packing process. The damping term is similar to inertia in the sense that both of them serve to prevent the velocities from changing too rapidly. This technique ensures that the velocities smoothly evolve with time, even with rapid changing forces and/or torques, thus achieving a good numerical stability in a dynamic simulation. As will be discussed later, the damper offers a self-adjusting feature to the dynamic DIFA model, allowing us to reproduce a frictional packing process without calculating the value of static friction.

The particle rigid-body translation and rotation are described in terms of the evolutions of the field  $\eta(\mathbf{r}, t; \alpha)$ :

$$\eta(\mathbf{r}, t; \alpha) = \eta(\mathbf{r}^0, t_0; \alpha) \quad (6.16)$$

where the instant (at  $t$ ) and original (at  $t_0$ ) position vectors  $\mathbf{r}$  and  $\mathbf{r}^0$  are related by the following transformation:

$$r_i = Q_{ij}(t; \alpha)[r_j^0 - r_j^c(t_0; \alpha)] + r_i^c(t; \alpha) \quad (6.17)$$

where the position of the center of mass of the particle and the matrix of rigid-body rotation evolve according to the following increment forms of equations of motion:

$$r_i^c(t + dt; \alpha) = r_i^c(t; \alpha) + V_i(t; \alpha)dt \quad (6.18)$$

$$Q_{ij}(t + dt; \alpha) = R_{ik}(t; \alpha)Q_{kj}(t; \alpha) \quad (6.19)$$

where

$$R_{ij}(t; \alpha) = \delta_{ij} \cos \omega + l_i l_j (1 - \cos \omega) - \varepsilon_{ijk} m_k \sin \omega, \quad (6.20)$$

and  $\omega(t; \alpha) = \mathbf{\Omega}(t; \alpha)dt$  is the rotation angle,  $\mathbf{l} = \boldsymbol{\omega} / \omega$  is the direction of rotation axis and  $\varepsilon_{ijk}$  the permutation symbol. The vector tensors  $M_{ij}$  and  $N_{ij}$  rotates with the particles:

$$M_{ij}(t; \alpha) = Q_{ik}(t; \alpha)Q_{jl}(t; \alpha)M_{kl}(t_0; \alpha) \quad (6.21)$$

$$N_{ij}(t; \alpha) = Q_{ik}(t; \alpha)Q_{jl}(t; \alpha)N_{kl}(t_0; \alpha) \quad (6.22)$$

The spatial and temporal evolutions of the fields  $\eta(\mathbf{r}, t; \alpha)$  are determined by the above forces and equations of motions. They describe the microstructural evolution of particles during a dynamic packing process. The primary driving force is the gravitation of each particle, and the short range repulsive forces and the friction forces serve to affect neighboring particle arrangements and prevent particle interpenetration.

## 6.4 Simulation Results

### 6.4.1 Simulation Test of Simple Cases

Before implementing the complete DIFA model for numerical simulation, we carried out several simple cases to check the validity and reliability of the modified equations of motion. All the simulations in this part are carried out using *Microsoft Office Excel*.

#### **6.4.1.1 Simplest Case: Free Fall of Ball in Fluid**

Consider a ball with a mass of  $m$  released above the ground at time  $t_0$ , it will accelerate from  $V(t_0) = 0$  due to the vertical gravity  $g$ , and eventually attains a steady speed (*terminal speed*). In this case, we inspected the velocity evolution without consideration of friction, thus the total driving force  $F(t) = mg$ , and the Eq. (12) is reduced to be

$$mg = MV(t) + M'\Delta V(t) \quad (6.23)$$

Combing Eq. (6.14) we obtained the solution from the formulation of current DIFA model.

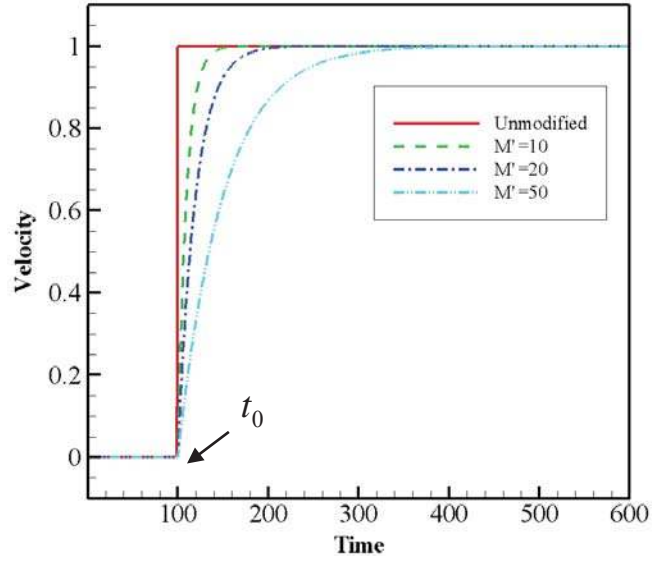


**Figure 6.2** Velocity evolution of free falling ball in viscous fluid. The red solid line are the result obtained by unmodified equations of motion, while the solutions by modified equations are plotted using different line types, corresponding to different values of  $M'$ . In all solving processes,  $m = 1$ ,  $g = 1$  and  $\Delta t = 0.1$ .

The solutions for  $V$  are plotted in Figure 6.2, as well as the solution obtained from the unmodified formulation in [202]. It shows that in the absence of friction the damping term will not change the final state of movement for the dropping ball in the system. With whatever value for  $M'$ , a same terminal speed, say,  $mg / M$ , was obtained eventually. But as the term “damping” indicates, the factor  $M'$  serves to slow down the speeding of the ball; the larger the  $M'$  is, the stronger the damping effect is. This effect is very similar to the inertia effect which is related the mass of an object. In this perspective, we may also consider the  $M'$  as an *effective mass* of the ball. Due to the presence of  $M'$ , the velocity

increases smoothly from 0 to the terminal speed, thus avoiding the velocity discontinuity and offering a great benefit for the numerical stability.

#### 6.4.1.2 Conveyor Problem

We then dealt with an interesting scenario of dropping an object (with initial velocity  $V_1$ ) on a horizontal conveyor belt moving at a constant velocity  $V_0$ , as sketched in Figure 6.3. The velocity of the object will change due to the friction force with the belt surface. If the rolling of the object is neglected, what is the ultimate speed it attains? In current case, the friction force is the only driving force which will change the state of motion of the object. The Eq. (6.12) goes to

$$F^f = MV(t) + M'\Delta V(t) \quad (6.24)$$

and Eq. (6.7) is simplified as

$$F^f = \begin{cases} \mu mg & , \text{ if } V(t) - V_0 \leq 0 \\ -\mu mg & , \text{ if } V(t) - V_0 > 0 \end{cases} \quad (6.25)$$

where  $\mu$  is the coefficient of friction.



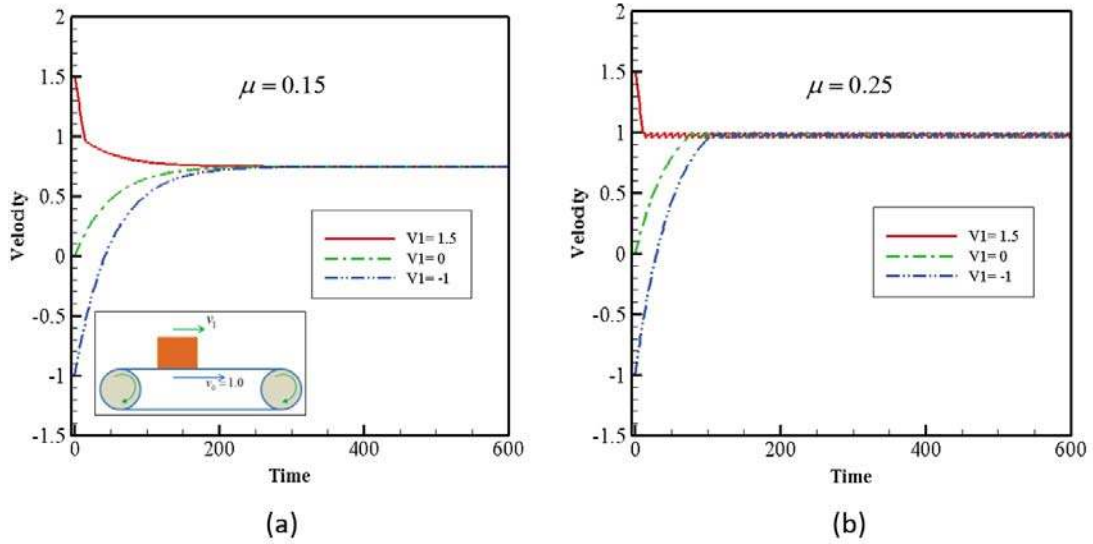


**Figure 6.3** Velocity evolution of an object dropped on a conveyor. Different line types and colors are corresponding to different initial velocity for the dropping object, *i.e.*,  $v_1$ . In all solving processes,  $v_0 = 1$ ,  $m = 5$ ,  $g = 1$ ,  $M = 1$ ,  $M' = 50$ , and  $\Delta t = 0.1$ .

Figure 6.3 presents the velocity as a function of time for different coefficients of friction and initial velocity of the object, respectively. In the case of small  $\mu$  (Figure 6.3a), the friction force is not sufficient for the object to obtain a high enough speed to catch up with the moving belt, thus leaving a constant relative velocity between the object and the conveyor belt. This is pretty straightforward. When  $\mu$  is large enough, as can be seen in Figure 6.3b, the object eventually obtains a velocity identical to the moving belt. Although, strictly speaking, the ultimate  $V(t)$  is vibrating around  $v_0$ , the time-averaged relative sliding vanishes and won't show up again. What's worth noting here is, firstly, in Figure 6.3b, even though the friction is larger than the force what the object need to stay at a velocity  $v_0$ , *i.e.*,  $\mu mg > MV_0$ , the terminal speed can't excess  $v_0$ . The second interesting

finding here is that, no matter what initial velocity the object has, the terminal speed is always the same for a given system. The two details suggest that the friction always resists relative motion regardless of the direction of the relative sliding. The formulation automatically leads the velocity to evolve in the right direction; this is exactly what we meant by self-adjusting. This case demonstrates that the proposed formulation automatically reproduced the feature of the static friction without distinguishing it from kinetic friction. The *by-pass* technique and *self-adjusting* feature enables the DIFA model to phenomenologically simulate a dynamic system with real sense of friction in a high computing efficiency.

#### 6.4.1.3 Problem of Sphere Rolling Downhill

So far we checked the validity of the equations of motion for the driving force only and friction force only cases, now let's think about a more complicated case with driving force, friction and rolling considerations. Image a solid sphere deposited on an inclined plane starts to roll down, how the sphere rolls/slides with or without the friction between the sphere and the plane? Letting the coordinate axis run parallel to the plane, where downhill is the positive direction, we may rewrite the equations of motion as

$$F_T - F^f = MV(t) + M'\Delta V(t) \quad (6.26)$$

$$F^f a = N\Omega(t) + N'\Delta\Omega(t) \quad (6.27)$$

where  $a$  is the radius of the sphere, and the friction can be determined via

$$F^f = \begin{cases} \mu F_N, & \text{if } \Omega(t)a - V_0 > 0 \\ -\mu F_N, & \text{if } \Omega(t)a - V_0 \leq 0 \end{cases} \quad (6.28)$$

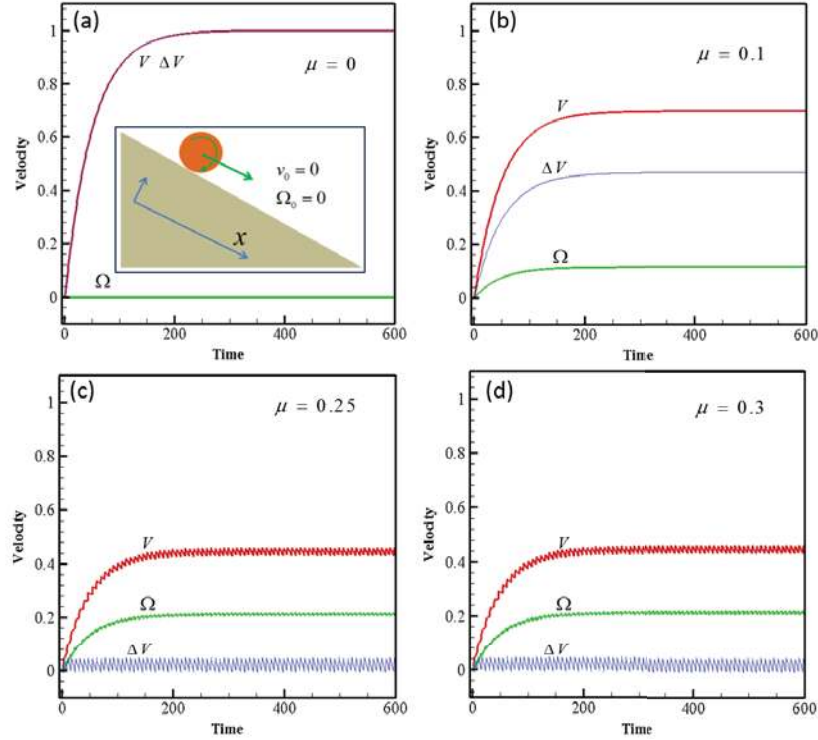


**Figure 6.4** Linear and angular velocity evolution for a sphere released on an inclined plane. Four cases with different coefficients of friction are presented. The relative sliding velocity between the ball and sloped plane was also plotted. Initial velocity for the ball is 0. In all solving processes,  $a = 2$ ,  $m = 5$ ,  $g = 1$ ,  $M = 1$ ,  $N = 5.2$ ,  $M' = 50$ ,  $N' = 50$  and  $\Delta t = 0.1$

Figure 6.4 shows the calculated results for linear velocity, angular velocity of the sphere, and relative sliding between the sphere and inclined plane. Without any surprise, in Figure 6.4a we see that the sphere sliding-without-rolling down the sloped plane. On the contrast, in Figure 6.4b the friction produces a torque which tends to increase the angular velocity of the sphere while decreasing its linear velocity. Note that the relative

sliding still occurs because of the insufficient friction; the sphere is actually sliding-with-rolling downhill. Increasing the value of  $\mu$  will continue to decrease the terminal linear velocity and increase terminal angular velocity, until to a critical value of  $\mu$  at which the sphere has eventually achieved pure rolling motion. Further increasing  $\mu$  won't change the terminal angular and linear velocity, as supported by the comparison between Figure 6.4c and 6.4d. In conclusion, the proposed equations of motion reproduced the physical process of “rolling downhill” with enough features and details with friction consideration.

Thus, the robustness and validity of the modified equations of motion have been verified in different cases involving a driving force, friction force, and combined driving/frictional forces, respectively. In the tests, the modified equations of motion phenomenologically produced the frictional behaviors of system without discriminating between the static and kinetic friction forces. In addition, by introducing a damping factor to the equations of motion, the discontinuity of velocity was prevented, which will provide a good numerical stability for a computational simulation.

## 6.4.2 Simulation of Particle Packing Process

For complex particle packing process where multi-touch problem is involved, it's required to implement the complete model for computer simulations, in which the continuous space is discretized into computational grids of size  $l_0$ . As illustrated by Figure 1 in [202], the particles are able to continuously translate and rotate on discrete computational grids attributing to the diffuse interface field. The dimensionless parameter  $\kappa = 75$  is used in Eq. (1). A time increment  $\Delta t = 0.1$  was used in the iteration of Eq. (6.14)

& (15). The developed DIFA model of particle packing is formulated for the general three-dimensional (3D) cases. In this article, two-dimensional (2D) simulations are performed to demonstrate its capabilities.

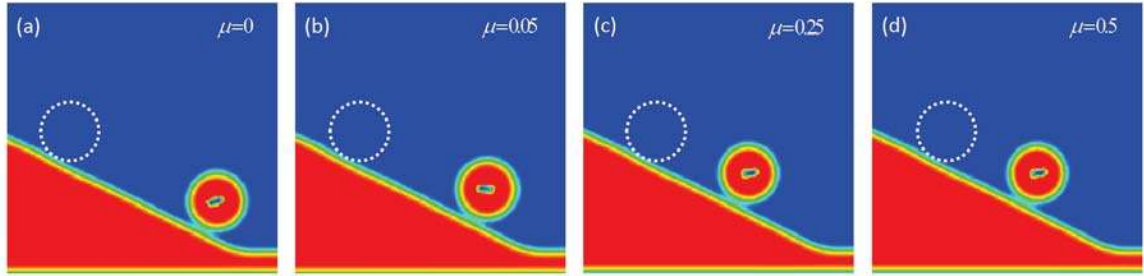


**Figure 6.5** DIFA simulation of a sphere sliding/rolling downhill. Four cases with different coefficients of friction are presented. The dotted circle is the initial position of the sphere. The hole on the sphere is intended to track the rotation of the sphere.

As mentioned in the Section 6.3.3, the friction was exerted on an *effective* contact point. In order to verify the accuracy of the treatment for friction forces, we began by considering again the problem of a sphere rolling down an inclined plane, and visualizing the results in Figure 6.5. Generally speaking, the computational codes well reproduced the results obtained in *Case C* of 6.4.1. In the Figure 6.5a the sphere reached to the farthest due to the ideal sliding translation without any rotation. Then a rotation was observed when a small friction coefficient was introduced (Figure 6.5b). Both the spheres in Figure 6.5c & d obtained the maximum possible angular velocity and were purely rolling downhill, with their translational motion being badly reduced by the friction forces. All the detailed behaviors captured by the DIFA model were consistent with the results we obtained

directly from the equations of motion, suggesting that algorithm by which the friction are applied in the model is accurate and reliable.

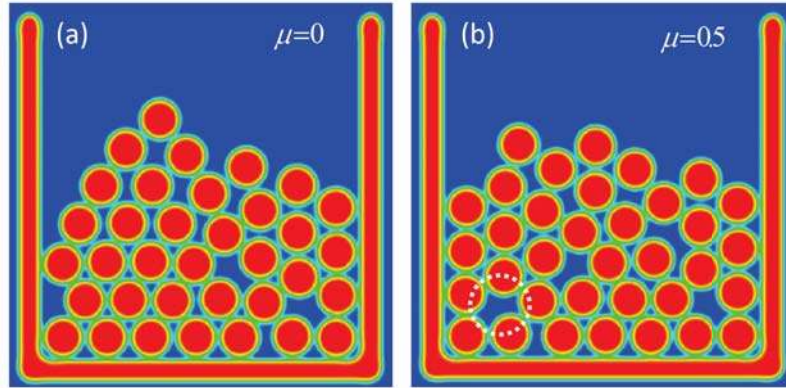


**Figure 6.6** DIFA simulation of a frictional and a frictionless packing structures. Note that the particle sequences are exactly the same for packing process producing (a) and (b).

Figure 6.6 shows us three packing patterns of identical spheres with different coefficients of friction. In simulations, balls were dropped sequentially from a random point above a container; during all the packing process the particle sequences are exactly the same, inspire of which, obvious difference between the final packing configuration is observed. The frictionless packing produced the most ordered pattern among the presented cases, while frictional packing process generated more vacancies/pores in the packing system. In order to demonstrate the role of friction in detail, the formation of a typical pore (highlighted in Figure 6.6b) is shown in Figure 6.7. Figure 6.7a(1-5) and 6.7b(1-5) are five snapshots of the simulated processes a and b, respectively. Let’s keep our eyes on the ball marked with “ $\times$ ”. At time  $t_1$ , there is practically no difference between the ball  $\times$  in Figure 6.7(a1) and (b1). Then at  $t_2$ , the ball  $\times$  is moving towards to the left because of

the friction force given by its downstairs' neighbor (compare Figure 6.7(a2) and (b2)). This diverged motion prevented the ball  $\times$  in Figure 6.7(b4) from occupying a lattice point as what it did in Figure 6.7(a4). Instead, the ball  $\times$  and its lower and upper neighbors, together pushed another ball (marked with  $\Delta$  in Figure 6.7(b5)) away from the lattice point position, leaving a pore in the packing pattern. The simulation shows that friction is playing an important role in the formation of packing defects and the determination of packing structure.

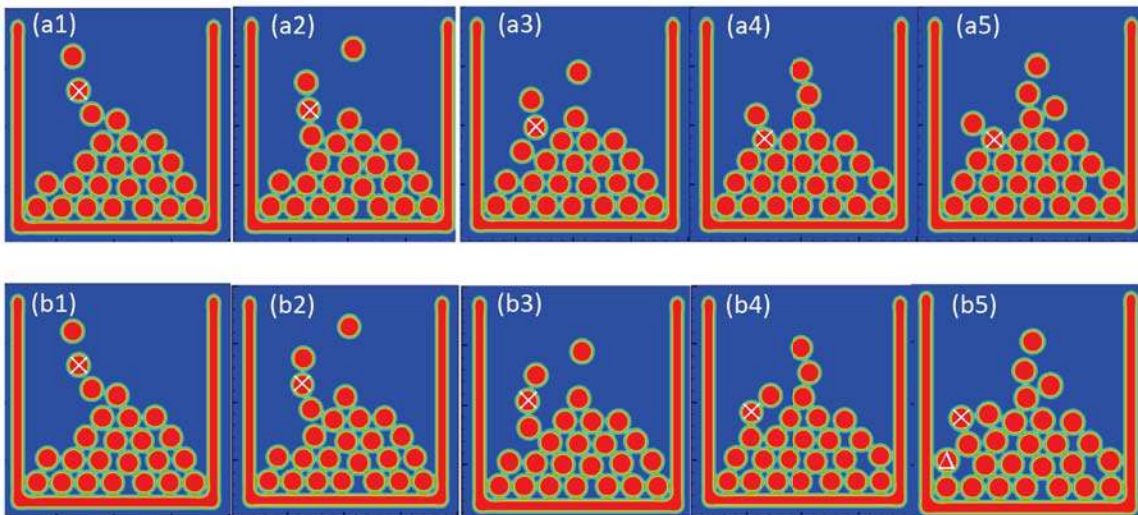


**Figure 6.7** Formation of a typical pore in the frictional packing process. For the purpose of comparison, the corresponding snap in the frictionless case are also presented in (a).

Another important feature of the DIFA model developed here is its capability to treat non-circle, arbitrarily shaped particles. For the purpose of demonstration, Figure 8 shows us a packing process of particles with hybrid shapes. As can be seen, the DIFA

model deals well with the short-range repulsive and friction, even for particles with arbitrary shapes and sizes.

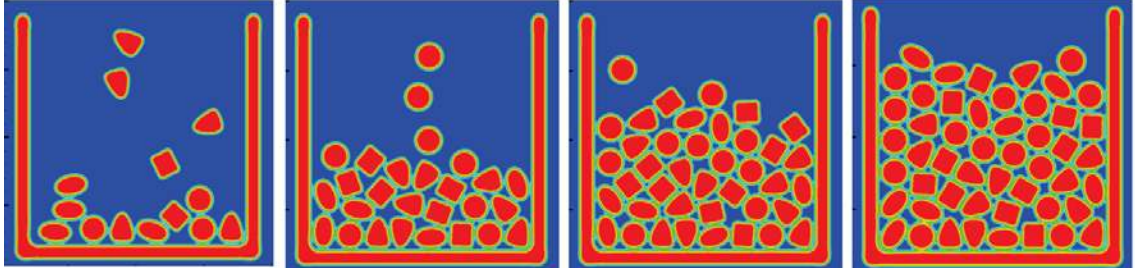


**Figure 6.8** DIFA simulation of packing process of multi-shaped particles.

## 6.5 Discussion and Conclusion

The computational model of arbitrarily shaped particles packing is based on diffuse interface field approach, DIFA. This model has several appealing features. Firstly, it automatically simulates the translation and rotation of arbitrarily shaped particles without explicitly tracking their surfaces. This is attributed to the use of diffuse interface field fields in the description of particle microstructure and its evolution. Secondly, the DIFA model well describes the frictional motions without calculating the value of static friction. The equations of motion used here offer a *self-adjusting* feature which allows the objects automatically evolve in the right way without identifying the transition between stick and slip. These features facilitate the implementation of the model in high computational efficiency.

As discussed before, we introduced a damping factor to the equations of motion Eq. (6.12) & (6.13), and considered it as analogue of as inertia. To illustrate further



the physical meaning of this concept, let's consider again the simplest *Case A* for example. According to Stokes' formula, the drag force  $F_D = MV$ , thus we can write Newton's second law for the ball as

$$mg - MV = m \frac{dV}{dt} . \quad (6.29)$$

It's easy to see the similarity between Eq. (6.29) and (6.23), and when  $M'$  denotes  $m / \Delta t$  as its value, these two equations converge. It means that, the *effective mass*  $M'$  combined the effect of both the real mass and the simulation time step on the velocity change. And in simulation,  $M'$  does not have to be equal to  $m / \Delta t$ , because, comparing with the velocity change  $\Delta V$ , we are more concerned with the final  $V$ . This offers an advantage that, one can achieve a better numerical stability by adjusting the magnitude of  $M'$  without losing the accuracy of ultimate velocity.

In the developed DIFA model, the friction is exerted on an effective contact point, and the treatment was verified carefully. But a natural question is, what if more than one contact point occurring between two objects? For example, as mentioned before, the container is dealt with as a special particle which keeps its position and orientation; but at the corners of such a container as shown in Figure 6.6~6.8, it's possible that a particle simultaneously touches the bottom and the wall of the container. Merging the two friction forces into one applying on the effective contact probably introduces faulty description of particle motion. The problem was treated as illustrated in Figure 6.9: the container was divided into three parts with convex shapes, each of which was treated a single particle

when calculating short-range repulsive forces and friction force; then they were coupled together in the simulation codes to output as a whole container, thus preventing the onset of the multi-touches between any particle and container. The same treatment is also applicable for complex concave particles.

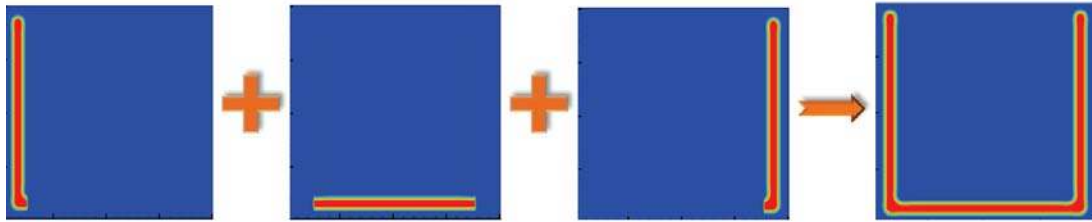


**Figure 6.9** Treatment of concave objects in the packing system.

The DIFA model developed in this chapter can be used to simulate the particle packing process accounting for the particle shape irregularity and friction. So several important process variables such as friction, particle shapes and size, container shapes and relative size can be investigated and this will be reported in a future publication. In addition, the DIFA model will also find its application in many material processes where particle shapes and friction are significantly involved. These processes include, for example, the storage and flow of granular materials in hoppers or tubes, which is important in pharmaceutical, food, agricultural and powder industries, and powder compaction process, which is crucial in ceramic industry and powder metallurgy.

# Chapter 7. Summary and Future Research

In this dissertation, computational simulations were conducted to study the microstructure – property – mechanism relations in ferroic composites. Phase field modeling was employed as the computing tool and the required models for ferroic composites were developed based on existing models for monolithic materials. Two representative ferroic composites, *i.e.*, two-phase particulate magnetoelectric (ME) composite and polymer matrix ferroelectric composite, were investigated and the learnt insights are summarized in this Chapter. The perspective of current study is also discussed.

## 7.1 Insights from Computational Study

For particulate ME composite:

Simulations found that in-situ electric poling of the ferroelectric phase within composite microstructures is crucial to obtaining the ME effect. 0-3 connectivity of isolated magnetostrictive phase embedded in continuous ferroelectric phase matrix is necessary, and small but finite electrical conductivity of isolated magnetic phase can beneficially enhance ME effect by both assisting effective poling and helping stabilize poled state of the ferroelectric phase. Optimum ME coefficient values can be achieved with appropriate bias magnetic field. The simulated evolution of magnetic and electric domains reveals complex domain-level strain-mediated coupling mechanisms between magnetization and polarization.

It is also revealed that longitudinal and transverse ME coefficients of 0-3 particulate composites with isotropic two-phase microstructures can be effectively tailored by controlling magnetic domain structures via internal residual stress engineering without resort to anisotropic two-phase microstructures (*e.g.*, 2-2 laminate, 1-3 fiber/rod). It suggests that co-sintering under uniaxial or biaxial stress rather than isostatic pressing is an effective route to engineer internal residual stress and magnetic domain structures of particulate ME composites, which may also offer a means to help eliminate cumbersome external bias magnetic field that is usually required to achieve optimal material response.

For polymer matrix ferroelectric composite:

We found that the macroscopic properties of the composites critically depend on the ferroelectric phase connectivity while are not sensitive to the sizes and internal grain structures of the ceramic particles. In order to fully exploit the ferroelectric properties of the particles embedded in the composite matrix, continuous ferroelectric phase connectivity is required. Without such continuous phase connectivity, the composites just behave like linear dielectric materials with very small dielectric constant, even though ferroelectric particles of large dielectric constant are used. Such composite behaviors are found to be dominated by depolarization field effect, which depends on the arrangement, alignment and, most importantly, connectivity of the ferroelectric particles.

Nonlinear polarization behavior associated with electric field-induced transition between paraelectric and ferroelectric phases in polymer matrix composites was also investigated. Theoretical analysis reveals that paraelectric→ferroelectric phase transition

can be induced by electric field along [100] but not [110] or [111] axis of a BaTiO<sub>3</sub> single crystal, and computer simulation further shows that [100]-textured polycrystalline BaTiO<sub>3</sub> is able to undergo field-induced phase transition and exhibit nonlinear polarization behavior. A critical degree (~20°) of [100] uniaxial texturing is determined by simulations that is required in order to achieve significantly increased dielectric capacity desired for high energy density storage application. In order to fully exploit the paraelectric↔ferroelectric phase transition and nonlinear polarization behavior in a polymer matrix composite, continuous paraelectric phase connectivity and [100] uniaxial texturing are required.

Additionally, a Diffuse Interface Field model was developed to simulate packing and motion in liquid phase which play a significant role in the fabrication of particulate-polymer composites. Several important processing variables such as friction, particle size and irregularity, container shapes and relative size were considered in the proposed model. Simulations show that the DIFA model is promising for studying the fabrication of particulate-polymer composites.

## **7.2 Future Research**

The simulations presented in this thesis were performed within an assumption of structural inhomogeneity and elastic homogeneity. The structural inhomogeneity allows us to take into account the realistic complex microstructure of ferroic composites, which is crucial for a study of microstructure – property – mechanism relations. The elastic homogeneity consideration ensures the computing efficiency of the sophisticated models,

which is also important for us to get enough data and learn the insights important for both rational design and practical application of ferroic composites. The developed phase field model for ferroic composites could be more sophisticated and realistic in future – by integrating the elastic inhomogeneity [Y.U. Wang, Y.M. Jin, A.G. Khachaturyan, “Phase Field Microelasticity Theory and Modeling of Elastically and Structurally Inhomogeneous Solid,” *J. Appl. Phys.*, **92**, 1351-1360, 2002]. After all, ferroic composites are structural and elastic inhomogeneous system. For example, the extrinsic ME effect in composites is a product property that results from the elastic interaction between the magnetostrictive phase and the piezoelectric phase; the modulus difference between the two active phases influences the strain transfer and the coupling between them, as well as the resultant ME response of the composites. The integration of elastic inhomogeneity to the phase field model could potentially provide more accurate simulations and open up new areas for exploration of ferroic materials and composites.

# References

- [1] K. Aizu, *Journal of the Physical Society of Japan*, 27 (1969) 387–396.
- [2] V.K. Wadhawan, *Reson*, 7 (2002) 15-24.
- [3] J.F. Scott, *Ferroelectrics*, 236 (2000) 247-258.
- [4] J.F. Scott, *Science*, 315 (2007) 954-959.
- [5] M. Dawber, J.F. Scott, *Journal of Physics: Condensed Matter*, 16 (2004) L515.
- [6] C.J. Dias, D.K. Das-Gupta, *Dielectrics and Electrical Insulation*, *IEEE Transactions on*, 3 (1996) 706-734.
- [7] F. Jona, G. Shirane, *Ferroelectric crystals*, Dover New York, 1993.
- [8] B. Noheda, N. Cereceda, T. Iglesias, G. Lifante, J.A. Gonzalo, H.T. Chen, Y.L. Wang, *Physical Review B*, 51 (1995) 16388-16391.
- [9] V. Keppens, *Nat Mater*, 12 (2013) 952-953.
- [10] R.A. Steven, A.S. Henry, *Smart Materials and Structures*, 16 (2007) R1.
- [11] P.M. Moubarak, P. Ben-Tzvi, M.E. Zaghoul, *Sensors Journal*, *IEEE*, 12 (2012) 1033-1042.
- [12] H. Irschik, *Engineering Structures*, 24 (2002) 5-11.
- [13] K.K. Shung, J.M. Cannata, Q.F. Zhou, *J Electroceram*, 19 (2007) 141-147.
- [14] A.M. Flynn, L.S. Tavrow, S.F. Bart, R.A. Brooks, D. Ehrlich, K.R. Udayakumar, L.E. Cross, *Microelectromechanical Systems*, *Journal of*, 1 (1992) 44-51.
- [15] D. Shuxiang, S.P. Lim, K.H. Lee, Z. Jingdong, L.C. Lim, K. Uchino, *Ultrasonics, Ferroelectrics, and Frequency Control*, *IEEE Transactions on*, 50 (2003) 361-367.
- [16] B. Koc, S. Cagatay, K. Uchino, *Ultrasonics, Ferroelectrics, and Frequency Control*, *IEEE Transactions on*, 49 (2002) 495-500.

- [17] X. Wang, J. Song, J. Liu, Z.L. Wang, *Science*, 316 (2007) 102-105.
- [18] S.-E. Park, T.R. Shrout, *Ultrasonics, Ferroelectrics, and Frequency Control*, IEEE Transactions on, 44 (1997) 1140-1147.
- [19] C.J. Harvey, J.M. Pilcher, R.J. Eckersley, M.J.K. Blomley, D.O. Cosgrove, *Clinical Radiology*, 57 157-177.
- [20] C. Kittel, New York: Wiley, 1976, 5th ed., 1 (1976).
- [21] M.B. Moffett, A.E. Clark, M. Wun-Fogle, J. Linberg, J.P. Teter, E.A. McLaughlin, *The Journal of the Acoustical Society of America*, 89 (1991) 1448-1455.
- [22] A.E. Clark, J.B. Restorff, M. Wun-Fogle, T.A. Lograsso, D.L. Schlagel, *Magnetics*, IEEE Transactions on, 36 (2000) 3238-3240.
- [23] I.D. Mayergoyz, G. Engdahl, *Handbook of giant magnetostrictive materials*, Elsevier, 1999.
- [24] H. Kwun, K. Bartels, *Ultrasonics*, 36 (1998) 171-178.
- [25] F. Claeysen, N. Lhermet, R. Le Letty, P. Bouchilloux, *Journal of Alloys and Compounds*, 258 (1997) 61-73.
- [26] L. Sandlund, M. Fahlander, T. Cedell, A.E. Clark, J.B. Restorff, M. Wun-Fogle, *Journal of Applied Physics*, 75 (1994) 5656-5658.
- [27] L. Ching Yin, O. Siu Wing, C. Helen Lai Wa, *Magnetics*, IEEE Transactions on, 42 (2006) 3111-3113.
- [28] T.A. Duenas, G.P. Carman, *Journal of Applied Physics*, 90 (2001) 2433-2439.
- [29] Z.J. Guo, S.C. Busbridge, A.R. Piercy, Z.D. Zhang, X.G. Zhao, B.W. Wang, *Applied Physics Letters*, 78 (2001) 3490-3492.
- [30] J. Hudson, S.C. Busbridge, A.R. Piercy, *Journal of Applied Physics*, 83 (1998) 7255-7257.



- [31] S.R. Kim, S.Y. Kang, J.K. Park, J.T. Nam, D. Son, S.H. Lim, *Journal of Applied Physics*, 83 (1998) 7285-7287.
- [32] N. Nersessian, S.-W. Or, G.P. Carman, *Journal of Magnetism and Magnetic Materials*, 263 (2003) 101-112.
- [33] M. Pasquale, S.H. Lim, *Journal of Applied Physics*, 85 (1999) 4633-4635.
- [34] L. Ruiz de Angulo, J.S. Abell, I.R. Harris, *Journal of Magnetism and Magnetic Materials*, 157-158 (1996) 508-509.
- [35] O. Siu Wing, N. Nersessian, G.P. Carman, *Magnetics, IEEE Transactions on*, 40 (2004) 71-77.
- [36] S. Wing Or, N. Nersessian, G.P. Carman, *Journal of Magnetism and Magnetic Materials*, 262 (2003) L181-L185.
- [37] W. Eerenstein, N. Mathur, J. Scott, *nature*, 442 (2006) 759-765.
- [38] N.A. Spaldin, M. Fiebig, *Science*, 309 (2005) 391-392.
- [39] C.-W. Nan, M. Bichurin, S. Dong, D. Viehland, G. Srinivasan, *Journal of Applied Physics*, 103 (2008) 031101.
- [40] M. Fiebig, *Journal of Physics D: Applied Physics*, 38 (2005) R123.
- [41] S.-W. Cheong, M. Mostovoy, *Nature materials*, 6 (2007) 13-20.
- [42] C. Rodríguez, M. Rodríguez, I. Orue, J. Vilas, J. Barandiarán, M. Gubieda, L. Leon, *Sensors and Actuators A: Physical*, 149 (2009) 251-254.
- [43] R.D. Kornbluh, R. Pelrine, Q. Pei, S. Oh, J. Joseph, *Proc. SPIE 3987, Smart Structures and Materials 2000: Electroactive Polymer Actuators and Devices (EAPAD)*, 2000, pp. 51-64.
- [44] H. Meng, *Appl. Phys. Lett.*, 96 (2010) 102501.
- [45] S. Lim, S. Kim, S. Kang, J. Park, J. Nam, D. Son, *Journal of magnetism and magnetic materials*, 191 (1999) 113-121.

- [46] S.-E. Park, T.R. ShROUT, *Journal of Applied Physics*, 82 (1997) 1804-1811.
- [47] G.D. Shaffer, *Journal of Field Archaeology*, 20 (1993) 59-75.
- [48] D. Brigante, *NEW COMPOSITE MATERIALS*, Springer, 2013.
- [49] T. Lottermoser, T. Lonkai, U. Amann, D. Hohlwein, J. Ihringer, M. Fiebig, *Nature*, 430 (2004) 541-544.
- [50] T. Goto, T. Kimura, G. Lawes, A. Ramirez, Y. Tokura, *Physical review letters*, 92 (2004) 257201.
- [51] W. Prellier, M. Singh, P. Murugavel, *Journal of Physics: Condensed Matter*, 17 (2005) R803.
- [52] T. Kimura, T. Goto, H. Shintani, K. Ishizaka, T. Arima, Y. Tokura, *Nature*, 426 (2003) 55-58.
- [53] N.A. Hill, *The Journal of Physical Chemistry B*, 104 (2000) 6694-6709.
- [54] C.-W. Nan, *Physical Review B*, 50 (1994) 6082.
- [55] R. Newnham, D. Skinner, L. Cross, *Materials Research Bulletin*, 13 (1978) 525-536.
- [56] J. Van Suchtelen, *Philips Res. Rep*, 27 (1972) 28-37.
- [57] Y. Tang, X. Chen, Y. Li, X. Zheng, *Materials science & engineering. B, Solid-state materials for advanced technology*, 116 (2005) 150-155.
- [58] M.I. Bichurin, I.A. Kornev, V.M. Petrov, I.V. Lisnevskaya, *Ferroelectrics*, 204 (1997) 289-297.
- [59] J. Ryu, A. Carazo, K. Uchino, H.-E. Kim, *J Electroceram*, 7 (2001) 17-24.
- [60] S.L. Kadam, K.K. Patankar, V.L. Mathe, M.B. Kothale, R.B. Kale, B.K. Chougule, *J Electroceram*, 9 (2002) 193-198.
- [61] P.M. Raccach, J.B. Goodenough, *Journal of Applied Physics*, 39 (1968) 1209-1210.
- [62] M. Zeng, J.G. Wan, Y. Wang, H. Yu, J.-M. Liu, X.P. Jiang, C.W. Nan, *Journal of Applied Physics*, 95 (2004) 8069-8073.

- [63] I. Rashed Adnan, P. Shashank, Japanese Journal of Applied Physics, 45 (2006) L128.
- [64] K. Patankar, V. Mathe, R. Mahajan, S. Patil, R.M. Reddy, K. SivaKumar, Materials Chemistry and physics, 72 (2001) 23-29.
- [65] K. Patankar, S. Patil, K. Sivakumar, R. Mahajan, Y. Kolekar, M. Kothale, Materials chemistry and physics, 65 (2000) 97-102.
- [66] G. Srinivasan, C.P. DeVreugd, C.S. Flattery, V.M. Laletsin, N. Paddubnaya, Applied Physics Letters, 85 (2004) 2550-2552.
- [67] J.-g. Wan, H. Zhang, X. Wang, D. Pan, J.-m. Liu, G. Wang, Applied Physics Letters, 89 (2006) 122914.
- [68] S.Q. Ren, L.Q. Weng, S.H. Song, F. Li, J.G. Wan, M. Zeng, J Mater Sci, 40 (2005) 4375-4378.
- [69] L. Weng, Y. Fu, S. Song, J. Tang, J. Li, Scripta Materialia, 56 (2007) 465-468.
- [70] Q.H. Jiang, Z.J. Shen, J.P. Zhou, Z. Shi, C.-W. Nan, Journal of the European Ceramic Society, 27 (2007) 279-284.
- [71] K.-p. Chen, C. Li, X. Zhang, Y. Huang, Materials Letters, 57 (2002) 20-23.
- [72] J. Ryu, S. Priya, A.V. Carazo, K. Uchino, H.-E. Kim, Journal of the American Ceramic Society, 84 (2001) 2905-2908.
- [73] R. Jungho, C. Alfredo Vázquez, U. Kenji, K. Hyoun-Ee, Japanese Journal of Applied Physics, 40 (2001) 4948.
- [74] S. Dong, J.-F. Li, D. Viehland, Applied Physics Letters, 83 (2003) 2265-2267.
- [75] G. Srinivasan, E.T. Rasmussen, J. Gallegos, R. Srinivasan, Y.I. Bokhan, V.M. Laletin, Physical Review B, 64 (2001) 214408.
- [76] G. Srinivasan, E.T. Rasmussen, B.J. Levin, R. Hayes, Physical Review B, 65 (2002) 134402.

- [77] G. Srinivasan, R. Hayes, M.I. Bichurin, *Solid State Communications*, 128 (2003) 261-266.
- [78] G. Srinivasan, E.T. Rasmussen, R. Hayes, *Physical Review B*, 67 (2003) 014418.
- [79] J. Zhai, Z. Xing, S. Dong, J. Li, D. Viehland, *Applied Physics Letters*, 88 (2006) 062510.
- [80] S. Dong, J. Zhai, F. Bai, J. Li, D. Viehland, T.A. Lograsso, *Journal of Applied Physics*, 97 (2005) 103902.
- [81] S. Dong, J. Zhai, J. Li, D. Viehland, *Applied Physics Letters*, 88 (2006) 082907.
- [82] S. Dong, J. Zhai, J. Li, D. Viehland, *Applied Physics Letters*, 89 (2006) 252904.
- [83] S. Dong, J. Zhai, J.-F. Li, D. Viehland, *Applied Physics Letters*, 89 (2006) 122903.
- [84] S. Dong, J. Zhai, J.F. Li, D. Viehland, M.I. Bichurin, *Applied Physics Letters*, 89 (2006) 243512.
- [85] J. Zhai, J. Li, S. Dong, D. Viehland, M.I. Bichurin, *Journal of Applied Physics*, 100 (2006) 124509.
- [86] S. Dong, J.G. Bai, J. Zhai, J.-F. Li, G.-Q. Lu, D. Viehland, S. Zhang, T.R. Shrout, *Applied Physics Letters*, 86 (2005) 182506.
- [87] H. Zheng, J. Wang, S.E. Lofland, Z. Ma, L. Mohaddes-Ardabili, T. Zhao, L. Salamanca-Riba, S.R. Shinde, S.B. Ogale, F. Bai, D. Viehland, Y. Jia, D.G. Schlom, M. Wuttig, A. Roytburd, R. Ramesh, *Science*, 303 (2004) 661-663.
- [88] H. Zheng, J. Wang, L. Mohaddes-Ardabili, M. Wuttig, L. Salamanca-Riba, D.G. Schlom, R. Ramesh, *Applied Physics Letters*, 85 (2004) 2035-2037.
- [89] F. Zavaliche, H. Zheng, L. Mohaddes-Ardabili, S.Y. Yang, Q. Zhan, P. Shafer, E. Reilly, R. Chopdekar, Y. Jia, P. Wright, D.G. Schlom, Y. Suzuki, R. Ramesh, *Nano Letters*, 5 (2005) 1793-1796.
- [90] J.G. Wan, X.W. Wang, Y.J. Wu, M. Zeng, Y. Wang, H. Jiang, W.Q. Zhou, G.H. Wang, J.-M. Liu, *Applied Physics Letters*, 86 (2005) 122501.

- [91] P. Murugavel, P. Padhan, W. Prellier, *Applied Physics Letters*, 85 (2004) 4992-4994.
- [92] P. Murugavel, D. Saurel, W. Prellier, C. Simon, B. Raveau, *Applied Physics Letters*, 85 (2004) 4424-4426.
- [93] M.P. Singh, W. Prellier, L. Mechin, C. Simon, B. Raveau, *Journal of Applied Physics*, 99 (2006) 024105.
- [94] N. Ortega, P. Bhattacharya, R.S. Katiyar, P. Dutta, A. Manivannan, M.S. Seehra, I. Takeuchi, S.B. Majumder, *Journal of Applied Physics*, 100 (2006) 126105.
- [95] W. Eerenstein, M. Wiora, J.L. Prieto, J.F. Scott, N.D. Mathur, *Nat Mater*, 6 (2007) 348-351.
- [96] Y.G. Ma, W.N. Cheng, M. Ning, C.K. Ong, *Applied Physics Letters*, 90 (2007) -.
- [97] X.M. Chen, Y.H. Tang, I.-W. Chen, Z.C. Xu, S.Y. Wu, *Journal of Applied Physics*, 96 (2004) 6520-6522.
- [98] Y. Li, X. Chen, Y. Lin, Y. Tang, *Journal of the European Ceramic Society*, 26 (2006) 2839-2844.
- [99] M. Xanthos, *Functional Fillers for Plastics*, WILEY-VCH Verlag GmbH & Co KGaA, Weinheim, 2005.
- [100] J. William D. Callister, *Materials Science and Engineering: An Introduction*, 6th Edition, Wiley-VCH, USA, 2005.
- [101] J. Chatterjee, Y. Haik, C.J. Chen, *Journal of Magnetism and Magnetic Materials*, 246 (2002) 382-391.
- [102] J.L. Wilson, P. Poddar, N.A. Frey, H. Srikanth, K. Mohomed, J.P. Harmon, S. Kotha, J. Wachsmuth, *Journal of Applied Physics*, 95 (2004) 1439-1443.
- [103] G. Filipcsei, I. Csetneki, A. Szilágyi, M. Zrínyi, *Magnetic Field-Responsive Smart Polymer Composites, Oligomers # Polymer Composites # Molecular Imprinting*, Springer Berlin / Heidelberg, 2007, pp. 137-189.

- [104] Q. Wang, L. Zhu, *Journal of Polymer Science Part B: Polymer Physics*, 49 (2011) 1421-1429.
- [105] S. Ogitani, S.A. Bidstrup-Allen, P.A. Kohl, *Advanced Packaging, IEEE Transactions on*, 23 (2000) 313-322.
- [106] H.C. Pant, M.K. Patra, A. Verma, S.R. Vadera, N. Kumar, *Acta Materialia*, 54 (2006) 3163-3169.
- [107] H.-I. Hsiang, K.-Y. Lin, F.-S. Yen, C.-Y. Hwang, *J Mater Sci*, 36 (2001) 3809-3815.
- [108] H. Lee, x, Gyu, H.-G. Kim, *Journal of Applied Physics*, 67 (1990) 2024-2028.
- [109] N. Guo, S.A. DiBenedetto, P. Tewari, M.T. Lanagan, M.A. Ratner, T.J. Marks, *Chemistry of Materials*, 22 (2010) 1567-1578.
- [110] T.R. Gururaja, W.A. Schulze, T.R. Shrout, A. Safari, L. Webster, L.E. Cross, *Ferroelectrics*, 39 (1981) 1245-1248.
- [111] Y. Bai, Z.-Y. Cheng, V. Bharti, H.S. Xu, Q.M. Zhang, *Applied Physics Letters*, 76 (2000) 3804-3806.
- [112] D.Q. Tan, C. Qin, F. Xiaomei, P. Irwin, Y.U. Wang, *Ultrasonics, Ferroelectrics, and Frequency Control, IEEE Transactions on*, 60 (2013) 1619-1624.
- [113] Y. Benveniste, *Physical Review B*, 51 (1995) 16424.
- [114] I. Getman, *Ferroelectrics*, 162 (1994) 45-50.
- [115] C.-W. Nan, D.R. Clarke, *Journal of the American Ceramic Society*, 80 (1997) 1333-1340.
- [116] G. Harshe, J.P. Dougherty, R.E. Newnham, 1993 North American Conference on Smart Structures and Materials, International Society for Optics and Photonics, 1993, pp. 224-235.
- [117] M.I. Bichurin, V.M. Petrov, O.V. Ryabkov, S.V. Averkin, G. Srinivasan, *Physical Review B*, 72 (2005) 060408.

- [118] H. Haitao, Z. Li Min, *Journal of Physics D: Applied Physics*, 37 (2004) 3361.
- [119] D.A. Filippov, *Tech. Phys. Lett.*, 30 (2004) 351-353.
- [120] T.-L. Wu, J.H. Huang, *International Journal of Solids and Structures*, 37 (2000) 2981-3009.
- [121] L. Li, J. Li, *Physical Review B*, 73 (2006) 184416.
- [122] S. Srinivas, J.Y. Li, *Acta Materialia*, 53 (2005) 4135-4142.
- [123] J.Y. Li, *International Journal of Engineering Science*, 38 (2000) 1993-2011.
- [124] J. Lee, J.G. Boyd Iv, D.C. Lagoudas, *International Journal of Engineering Science*, 43 (2005) 790-825.
- [125] T. Chen, *Journal of the Mechanics and Physics of Solids*, 45 (1997) 385-398.
- [126] C.-W. Nan, *Journal of Applied Physics*, 82 (1997) 5268-5269.
- [127] S. Dong, J. Cheng, J.F. Li, D. Viehland, *Applied Physics Letters*, 83 (2003) 4812-4814.
- [128] Y.Y. Huang, Y.M. Jin, *Applied Physics Letters*, 93 (2008) 142504-142504-142503.
- [129] Y.U. Wang, *J Mater Sci*, 44 (2009) 5225-5234.
- [130] B. Jaffe, *Piezoelectric ceramics*, Elsevier, 2012.
- [131] C. Brosseau, A. Beroual, A. Boudida, *Journal of Applied Physics*, 88 (2000) 7278-7288.
- [132] R. Yang, J. Qu, T. Marinis, C.P. Wong, *Components and Packaging Technologies, IEEE Transactions on*, 23 (2000) 680-683.
- [133] B.J.P. Adohi, C.V. Bouanga, K. Fatyeyeva, M. Tabellout, *Journal of Physics D: Applied Physics*, 42 (2009) 015302.
- [134] G. Liu, C.-W. Nan, N. Cai, Y. Lin, *International Journal of Solids and Structures*, 41 (2004) 4423-4434.

- [135] Y.X. Liu, J.G. Wan, J.-M. Liu, C.W. Nan, *Journal of Applied Physics*, 94 (2003) 5111-5117.
- [136] G. Liu, C.-W. Nan, N. Cai, Y. Lin, *Journal of Applied Physics*, 95 (2004) 2660-2664.
- [137] K. Zhou, S.A. Boggs, R. Ramprasad, M. Aindow, C. Erkey, S.P. Alpay, *Applied Physics Letters*, 93 (2008) 102908.
- [138] K.S. Maxwell, J.D. Whitcomb, Z. Ounaies, A. Barhoumi, *Journal of Intelligent Material Systems and Structures*, 21 (2010) 1073-1084.
- [139] V. Myroshnychenko, C. Brosseau, *Journal of Applied Physics*, 97 (2005) 044101.
- [140] R. Abraham, R. Guo, A.S. Bhalla, *Ferroelectrics*, 315 (2005) 1-15.
- [141] X. Zhao, Y. Wu, Z. Fan, F. Li, *Journal of Applied Physics*, 95 (2004) 8110-8117.
- [142] C. Ang, Z. Yu, R. Guo, A.S. Bhalla, *Journal of Applied Physics*, 93 (2003) 3475-3480.
- [143] M.E. Azimi, P.K. Ghosh, *Modelling and Simulation in Materials Science and Engineering*, 2 (1994) 1093.
- [144] H. Cheng, S. Torquato, *Physical Review B*, 56 (1997) 8060.
- [145] A. Beroual, C. Brosseau, *Dielectrics and Electrical Insulation*, *IEEE Transactions on*, 8 (2001) 921-929.
- [146] L.-Q. Chen, *Annual review of materials research*, 32 (2002) 113-140.
- [147] N. Moelans, B. Blanpain, P. Wollants, *Calphad*, 32 (2008) 268-294.
- [148] Y.M. Jin, *Acta Materialia*, 57 (2009) 2488-2495.
- [149] Y.U. Wang, *Applied Physics Letters*, 96 (2010) 232901.
- [150] A.F. Devonshire, *Philos. Mag.*, 40 (1949) 1040.
- [151] S. Semenovskaya, A.G. Khachatryan, *Journal of Applied Physics*, 83 (1998) 5125-5136.



- [152] A. Huber, R. Schäfer, Springer, Berlin, 1998.
- [153] Y.M. Jin, Applied Physics Letters, 103 (2013) 021906-021906-021904.
- [154] A.E. Clark, J.P. Teter, O.D. McMasters, Journal of Applied Physics, 63 (1988) 3910-3912.
- [155] P.P. Wu, X.Q. Ma, J.X. Zhang, L.Q. Chen, Philosophical Magazine, 90 (2010) 125-140.
- [156] J. Zhang, Y. Li, D. Schlom, L. Chen, F. Zavaliche, R. Ramesh, Q. Jia, Applied physics letters, 90 (2007) 052909.
- [157] Y. Ni, A.G. Khachatryan, Journal of Applied Physics, 102 (2007) 113506.
- [158] Y.U. Wang, D.Q. Tan, J. Krahn, Journal of Applied Physics, 110 (2011) 044103.
- [159] Y. Wang, J Mater Sci, 44 (2009) 5225-5234.
- [160] J.v.d. Boomgaard, A.M.J.G. van Run, J. Van Suchtelen, Ferroelectrics, 14 (1976) 727-728.
- [161] J. Van Den Boomgaard, A.M.J.G. Van Run, J.V. Suchtelen, Ferroelectrics, 10 (1976) 295-298.
- [162] J. Ma, J. Hu, Z. Li, C.-W. Nan, Advanced Materials, 23 (2011) 1062-1087.
- [163] S. Lopatin, I. Lopatina, I. Lisnevskaya, Ferroelectrics, 162 (1994) 63-68.
- [164] A. Amin, M.J. Haun, B. Badger, H. McKinstry, L.E. Cross, Ferroelectrics, 65 (1985) 107-130.
- [165] M.J. Haun, Z.Q. Zhuang, E. Furman, S.-J. Jang, L.E. Cross, Journal of the American Ceramic Society, 72 (1989) 1140-1144.
- [166] Z. Shi, C.-W. Nan, J. Zhang, J. Ma, J.-F. Li, Journal of Applied Physics, 99 (2006) 124108.
- [167] M. Wun-Fogle, J.B. Restorff, A.E. Clark, E. Dreyer, E. Summers, Journal of Applied Physics, 97 (2005) 10M301-310M301-303.

- [168] Y.U. Wang, Y.M. Jin, A.G. Khachaturyan, *Acta Materialia*, 51 (2003) 4209-4223.
- [169] A. Hubert, R. Schafer, A. Hubert, R. Schafer, *Magnetic domains*, Springer, 1998.
- [170] I.D.M. Giorgio Bertotti, *The Science of Hysteresis*, Elsevier, 2005.
- [171] R.E. Newnham, D.P. Skinner, L.E. Cross, *Materials Research Bulletin*, 13 (1978) 525-536.
- [172] C.J. Dias, D.K. Das - Gupta, *Journal of Applied Physics*, 74 (1993) 6317-6321.
- [173] Y.P. Mao, S.Y. Mao, Z.-G. Ye, Z.X. Xie, L.S. Zheng, *Journal of Applied Physics*, 108 (2010) 014102.
- [174] A. Pelaiz-Barranco, *Applied Physics Letters*, 100 (2012) 212903-212903-212903.
- [175] W.-F. Rao, Y.U. Wang, *Applied Physics Letters*, 92 (2008) 102905.
- [176] Y.P. Mamunya, V.V. Davydenko, P. Pissis, E.V. Lebedev, *European Polymer Journal*, 38 (2002) 1887-1897.
- [177] V. Tomer, C.A. Randall, G. Polizos, J. Kostelnick, E. Manias, *Journal of Applied Physics*, 103 (2008) 034115.
- [178] M. Lines, A. Glass, (1977).
- [179] C. Kittel, *Physical Review*, 82 (1951) 729-732.
- [180] B. Jaffe, *Proceedings of the IRE*, 49 (1961) 1264-1267.
- [181] G.R. Love, *Journal of the American Ceramic Society*, 73 (1990) 323-328.
- [182] A. Bell, *Journal of Applied Physics*, 89 (2001) 3907-3914.
- [183] M.T. Sebastian, H. Jantunen, *International Journal of Applied Ceramic Technology*, 7 (2010) 415-434.
- [184] R. Popielarz, C.K. Chiang, R. Nozaki, J. Obrzut, *Macromolecules*, 34 (2001) 5910-5915.
- [185] V. Tomer, C.A. Randall, *Journal of Applied Physics*, 104 (2008) 074106.

- [186] B.D. Lubachevsky, F.H. Stillinger, *Journal of Statistical Physics*, 60 (1990) 561-583.
- [187] S. Torquato, F.H. Stillinger, *Reviews of Modern Physics*, 82 (2010) 2633-2672.
- [188] S. Torquato, T.M. Truskett, P.G. Debenedetti, *Physical Review Letters*, 84 (2000) 2064-2067.
- [189] S.F. Edwards, D.V. Grinev, *Chemical Engineering Science*, 56 (2001) 5451-5455.
- [190] C. Song, P. Wang, H.A. Makse, *Nature*, 453 (2008) 629-632.
- [191] W.M. Visscher, M. Bolsterli, *Nature*, 239 (1972) 504-507.
- [192] O. Tsuyoshi, O. Takashi, *Journal of Physics: Condensed Matter*, 16 (2004) 6651.
- [193] N.D. Aparicio, A.C.F. Cocks, *Acta Metallurgica et Materialia*, 43 (1995) 3873-3884.
- [194] R.Y. Yang, R.P. Zou, A.B. Yu, *Physical Review E*, 62 (2000) 3900-3908.
- [195] H.A. Makse, J. Kurchan, *Nature*, 415 (2002) 614-617.
- [196] L.E. Silbert, D. Ertas, G.S. Grest, T.C. Halsey, D. Levine, *Physical Review E*, 65 (2002) 031304.
- [197] R. Kikuuwe, N. Takesue, A. Sano, H. Mochiyama, H. Fujimoto, *Intelligent Robots and Systems, 2005. (IROS 2005). 2005 IEEE/RSJ International Conference on, 2005*, pp. 1009-1016.
- [198] Y. Jiao, F.H. Stillinger, S. Torquato, *Physical Review E*, 79 (2009) 041309.
- [199] Y. Jiao, F.H. Stillinger, S. Torquato, *Physical Review Letters*, 100 (2008) 245504.
- [200] D.D. Quinn, *ASME Conference Proceedings, 2002* (2002) 361-367.
- [201] Y.U. Wang, *Acta Materialia*, 54 (2006) 953-961.
- [202] Y.U. Wang, *Acta Materialia*, 55 (2007) 3835-3844.
- [203] L.E. Landau LD, *Fluid mechanics, 2nd ed.*, Butterworth-Heinemann, Oxford, 1997.

# Appendix A: Copyright Permission of Contents in Section 2.2.1 of Chapter 2

Section 2.2.1 of Chapter 2 in this dissertation was originally published in “Phase field modeling and simulation of particulate magnetoelectric composites: Effects of connectivity, conductivity, poling and bias field”, Acta Materialia, Elsevier, 2014, 70, page 45-55. Permission to reuse materials from the published work was obtained with kind permission from Elsevier. A copy of the granting permission for reproduction is shown as below.

This is a License Agreement between Fengde D Ma ("You") and Elsevier ("Elsevier"). The license consists of your order details, the terms and conditions provided by Elsevier, and the [payment terms and conditions](#).

License Number	3538850136186
License date	Dec 30, 2014
Order Content Publisher	Elsevier
Order Content Publication	Acta Materialia
Order Content Title	Phase field modeling and simulation of particulate magnetoelectric composites: Effects of connectivity, conductivity, poling and bias field
Order Content Author	None
Order Content Date	15 May 2014
Licensed content volume number	70
Licensed content issue number	n/a
Number of pages	11
Type of Use	reuse in a thesis/dissertation
Portion	full article
Format	both print and electronic

Are you the author of this Elsevier article?	Yes
Will you be translating?	No
Title of your thesis/dissertation	COMPUTATIONAL STUDY OF MICROSTRUCTURE-PROPERTY-MECHANISM RELATIONS IN FERROIC COMPOSITES
Expected completion date	Jan 2015
Estimated size (number of pages)	120
Elsevier VAT number	GB 494 6272 12
Price	0.00 USD
VAT/Local Sales Tax	0.00 USD / 0.00 GBP
Total	<b>0.00 USD</b>

# Appendix B: Copyright Permission of Contents in Chapter 3

Chapter 3 of this dissertation was originally published in “Phase field modeling and simulation of particulate magnetoelectric composites: Effects of connectivity, conductivity, poling and bias field”, Acta Materialia, Elsevier, 2014, 70, page 45-55. Permission to reuse materials from the published work was obtained with kind permission from Elsevier. A copy of the granting permission for reproduction is shown as below.

This is a License Agreement between Fengde D Ma ("You") and Elsevier ("Elsevier"). The license consists of your order details, the terms and conditions provided by Elsevier, and the [payment terms and conditions](#).

License Number	3538850136186
License date	Dec 30, 2014
Order Content Publisher	Elsevier
Order Content Publication	Acta Materialia
Order Content Title	Phase field modeling and simulation of particulate magnetoelectric composites: Effects of connectivity, conductivity, poling and bias field
Order Content Author	None
Order Content Date	15 May 2014
Licensed content volume number	70
Licensed content issue number	n/a
Number of pages	11
Type of Use	reuse in a thesis/dissertation
Portion	full article
Format	both print and electronic

Are you the author of this Elsevier article?	Yes
Will you be translating?	No
Title of your thesis/dissertation	COMPUTATIONAL STUDY OF MICROSTRUCTURE-PROPERTY-MECHANISM RELATIONS IN FERROIC COMPOSITES
Expected completion date	Jan 2015
Estimated size (number of pages)	120
Elsevier VAT number	GB 494 6272 12
Price	0.00 USD
VAT/Local Sales Tax	0.00 USD / 0.00 GBP
Total	<b>0.00 USD</b>

# Appendix C: Copyright Permission of Figures in Chapter 4

Chapter 4 of this dissertation was originally published in “Effect of magnetic domain structure on longitudinal and transverse magnetoelectric response of particulate magnetostrictive-piezoelectric composites”, Applied Physics Letters, AIP Publishing LLC, 2014, 104, page 112903. Permission to reuse the figures from the published work was obtained with kind permission from AIP Publishing LLC. A copy of the granting permissions for reproduction are shown as below.

License Number	3538860255493
Order Date	Dec 30, 2014
Order Content Publisher	AIP Publishing LLC
Order Content Publication	Applied Physics Letters
Article Title	Effect of magnetic domain structure on longitudinal and transverse magnetoelectric response of particulate magnetostrictive-piezoelectric composites
Author	Fengde D. Ma, Yongmei M. Jin, Yu U. Wang, et al.
Online Publication Date	Mar 19, 2014
Volume number	104
Issue number	11
Type of Use	Thesis/Dissertation
Requestor type	Author (original article)
Format	Print and electronic
Portion	Figure/Table
Number of figures/tables	5
Title of your thesis / dissertation	COMPUTATIONAL STUDY OF MICROSTRUCTURE-PROPERTY-MECHANISM RELATIONS IN FERROIC COMPOSITES



Expected completion date	Jan 2015
Estimated size (number of pages)	120
<b>Total</b>	<b>0.00 USD</b>

# Appendix D: Copyright Permission of Texts in Chapter 4

Chapter 4 of this dissertation was originally published in “Effect of magnetic domain structure on longitudinal and transverse magnetoelectric response of particulate magnetostrictive-piezoelectric composites”, Applied Physics Letters, AIP Publishing LLC, 2014, 104, page 112903. Permission to reuse the texts from the published work was obtained with kind permission from AIP Publishing LLC. A copy of the granting permissions for reproduction are shown as below.

License Number	3538851419340
Order Date	Dec 30, 2014
Order Content	AIP Publishing LLC
Publisher	
Order Content	Applied Physics Letters
Publication	
Article Title	Effect of magnetic domain structure on longitudinal and transverse magnetoelectric response of particulate magnetostrictive-piezoelectric composites
Author	Fengde D. Ma, Yongmei M. Jin, Yu U. Wang, et al.
Online Publication Date	Mar 19, 2014
Volume number	104
Issue number	11
Type of Use	Thesis/Dissertation
Requestor type	Author (original article)
Format	Print and electronic
Portion	Excerpt (> 800 words)
Will you be translating?	No

Title of your thesis / dissertation	COMPUTATIONAL STUDY OF MICROSTRUCTURE- PROPERTY-MECHANISM RELATIONS IN FERROIC COMPOSITES
Expected completion date	Jan 2015
Estimated size (number of pages)	120
<b>Total</b>	<b>0.00 USD</b>